

# UC San Diego

## UC San Diego Electronic Theses and Dissertations

### Title

The Development and Application of Nanoparticles for Cell Tracking and Multimodal Imaging

### Permalink

<https://escholarship.org/uc/item/4tp8r86q>

### Author

Lemaster, Jeanne Elizabeth

### Publication Date

2019

Peer reviewed|Thesis/dissertation

UNIVERSITY OF CALIFORNIA SAN DIEGO

The Development and Application of Nanoparticles for Cell Tracking and Multimodal Imaging

A dissertation submitted in partial satisfaction of the  
requirements for the degree Doctor of Philosophy

in

NanoEngineering

by

Jeanne E. Lemaster

Committee in charge:

Professor Jesse Jokerst, Chair  
Professor Yi Chen  
Professor Vicky Grassian  
Professor David Hall  
Professor Darren Lipomi

2019

Copyright

Jeanne E. Lemaster, 2019

All rights reserved.

The Dissertation of Jeanne E. Lemaster is approved, and it is acceptable in quality and form for publication on microfilm and electronically:

---

---

---

---

---

Chair

University of California San Diego

2019

## DEDICATION

This dissertation is dedicated to my friends, labmates, mentors, and family, especially my late father who wasn't here to see the completion of my degree but supported me throughout my life pursuits. I am grateful for the patience, knowledge, encouragement, and advice which lit the road of my PhD journey – and that has made all the difference.

## EPIGRAPH

*"Education never ends, Watson. It is a series of lessons, with the greatest for the last."*

*Sir Arthur Conan Doyle, His Last Bow*

*"There is a way out of every box, a solution to every puzzle; it's just a matter of finding it."*

*Captain Jean-Luc Picard*

*"Higher, further, faster, baby."*

*Carol Danvers*

## TABLE OF CONTENTS

SIGNATURE PAGE .....	iii
DEDICATION .....	iv
EPIGRAPH .....	v
TABLE OF CONTENTS .....	vi
LIST OF TABLES .....	ix
LIST OF FIGURES .....	x
LIST OF SCHEMES .....	xiii
ACKNOWLEDGEMENTS .....	xiv
VITA .....	xvi
ABSTRACT OF THE DISSERTATION .....	xvii
CHAPTER 1: INTRODUCTION AND HISTORY .....	1
1.1 Introduction .....	1
1.2 Molecular Imaging .....	1
1.3 Photoacoustic Imaging .....	2
1.4 Contrast Agents in Photoacoustic Imaging .....	3
1.5 Inorganic Nanoparticles .....	4
1.6 Organic Nanoparticles .....	7
1.7 Multimodal Imaging with Photoacoustics .....	9
1.8 Nanoparticle Coatings .....	10
1.9 Conclusion .....	11
1.10 Acknowledgments .....	11
CHAPTER 2: GADOLINIUM DOPING ENHANCES THE PHOTOACOUSTIC SIGNAL OF SYNTHETIC MELANIN NANOPARTICLES: A DUAL MODALITY CONTRAST AGENT FOR STEM CELL IMAGING .....	12
2.1 Introduction .....	12
2.2. Methods .....	13
2.3. Results and Discussion .....	17
2.3.1 Synthesis and Characterization .....	17
2.3.2 Photoacoustic and MRI Performance .....	19
2.3.3 Cellular Imaging .....	24

2.4. Conclusion.....	26
2.5 Author Contributions.....	27
2.6 Acknowledgements .....	27
2.7 Appendix .....	28
<b>CHAPTER 3: SYNTHESIS OF ULTRASMALL SYNTHETIC MELANIN NANOPARTICLES BY UV IRRADIATION IN ACIDIC AND NEUTRAL CONDITIONS .....</b>	<b>39</b>
3.1 Introduction .....	39
3.2. Methods.....	41
3.3. Results and Discussion.....	43
3.3.1 Size control. ....	45
3.3.4 Wavelength Effects.....	48
3.3.4 FTIR Characterization .....	48
3.3.4 NMR Characterization.....	49
3.3.5 Mechanism.....	50
3.4. Conclusion.....	52
3.5 Author Contributions.....	52
3.6 Acknowledgements .....	53
3.7 Appendix .....	54
<b>CHAPTER 4: THE DEVELOPMENT OF A TRIMODAL CONTRAST AGENT FOR ACOUSTIC AND MAGNETIC PARTICLE IMAGING OF STEM CELLS .....</b>	<b>59</b>
4.1 Introduction .....	59
4.2 Materials and Methods .....	62
4.3 Results and Discussion.....	66
4.3.1 Synthesis and Physical Characterization .....	66
4.3.2 Optimization, Viability, and Cellular Uptake.....	67
4.3.3 Concentration Dependence and Cell Labeling Optimization .....	71
4.4 Conclusion.....	81
4.5 Acknowledgements .....	81
4.6 Appendix .....	82
<b>CHAPTER 5: PHOTOACOUSTIC IMAGING QUANTIFIES DRUG RELEASE FROM NANOCARRIERS VIA REDOX CHEMISTRY OF DYE-LABELED CARGO.....</b>	<b>91</b>
5.1 Introduction .....	91
5.2 Materials and Methods .....	92



Reagents.....	92
Instruments. ....	92
Synthesis of precursors.....	93
5.3 Results and Discussion.....	96
5.3.1 Synthesis of PTX-MB .....	97
5.3.2 Optical and acoustic characterization of PTX-MB.....	99
5.3.3 Nanoparticle Synthesis and Characterization .....	100
5.3.4 <i>In vitro</i> drug release and anticancer inhibitory activity .....	102
5.3.5 <i>In vivo</i> drug release and anticancer activity.....	104
5.4 Conclusion.....	106
5.5 Acknowledgements .....	108
5.6 Appendix .....	108
CHAPTER 6: CONCLUSION AND FUTURE DIRECTION.....	122
6.1 Translation of Nanoparticle-based Contrast Agents to Clinical Settings.....	122
6.2 Hardware Advancements .....	122
6.3 Future Direction in Nanoparticle Contrast Agent Development.....	123
REFERENCES .....	125

## LIST OF TABLES

Table 2.1. ICP-OES measurements of metal-doped SMNP.....	19
--	----

## LIST OF FIGURES

Figure 1.1. Basics of Photoacoustics. ....	3
Figure 1.2 Biodegradable gold nanoparticles. ....	6
Figure 1.3 Imaging Reactive Oxygen Species with Acoustic Data and Semiconducting Nanoparticles. ....	8
Figure 1.4 <i>In vivo</i> imaging of uranyl cation.....	8
Figure 2.1 Synthesis and characterization of synthetic melanin nanoparticles (SMNP).....	18
Figure 2.2 Photoacoustic (PA) imaging and intensity data of SMNP and metal-doped SMNP....	21
Figure 2.3 Photoacoustic (PA) intensity of Gd(III)-doped SMNP particles is dependent on the concentration of SMNP and Gd(III). ....	22
Figure 2.4 Optimization of hMSC Labeling Parameters. ....	23
Figure 2.5. Photoacoustic and MR imaging of Gd(III)-SMNP implanted into mouse hearts. ....	26
Figure 3.1 Synthesis and characterization of ultrasmall synthetic melanin nanoparticles. ....	44
Figure 3.2. TEM and absorption spectrum of SMNP and UMNP at initial concentration of 1 mg/mL dopamine.....	45
Figure 3.3. Characterization of SMNP and UMNP formed in water with UV irradiation at varying concentrations.....	47
Figure 3.4 NMR spectroscopy shows loss of aliphatic side chains in UMNP indicating that polymerization has occurred.....	50
Figure 3.5 Mechanism of UV-initiated polymerization.....	52
Figure 4.1. Nanobubble Schematic and Synthesis.....	67
Figure 4.2. Optimization of synthesis parameters and cell number detection.....	70
Figure 4.3. Signal intensity of the multimodal contrast agent and effect of incubation time on labeled cells.....	73
Figure 4.4 Effect of concentration on US, PA, and MPI signal in labeled cells.....	74
Figure 4.5. The differentiation ability of hMSCs is unaffected by the nanobubble labeling.....	78

Figure 4.6. <i>In vivo</i> imaging .....	80
Figure 5.1. Structural, spectral and photoacoustic characterization of PTX-MB .....	98
Figure 5.2 Preparation and characterization of PLGA nanoparticles encapsulating PTX-LMB. ....	101
Figure 5.3. <i>In vitro</i> drug release and cancer inhibitory activity of PTX-MB and PTX-MB @ PLGA NPs.....	102
Figure 5.4. Photoacoustic <i>in vivo</i> drug release monitoring in mice.....	104
Figure 5.5. <i>In vivo</i> efficacy of PTX-MB @ PLGA NPs. ....	106

## LIST OF SCHEMES

Scheme 5.1. Design and synthesis of paclitaxel-methylene blue conjugate (PTX-MB).....97

## ACKNOWLEDGEMENTS

I would like to acknowledge Professor Jesse Jokerst, Co-Advisor Professor David Hall, and committee members: Professor Chen, Professor Grassian, and Professor Lipomi for their support and guidance on my committee and through my research efforts.

Additionally, I am grateful for the assistance and constant backing from Professor Andrew Kummel, Professor Jan Talbot, Professor Benjamin Russ, Professor Sourena Fakhimi, Professor Nathan Gianneschi, Professor Saber Hussain, Dana Jimenez, Christopher Barback, collaborators Dr. Zhao Wang and Dr. Ananth Jeevarathinam, Chava Angell, Mark Stambaugh, and all of the former and current members of the Jokerst, Chen, and Zhang labs.

I would like to thank all my family and friends for their patience, love, editing, music suggestions, surf sessions, workouts, and happy hours which helped me through this process. I would especially like to thank Calvin (and his feline friend Hobbes) for his first kicks, first smiles, and first love.

Chapter 1, in part, is a reprint of the material as it appears in Wiley Interdisciplinary Reviews: Nanomedicine and Nanobiotechnology 2017. Lemaster, Jeanne, Jokerst, Jesse V. The dissertation author was the primary author of this chapter.

Chapter 2, in full, is reprinted and reformatted material as it appears in Chemistry of Materials, 2018, Lemaster, Jeanne E., Zhao Wang, Ali Hariri, Fang Chen, Ziyang Hu, Yuran Huang, Christopher V. Barback, Richard Cochran, Nathan C. Gianneschi, and Jesse V. Jokerst. The dissertation author was the co-first author of this paper.

Chapter 3, in full, is reprinted and reformatted material as it appears in ACS Applied Bio Materials, 2019, Lemaster, Jeanne E., AnanthaKrishnan Soundaram Jeevarathinam, Ajay Kumar,

Bhargavi Chandrasekar, Fang Chen, and Jesse V. Jokerst. The dissertation author was the primary investigator and author of this paper.

Chapter 4, in full, is reprinted and reformatted material as it appears in ACS Applied Nano Materials, Lemaster, Jeanne E., Fang Chen, Taeho Kim, Ali Hariri, and Jesse V. Jokerst, 2018. The dissertation author was the primary investigator and author of this paper.

Chapter 5, in full, is currently being prepared for submission for publication of the material, AnanthaKrishnan Soundaram Jeevarathinam, Lemaster, Jeanne E., Fang Chen, Eric Zhao, and Jesse V. Jokerst. The dissertation author was the co-first author of this paper.

Chapter 6, in part, is a reprint of the material as it appears in Wiley Interdisciplinary Reviews: Nanomedicine and Nanobiotechnology 2017. Lemaster, Jeanne, Jokerst, Jesse V. The dissertation author was the primary author of this chapter.

## VITA

- 2008 Bachelor of Science, Chemical Engineering, The Ohio State University
- 2016 Master of Science, NanoEngineering, University of California San Diego
- 2016-2017 Teaching Assistant, University of California San Diego
- 2015-2019 Research Assistant, University of California San Diego
- 2019 Doctor of Philosophy, NanoEngineering, University of California San Diego

## PUBLICATIONS

**Lemaster, Jeanne E.**, et al. "Gadolinium doping enhances the photoacoustic signal of synthetic melanin nanoparticles: a dual modality contrast agent for stem cell imaging." *Chemistry of Materials* 31.1 (2018): 251-259.

**Lemaster, Jeanne E.**, et al. "Development of a trimodal contrast agent for acoustic and magnetic particle imaging of stem cells." *ACS Applied Nano Materials* 1.3 (2018): 1321-1331.

**Lemaster, Jeanne E.**, et al. "Synthesis of Ultrasmall Synthetic Melanin Nanoparticles by UV Irradiation in Acidic and Neutral Conditions", *ACS Applied Bio Materials* (2019): 4667-4674.

**Lemaster, Jeanne**, Jeevarathinam, Ananthakrishnan, Chen, Fang; Zhao, Eric; Jokerst, Jesse, Photoacoustic Imaging Quantifies Drug Release from Nanocarriers via Redox Chemistry of Dye-Labeled Cargo, submitted for publication.

Hariri, Ali, Eric Zhao, Ananthakrishna Soundaram Jeevarathinam, **Jeanne Lemaster**, Jianjian Zhang, and Jesse V. Jokerst. "Molecular imaging of oxidative stress using an LED-based photoacoustic imaging system." *Scientific reports* 9, no. 1 (2019): 1-10.

Chen, F., Zhao, E.R., Hableel, G., Hu, T., Kim, T., Li, J., Gonzalez-Pech, N.I., Cheng, D.J., **Lemaster, J.E.**, Xie, Y. and Grassian, V.H., 2019. Increasing the Efficacy of Stem Cell Therapy via Triple-Function Inorganic Nanoparticles. *ACS nano*.

Chen, Fang, Gongyi Li, Eric Ruike Zhao, Jingting Li, Ghanim Hableel, **Jeanne Lemaster**, Yuting Bai, George L. Sen, and Jesse V. Jokerst. "Cellular toxicity of silicon carbide nanomaterials as a function of morphology." *Biomaterials* 179 (2018): 60-70.



Wang, Junxin, Ananthkrishnan Soundaram Jeevarathinam, Anamik Jhunjhunwala, Haowen Ren, **Jeanne Lemaster**, Yanqi Luo, David P. Fenning, Eric E. Fullerton, and Jesse V. Jokerst. "A Wearable Colorimetric Dosimeter to Monitor Sunlight Exposure." *Advanced Materials Technologies* 3, no. 6 (2018): 1800037.

Kim, Taeho, **Jeanne Lemaster**, Fang Chen, Jin Li, and Jesse V. Jokerst. "Photoacoustic Imaging of Human Mesenchymal Stem Cells Labeled with Prussian Blue–Poly (l-lysine) Nanocomplexes." *ACS nano* 11, no. 9 (2017): 9022-9032.

Hariri, Ali, **Jeanne Lemaster**, Junxin Wang, AnanthaKrishnan S. Jeevarathinam, Daniel L. Chao, and Jesse V. Jokerst. "The characterization of an economic and portable LED-based photoacoustic imaging system to facilitate molecular imaging." *Photoacoustics* 9 (2018): 10-20.

**Lemaster, Jeanne**, and Jesse V. Jokerst. "What is new in nanoparticle-based photoacoustic imaging?." *Wiley Interdisciplinary Reviews: Nanomedicine and Nanobiotechnology* 9.1 (2017).

Arconada-Alvarez, Santiago J., **Lemaster, Jeanne**, et al "The development and characterization of a novel yet simple 3D printed tool to facilitate phantom imaging of photoacoustic contrast agents." *Photoacoustics* 5 (2017): 17-24.

**Skebo, Jeanne**, et al. "Assessment of metal nanoparticle agglomeration, uptake, and interaction using high-illuminating system." *International Journal of Toxicology* 26.2 (2007): 135-141.

## **FIELDS OF STUDY**

Major Field: NanoEngineering

Professor Jesse Jokerst, PhD

## ABSTRACT OF THE DISSERTATION

The Development and Application of Nanoparticles for Cell Tracking and Multimodal Imaging

by

Jeanne Lemaster

Doctor of Philosophy in NanoEngineering

University of California San Diego, 2019

Professor Jesse Jokerst, Chair

Stem cell therapy is an emerging tool to treat a variety of conditions from cancer to musculoskeletal disorders to cardiac disease. Current FDA-approved stem cell therapies utilize cells from peripheral blood or bone marrow to treat patients who have disorders of the hematopoietic system; however clinical trials for utilizing stem cells to treat muscular skeletal disorders and cardiac disease are underway. Because stem cells self-renew and differentiate in multiple lineage pathways, the general theory behind stem cell therapy is that damaged tissue can be repaired or regenerated and that trophic activity of stem cells can modulate other immune cells.

While stem cell therapy has the potential to treat a variety of conditions due to its regenerative and proliferative activity, more study is needed to address ideal injection time, method of injection, distribution, and retention concerns. Imaging stem cells addresses these concerns and can provide more information overall about the fate of stem cells. Contrast agents are needed to increase the contrast and specificity of imaging stem cells. Nanoparticle-based contrast agents are important tools for imaging because they offer high contrast and stable signal. Chapter 1 of this

thesis provides a background on cell therapy and various imaging modalities. Chapter 2 details the design and synthesis of gadolinium-doped synthetic melanin nanoparticles which were used to label stem cells for photoacoustics and magnetic resonance imaging (MRI). Chapter 3 explores the mechanism of ultraviolet (UV)-induced synthetic melanin nanoparticle generation. Chapter 4 describes the design, synthesis, and application of an iron oxide PLGA-based nanoparticle used for ultrasound, photoacoustics, and magnetic particle imaging (MPI). Finally, Chapter 5 describes the synthesis and application of a nanoparticle for cancer treatment that shows an increase in photoacoustic intensity as drug is released. This nanoparticle was then used to treat tumors in mice and luminescence was used to monitor treatment response. Chapter 6 concludes with a perspective on the future of imaging cell therapy with possible directions.

## CHAPTER 1: INTRODUCTION AND HISTORY

### 1.1 Introduction

Cell-based therapies are expanding the field of regenerative medicine and have been used to treat a variety of conditions including cancer<sup>1</sup>, osteoarthritis<sup>2</sup>, neurodegenerative conditions<sup>3</sup>, and myocardial repair<sup>4</sup>. Current FDA-approved stem cell therapies utilize cells from peripheral blood or bone marrow to treat patients who have disorders of the hematopoietic system. Additionally, clinical trials utilizing stem cells to treat muscular skeletal disorders and cardiac disease are underway<sup>5</sup>. Because stem cells have the ability to self-renew and differentiate in multiple lineage pathways, the general theory behind stem cell therapy is that damaged tissue can be repaired or regenerated and that trophic activity of stem cells can modulate other immune cells.

Although stem cell therapy has the potential to treat a variety of conditions due to its regenerative and proliferative activity, more study is needed to address improve therapeutic outcomes<sup>6</sup>. Questions such as engraftment, migration, and retention can be answered using *in vivo* molecular imaging<sup>7</sup>. Additionally, recent advances in molecular imaging provide a more in-depth understanding of the *in vivo* behavior of stem cells and is important in preclinical and clinical studies.

### 1.2 Molecular Imaging

*In vivo* molecular imaging is a powerful tool to study biology and practice medicine.<sup>8-9</sup> Ultrasound imaging is particularly useful because of its low cost, good depth of penetration, and high temporal and spatial resolution. One recent development in ultrasound is photoacoustic imaging, which uses the absorption of optical energy to generate acoustic waves. Photoacoustic imaging offers high contrast and good signal-to-noise ratios in large volumes of biological tissues

without ionizing radiation or tissue damage. It combines the high temporal and spatial resolution of ultrasound with the good contrast and multiplexing capabilities of optical imaging. Different designs offer resolution from whole organs to organelles.<sup>10</sup>

Imaging can help address these concerns by providing information during injection, immediately after injection, and even the long term fate of these cells. Multimodal imaging for visualizing stem cells combines the strengths of each modality. The gold standard of imaging stem cells uses FDA-approved iron oxide-based nanoparticles to label stem cells and magnetic resonance imaging (MRI)<sup>11</sup>. This method is limited by poor temporal resolution, high background signal, and high cost. Magnetic particle imaging is a related modality which utilizes iron oxide nanoparticles to image cells with no background, but also lacks temporal resolution and is not yet clinically available. Clinically, ultrasound is one of the most common imaging techniques but it is limited by high background and low contrast. Photoacoustics is an emerging technique which utilizes the high spatial and temporal resolution of ultrasound but offers the contrast and spectral tunability of optical imaging.

### **1.3 Photoacoustic Imaging**

Photoacoustic imaging is a “light in-sound out” effect versus the “sound in-sound out” in traditional ultrasound (**Fig. 1.1A**). The mechanism of contrast is absorption of photons and subsequent thermal expansion. First, a nanosecond-pulse laser beam irradiates the sample and is absorbed to raise the temperature ( $\Delta T$ ) and cause a pressure rise,  $p_0$ , due to thermal expansion via  $p_0 = \beta \cdot \Delta T / \kappa$ . Here,  $\beta$  is the thermal expansion coefficient, and  $\kappa$  is the isothermal compressibility.<sup>10</sup> Most excitation sources used in photoacoustic imaging are between ~680 and ~1100 nm<sup>12</sup>. This is because near infrared (NIR) light has higher penetration depth than optical light due to lower

hemoglobin absorption and tissue scattering.<sup>13-14</sup> A transducer then detects the pressure wave and software forms an image from the acoustic data.

Current challenges in photoacoustic imaging include light scatter and absorption, frequency/signal changes because of volume modifications, reconstruction inaccuracies, tissue background noise, attenuation of the excitation source, and poor penetration depth.<sup>15</sup> Therefore, developing effective contrast agents to specifically increase signal at the site of interest is important in improving photoacoustic imaging for use in humans.

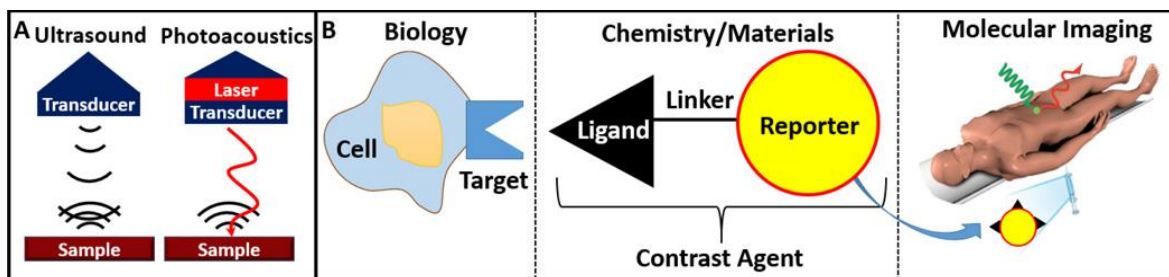


**Figure 1.1. Basics of Photoacoustics.** **A)** Ultrasound and photoacoustic imaging both use acoustic data (curved black lines) to create an image. In ultrasound, impedance mismatch creates contrast. In photoacoustics, incident light (red arrow) causes thermal expansion and hence a pressure difference (black lines). **B)** Contrast agents link biology and medicine via an imaging signal. Nanoparticles make excellent reporters because they have high signal intensity and stability.

#### 1.4 Contrast Agents in Photoacoustic Imaging

Imaging agents (or contrast agents) increase the specific contrast of a target organ or disease process such as cancer (**Fig. 1.1B**). Photoacoustic contrast agents should be effective at low doses, biocompatible, biodegradable, non-toxic, and complement the intrinsic ultrasound data.<sup>16, 17</sup> There are both endogenous and exogenous photoacoustic contrast agents. Endogenous agents include hemoglobin and melanin—these naturally absorb in the infrared region.<sup>18</sup> However, endogenous agents often have less contrast than exogenous agents such as nanoparticles or dyes because hemoglobin/melanin is also present in normal adjacent tissue.<sup>19</sup> While this can be

improved by using a reporter gene to specifically express a protein, e.g. tyrosinase,<sup>20</sup> at the site of interest, the use of reporter genes in humans is limited.

Small molecule dyes are a second class of photoacoustic contrast agents—many of these are already clinically approved. They also have good tissue penetration after intravenous injection and defined pharmacokinetics and pharmacodynamics. Examples include methylene blue, indocyanine green, and Prussian blue.<sup>21</sup> The disadvantages of small molecules include low photoacoustic signal, poor photostability, fast clearance, and small optical absorption cross sections.<sup>22</sup>

Nanoparticles are a third class of contrast agents. Nanoparticles are useful in photoacoustic imaging because they have high signal and stable signal. They can also be functionalized with many copies of targeting ligands to home the material to the site of interest. Nanoparticles can be made from a variety of responsive materials that produce signal only under the influence of a chemical cue. The rest of this manuscript describes some of the most interesting and recent advances in nanoparticles for photoacoustic imaging including inorganic nanoparticles, organic/polymeric nanoparticles, nanoparticle coatings, multimodality imaging, as well as emerging topics.

### **1.5 Inorganic Nanoparticles**

Metal nanoparticles were among the first materials to be used as photoacoustic contrast agents because of their high absorption cross section (intense photoacoustic signal) as well as established biocompatibility.<sup>23-24</sup> Gold nanoparticles are particularly popular because they have size- and shape-tunable absorption peaks and thus can facilitate multiplexing in photoacoustic imaging (multiplexing is the measurement of multiple different signal types at the same time).<sup>25</sup> Several configurations of gold nanoparticles have been studied including spheres, rods, shells, and

liposomal formulations.<sup>26</sup> While metal nanoparticles do not experience photobleaching, their morphology can change under irradiation to decrease signal.<sup>27</sup> Most nanoparticles used in imaging are 20-150 nm. Particles that are smaller than ~10 nm are easily cleared from circulation via the kidneys and thus do not have adequate residence time to accumulate in target tissue. The signal strength of these smaller particles is usually low as well.

Recent advances in gold nanoparticles for photoacoustics have increased signal. For example, Emelianov and coworkers have improved contrast by using nonlinear photoacoustic effects. This was reported when plasmonic nanoparticles undergo aggregation and cellular endocytosis. This causes thermal coupling, localized temperature increases, and nonlinear effects for improved signal.<sup>28</sup> In another example, Zharov created clusters of gold nanoparticles linked via photoswitchable proteins.<sup>29</sup> The distance between the nanoparticles changed upon activation of the protein, which in turn changed the photoacoustic signal.

Another challenge is poor biodegradation of gold nanoparticles. These materials accumulate in the liver and spleen with very long clearance times. More recently, < 5-nm gold particles were bound together into clusters with a biodegradable binder (**Fig. 1.2**).<sup>30</sup> These larger particles have robust photoacoustic signal, and the cluster was sensitive to pH and acidic endosomes that could result in biodegradation and clearance of the smaller gold particles via the kidney.<sup>31</sup> Similarly, 2-4 nm gold nanobeacons (GNBs) were placed inside phospholipid nanoparticle, and this contrast agent produced a photoacoustic signal nearly 10 times greater than blood.<sup>32</sup>



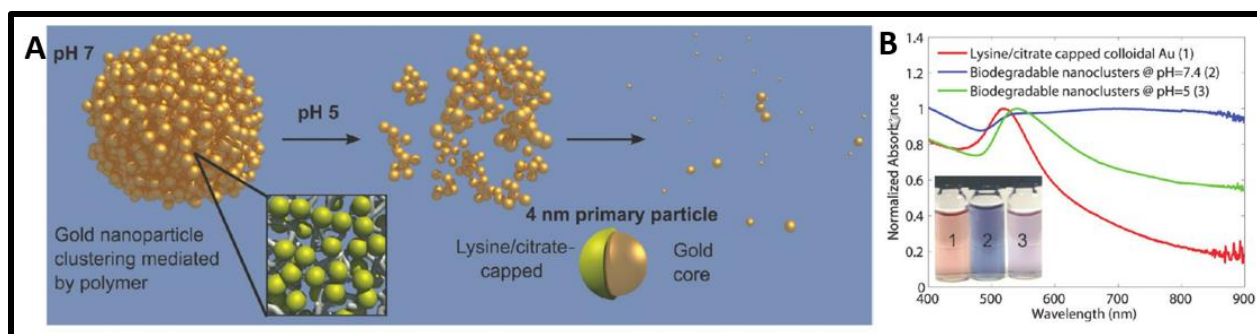


**Figure 1.2 Biodegradable gold nanoparticles.** A) Small gold spheres are bound together with a pH sensitive polymer. At endosomal pH values (~5), this polymer releases the small gold spheres. This causes a change in the absorbance spectrum (B). This is important because the larger gold cluster can be used for imaging, and the smaller spheres can then clear from the body via the kidney. Reproduced courtesy of American Chemical Society.<sup>30</sup>

Beyond gold, upconverting nanoparticles (UCNPs) have recently been shown to offer narrow excitation/emission profiles for photoacoustic imaging. These materials are based on phosphors like NaYF<sub>4</sub> doped with ytterbium (Yb<sup>3+</sup>), erbium (Er<sup>3+</sup>), and terbium (Tb<sup>3+</sup>). UCNPs convert NIR to visible light via donor (Yb)/acceptor (Er) relationships.<sup>33</sup> The heating capacity of NaYF<sub>4</sub>:Yb<sup>3+</sup>, Er<sup>3+</sup> UCNPs and luminescence quenching offers robust photoacoustic signal for small animal imaging at 980 nm.<sup>33</sup> These materials might be challenged by toxicity concerns related to injection of these exotic elements.

Copper and copper sulfide are also emerging materials. In one example, copper was encapsulated in a 80-90 nm phospholipid-entrapped nanoparticle (NanoCuN); it showed a 6-fold higher signal sensitivity than blood when used in a rodent model.<sup>34</sup> Copper sulfide (CuS) is also useful because it has a very tunable absorption peak.<sup>35</sup> In one example, CuS nanoparticles were used with a 1064 nm Nd:YAG laser to image human breast tissue up to 40 mm deep.<sup>36</sup> CuS nanoparticles were also used in a mouse model to visualize neural structures with clearance from the brain after 7 days.<sup>36</sup>

## 1.6 Organic Nanoparticles

Organic polymeric nanoparticles offer good clearance and biodegradation. They often use materials with existing FDA approval.<sup>37</sup> Porphysomes were among the earliest organic agents used for photoacoustic imaging and photodynamic therapy.<sup>38</sup> A new approach to manufacturing of nanoparticles has been a “green” synthesis of nanoparticles using naturally occurring materials as the source of contrast. In one example, nanoparticles were derived from honey via a solvent-free rapid surface passivation of carbon nanoparticles with organic macromolecules.<sup>39</sup> In another example, nanoparticles were made from the thermal and acidic degradation of cotton cellulose linters and later applied to ovarian cancer imaging. These cellulose nanoparticles were then shown to biodegrade into glucose in the presence of cellulase.<sup>40</sup> Another example harvested melanin from melanocytes and created nanoparticles from this natural pigment for photoacoustic imaging.<sup>41</sup> We suspect that this trend will continue and might help in the clinical translation of these materials.

Researchers are taking inspiration from materials used for light harvesting such as in photovoltaics, light emitting diodes, and energy transfer cascades. In one example, semiconducting polymer nanoparticles sensitive to reactive oxygen species were created via a benzothiadiazole scaffold. (**Fig. 1.3**).<sup>42</sup> These nanoparticles also have good structural flexibility, resistance to photodegradation, narrow photoacoustic spectral profile, and more photostability than gold nanorods.<sup>42</sup> In another example, light-harvesting porphyrins were used to synthesize a stimuli-responsive nanoswitch.<sup>43</sup> Organic nanoformulated naphthalocyanines were used in multispectral photoacoustic imaging to construct detailed maps of lymphatic drainage systems.<sup>44</sup> In another example, nanoparticles were made from perylene-diimide molecules. These materials had sufficient signal to image through intact skull and identify glioblastoma.<sup>45</sup> Additional work has described pyrrole-based nanoparticles<sup>22</sup> and porphyrinoids.<sup>46-47</sup> In one example, porphyrinoid-

based nanoparticle were sensitive to the presence of uranium and offered parts-per-billion detection limits *in vivo* (Fig. 1.4).<sup>46</sup>

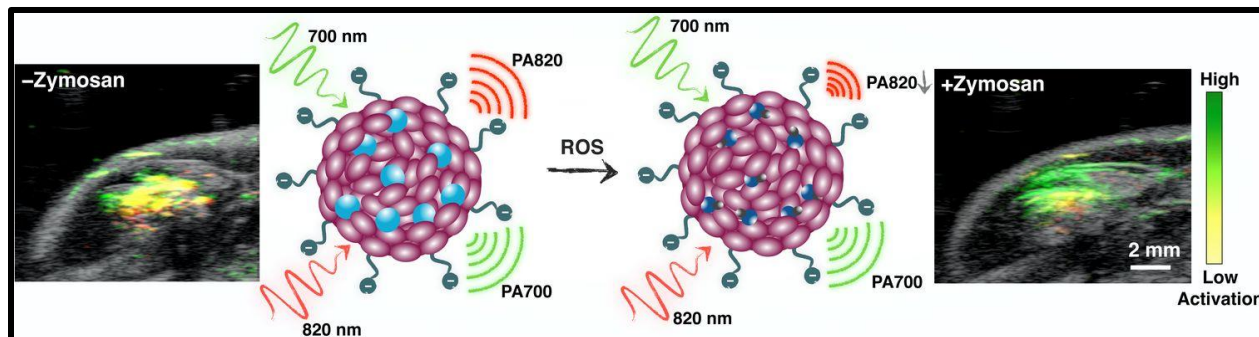


**Figure 1.3 Imaging Reactive Oxygen Species with Acoustic Data and Semiconducting Nanoparticles.** Nanoparticles based on benzothiadiazole groups are responsive to reactive oxygen species and produce more blue-shifted acoustic emission in the presence of reactive oxygen species (+Zymosan; right) than control animals (-Zymosan; left). Ratiometric photoacoustic imaging (700 nm/820 nm) can then be used to monitor expression of these molecules. (Zymosan is a glucan that induces experimental sterile inflammation.) Reproduced courtesy of Nature Publishing Group.<sup>48</sup>

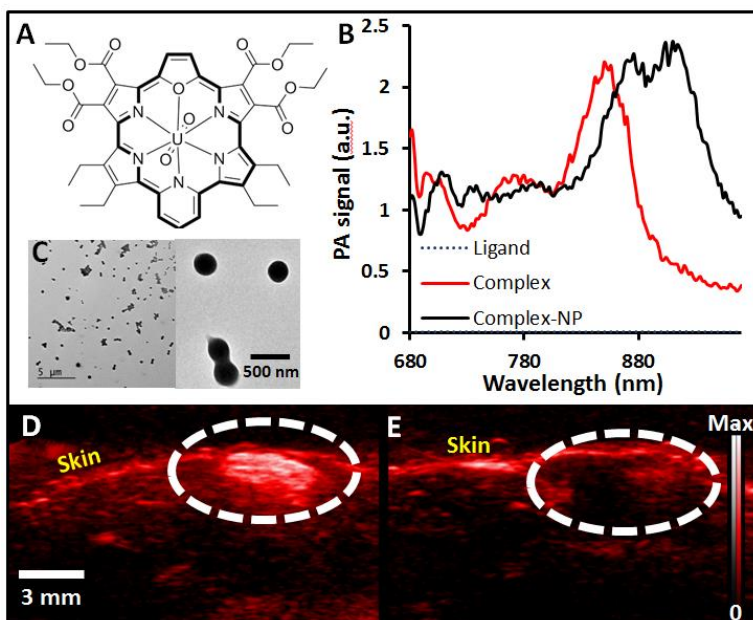


**Figure 1.4 In vivo imaging of uranyl cation.** A) A porphyrinoid macrocycle produces photoacoustic signal when the uranyl cation is chelated because of increased aromaticity (heavy black line). B) Photoacoustic spectrum for free macrocycle (ligand), uranium-complexed porphyrin (complex), and the complex solubilized in PLGA nanoparticles (Complex-NP). C) TEM of nanoparticles at two different magnifications. The *in vivo* imaging of 100  $\mu$ L of 0.38 nM NPs with the uranium complex (D) or empty macrocycle (E) highlights the signal difference. Note the scale and intensity bar in D and E apply to both panels. White dashed circle indicates the injection site. Reproduced with permission from The Royal Society of Chemistry.<sup>46</sup>

## 1.7 Multimodal Imaging with Photoacoustics

Combining photoacoustic imaging with other modalities can utilize the advantages of both methods and recent advancements in image acquisition and reconstruction have allowed multimodal imaging to expand.<sup>49</sup> Tantalum oxide-based polypyrrole (PPy) NPs were used for bimodal imaging to enhance X-ray CT and photoacoustic (PA) imaging.<sup>50</sup> MRI has excellent depth of penetration, but slower temporal resolution while photoacoustics has good temporal resolution and limited depth. In one example, a triple-modality nanoparticle combining magnetic resonance, photoacoustic, and Raman imaging (MPR) was used to resect glioma. Here, MRI signal is due to chelated gadolinium. The same probe can be used before (MRI) and during (photoacoustic) surgery for more accurate tumor resection.<sup>51</sup> Another alternative approach to MRI signal was shown via the copper component of copper sulfide nanoparticles.<sup>52</sup>

A similar approach was used with an ovarian cancer model, but the photoacoustic data was combined with Raman spectroscopy. Photoacoustics discriminated between tumor and normal tissue, and Raman offered guidance during surgical resection. Nanorods offered a 10-fold improvement in SERS signal versus gold spheres, but with only 1% of the volume.<sup>53</sup>

Other approaches have been inspired by traditional ultrasound. Microbubbles are used in diagnostic ultrasound because they have highly scattering acoustic properties and interact nonlinearly with incident ultrasound. However, they are generally used to image vascular targets because of their size ( $>1 \mu\text{m}$ ). One novel approach uses perfluorocarbon nanodroplets, which offer both ultrasound and photoacoustic contrast.<sup>54</sup> These materials are constructed from bovine serum albumin-coated liquid dodecafluoropentane and gold nanoparticles. The gold nanoparticle acts as a fuse to vaporize the dodecafluoropentane and produce acoustic impedance and photoacoustic signal. Another approach utilized the conversion of microbubbles to nanostructures using an

ultrasonic pulse. In this case, a bacteriochlorophyll–lipid shell was formed around a perfluoropropane gas and these microbubbles burst to form nanoparticles with unique optical properties.<sup>55</sup>

## **1.8 Nanoparticle Coatings**

The nanoparticle surface is where it interacts with the body. Thus, this layer has to be meticulously engineered to maintain low toxicity, high signal, and good targeting. While polyethylene glycol is often used as a coating agent on nanoparticles, silica also offers important advantages. First, it can increase the signal stability and prevent optically induced nanoparticle deformation—especially with gold nanoparticles.<sup>56</sup> Second, the overall magnitude of signal is 3- to 4-fold higher with the silica coating.<sup>57</sup> Third, silica can increase cellular uptake of gold into cells, which is useful for photoacoustic imaging of stem cell therapy.<sup>58</sup>

Other recent alternatives include non-cytotoxic PNIPAAmMA. This allows covalent attachment of targeting molecules like antibodies or magnetic nanoparticles and may also be used to improve target and anticancer therapies.<sup>59</sup> In another example, gold nanoparticles were coated with cinnamon-based phytochemicals (linalool, catechin, or epicatechin). These agents had uptake in PC-2 and MCF-7 cells and were internalized in cancer cells to report photoacoustic signal.<sup>60</sup>

Cell surface receptor targeting is an area with interest and Luke et. al showed that molecularly activated plasmonic nanosensors could detect metastases at low levels of approximately 30 cells by targeting to the epidermal growth factor receptor.<sup>61</sup> Protease activity has been visualized with the use of black hole quencher 3 conjugated to NIR-absorbing copper sulfide nanoparticles which exhibited two absorption peaks at 630 nm and 930 nm.<sup>62</sup> When in the presence of matrix metalloproteinases in the tumor, the black hole quencher 3 was released leaving the copper sulfide nanoparticles.

Another powerful approach to nanoparticle coating is the use of lysed cell membranes. Although this has not yet been shown for photoacoustic imaging, Zhang et al. have shown that the membrane from lysed erythrocytes or cancer cells can be used to cloak nanoparticles similar to synthetic polymers.<sup>63-64</sup> These membranes retain all signaling components on the cell, and thus have significant utility in increasing circulation time and homing nanoparticles to target.

## **1.9 Conclusion**

Engraftment, migration, and retention concerns in emerging cell therapies can be answered using in vivo molecular imaging. Nanoparticles are useful in multimodal imaging because they have high and stable signal. Additionally, they can be to home the material to the site of interest.

## **1.10 Acknowledgments**

The authors are grateful for funding from the National Institutes of Health (HL 117048). The authors also thank the American Cancer Society Institutional Research Grant #14-250-42 provided through the Moores Cancer Center, University of California, San Diego.

Chapter 1, in part, is a reprint of the material as it appears in Wiley Interdisciplinary Reviews: Nanomedicine and Nanobiotechnology 2017. Lemaster, Jeanne, Jokerst, Jesse V. The dissertation author was the primary author of this chapter.

## CHAPTER 2: GADOLINIUM DOPING ENHANCES THE PHOTOACOUSTIC SIGNAL OF SYNTHETIC MELANIN NANOPARTICLES: A DUAL MODALITY CONTRAST AGENT FOR STEM CELL IMAGING

### 2.1 Introduction

Melanin is a natural pigment with myriad functions arising from its chemical structure including metal ion chelation, photo-protection, free radical quenching, and coloration<sup>65-69</sup>. In humans, melanins can serve as a biomarker for melanoma<sup>70-71</sup> and Parkinson's disease<sup>72</sup>. To exploit these properties, several groups have reported synthetic melanin nanoparticles (SMNPs) synthesized by the auto-oxidation of dopamine or *L*-3,4-dihydroxyphenylalanine<sup>68, 73</sup>. These materials have also been employed as contrast agents<sup>74-76</sup>. For example, SMNPs loaded with paramagnetic iron can act as efficient contrast agents for  $T_1$ -weighted MRI<sup>77-78</sup>. SMNPs also have a strong optical absorption in the near-infrared region<sup>76</sup>, and previous research has shown that melanins prepared from dopamine monomers provide photoacoustic signal<sup>79</sup>. Pristine and metal-doped polydopamine nanoparticles have shown excellent biocompatibility and biodegradability and can be used for combined therapy such as phototherapy, drug delivery, and imaging<sup>80-84</sup>—including stem cell imaging.

Stem cell imaging is an important tool for monitoring cell-based therapies<sup>85-86</sup>. MRI is one of the most common modalities for imaging cells and typically utilizes ferromagnetic inorganic nanoparticles<sup>87-94</sup>, stable paramagnetic complexes<sup>95</sup>, or gadolinium (Gd)-based chelates<sup>96-99</sup>. However, MRI is limited by long temporal resolution; acoustic and photoacoustic imaging can overcome this limitation with video frame rates<sup>100-101</sup>. Recently, we and others have reported photoacoustic cell imaging via Prussian blue-poly (1-lysine)<sup>100</sup>, iron-oxide based nanobubbles with 1,1'-dioctadecyl-3,3',3',3'-tetramethylindotricarbocyanine iodide<sup>102</sup>, exosome-like

silica nanoparticles<sup>103</sup>, biodegradable P<sub>2</sub>O<sub>5</sub>–CaO–Na<sub>2</sub>O phosphate-based glass nanospheres<sup>104</sup>, and phosphorylcholine-coated semiconducting polymers<sup>105</sup>. However, a multimodal probe with both MRI and photoacoustic imaging would have significant utility. Real-time photoacoustic imaging would provide a means for monitoring delivery, and deep tissue MRI would be used in tandem to provide longer-term follow-up of stem cell location and quantities, superimposed with anatomical information.

Thus, we prepared SMNPs via polymerization of *L*-3,4-dihydroxyphenylalanine and dopamine in the presence of Mn(III) using a recently developed metal-templated loading approach<sup>78</sup>. The data showed that using post-modification to chelate the Gd to the synthetic melanin particle surface led to a very low Gd-loading percentage; thus, we used the Mn displacement method for the synthesis of Gd-SMNP to yield high and tunable Gd loadings<sup>78</sup>. We then displaced the Mn from SMNPs with gadolinium to yield a dual, MRI/photoacoustic contrast agent due to the low binding affinity of Mn<sup>78, 106</sup>. Surprisingly, the gadolinium-loaded particles exhibited dramatically enhanced photoacoustic contrast over the metal-free SMNPs. We then prepared various metal-loaded SMNPs and investigated them for similar enhancements in photoacoustic contrast. We found that the photoacoustic signal of the SMNPs increases with incorporation of different metal ions with Gd(III) showing the highest signal intensities among SMNPs doped with Ni(II), Zn(II), Cu(II), Mn(III), or Fe(III). This discovery of enhanced photoacoustic signal due to gadolinium integration into the nanoparticles sets the stage for other multimodal imaging efforts.

## 2.2. Methods

*Reagents.* The following materials were acquired and used as received: dopamine hydrochloride (L-DOPA, Sigma-Aldrich), potassium permanganate (Thermo Fisher), hydrochloride (Sigma-Aldrich), ethanol (Sigma-Aldrich), ammonia (Sigma-Aldrich), nitric acid



(Sigma-Aldrich), tris base (Sigma-Aldrich), phosphate-buffered saline (PBS; Thermo Fisher), matrigel (Corning), ultraPure agarose (Thermo Fisher), and dimethyl sulfoxide (DMSO, Sigma-Aldrich).

*Instrumentation.* The size of the SMNPs was measured by dynamic light scattering (DLS) (Zetasizer-90, Malvern Instruments). TEM used a FEI Sphera microscope operating at 200 kV. Micrographs were recorded on a 2 K X2 KGatan CCD camera. Photoacoustic imaging was performed with the Vevo 2100 instrument (Visualsonics) with a 21 MHz-centered transducer as described previously<sup>58</sup>. This system utilizes a flashlamp pumped Q-switched Nd:YAG laser with an optical parametric oscillator and a second harmonic generator with wavelengths of 680 - 970 nm with a 1 nm step size and a pulse of 4-6 ns. The peak energy is  $45\pm 5$  mJ at 20 Hz at the source, the field-of-view is 14-23 mm, and the acquisition rate is 5 frames/second. The specimens were aligned at a depth of approximately 1 cm from the transducer. The laser was optimized prior to use with a built-in energy power software and meter. We used 100% laser energy with 10-20 dB gain and 21 MHz frequency. Photoacoustic spectra were collected from 680-970 nm and 3D scans were performed. The distance between the imaging transducer and phantom was maintained constant in each of the scans. We collected eight fields-of-view for each specimen. Absorbance measurements used a Shimadzu UV-3600 spectrophotometer. The metal concentration for the initial doped SMNP synthesis was quantified by inductively coupled plasma-optical emission spectrometry (ICP-OES) using a Perkin Elmer Optima 3000DV spectrometer. The metal concentration for MRI and Gd(III) retention was quantified by inductively coupled plasma-mass spectrometry (ICP-MS) using an Agilent 4500 series ICP-MS (Agilent Technology, Inc.).

*SMNP Nanoparticle Syntheses.* SMNP was prepared from dopamine according to a previously published method<sup>107</sup>. In a typical reaction, 50 mL of deionized water and 20 mL of

ethanol were fully mixed with 1.2 mL ammonia (28-30%) under constant stirring at room temperature for 1 h. Five mL of dopamine hydrochloride aqueous solution (4 mg/mL) was then quickly injected into this solution. The SMNPs were centrifuged and washed with deionized water 3 times to yield the final sample.

Metal-doped SMNPs were prepared according to published procedures<sup>77-78</sup>. Briefly, dopamine hydrochloride and metal salts were fully dissolved in 100 mL deionized water under stirring at room temperature for 1 h. Subsequently, 50 mL Tris aqueous (25 mM) solution was quickly injected into the solution. After another 1.5 h, the doped nanoparticles were centrifuged and washed three times with deionized water<sup>77</sup> at neutral pH. The Gd(III)-doped SMNP was prepared by employing an additional step using Mn(III)-doped SMNP<sup>13</sup>: 60 mg GdCl<sub>3</sub> was added to 10 mL Mn(III)-doped SMNP (2 mg/mL in solution) and stirred at room temperature overnight, separated by centrifugation, and washed three times with deionized water. To calculate the metal loading in the final product, an aliquot of each sample was added to a concentrated HNO<sub>3</sub> solution for overnight digestion. The solution was then diluted to 10 mL (1% HNO<sub>3</sub>) and analyzed by inductively coupled plasma optical emission spectroscopy (ICP-OES). The solution for MRI was digested in aqua regia for 1 h, diluted to 10 mL (2% HNO<sub>3</sub>), and analyzed by inductively coupled plasma mass spectroscopy (ICP-MS).

*Cell Culture.* Poietic human mesenchymal stem cells (hMSCs; Lonza, PT-2501) were grown in supplemented media (Lonza, PT-3001) and seeded in a T75 flask at a concentration of 5000 cells/cm<sup>2</sup>. These cells were labeled with nanoparticles and incubated under standard conditions. The hMSCs were washed three times with PBS to remove free nanoparticles and detached using TrypLE Express (Life Technologies). Cell viability was determined using 3-(4,5-dimethylthiazol-2-yl)-2,5-diphenyltetrazolium bromide for the MTT assay (Biotium). Ten  $\mu$ L of

MTT solution was added to 100  $\mu$ L of medium in each well, mixed briefly, and incubated at 37°C for 4 hours. Then, 200  $\mu$ L of DMSO was added to each well and pipetted to dissolve the resulting formazan salt. Absorbance was measured to 570 nm. The MTT assays were conducted by plating 8,000 cells/well in replicate (n=8) in 96 well plates and treated at varying timepoints (0-24 hrs) at a constant concentration (0.42 mg/mL) as well as at varying concentrations (0-0.84 mg/mL) at a constant time (4 hours) unless otherwise noted. Wells were analyzed in replicates (n=8).

*In vitro Photoacoustic Imaging and MRI Imaging.* For photoacoustic imaging of hMSCs, cells were labeled with nanoparticles and mixed in a 1% agar solution. The gain was set to 10-20 dB and read at a wavelength of 720 nm. Eight fields of view were collected for each sample. To measure the relaxivity of the Gd-SMNP, various concentrations of Gd-SMNP from 0 – 0.46 mM were prepared in a 1% agar solution. For the 4.7-T MRI, we used a MRS 4000 system from MR Solutions with a variable strength electromagnet set to 4.7-T. After scouting, we acquired T1 spin echo multi-slice images with horizontal phase encoding directions, FOVs of 60 mm, an echo time of 11 ms, repetition time of 720 ms, flip angle of 90°, a 512  $\times$  512 matrix, and autogain calibration. We acquired 12 slices with 1-mm thick slices. The  $\phi$  and  $\theta$  angle were set to zero for coronal slices with no echo asymmetry. The T1 reciprocal was plotted as a function of concentration from 0.046 -0.46 mM. For the 7T MRI, we used a Bruker 7.0 T magnet with Avance II hardware. After scouting, we acquired T1 spin echo multi-slice images with horizontal phase encoding directions, FOVs of 6.91/3.12 cm, an echo time of 1/1, repetition time of 750 ms, flip angle of 90°, and a 256  $\times$  116 matrix. We acquired 6 slices with 2-mm thickness. The T1 reciprocal was plotted as a function of concentration from 0.046 -0.46 mM.

*In vivo Photoacoustic Imaging and MRI Imaging.* 500,000 Gd(III)-SMNP-labeled hMSCs were injected in a 50% matrigel mixture in the left ventricle (LV) wall of nude mice.

Control mice were injected with a PBS/matrigel solution only. Echocardiograms were performed in the long axis (lax) mode. MRI was performed before injection and 15 minutes after injection with labeled hMSCs.

*Data analysis.* ImageJ 1.48 v58 was used to quantitate the photoacoustic signal for the SMNPs via region of interest (ROI) analysis for the average integrated density in arbitrary units (bit depth) using the maximum intensity projection for 8-bit images<sup>108</sup>. The photoacoustic means and standard deviations were calculated from eight fields-of-view in each sample. The error bars represent the standard deviation of the measurements unless otherwise noted.

## **2.3. Results and Discussion**

### **2.3.1 Synthesis and Characterization.**

Three types of SMNPs were used in these studies: (1) SMNP prepared by polymerization of dopamine (SMNP)<sup>107</sup>; (2) Metal-doped SMNP made by polymerization of dopamine in the presence of metal salts; and (3) Gd(III)-doped SMNP made via a metal exchange method beginning with a Mn(III) doped SMNP as a template (**Figure 2.1**)<sup>77-78</sup>. The synthesis began with the polymerization of dopamine (**Figures 2.1A, 2.1B**) to form spherical particles. Previous research has shown that the high metal binding capacities and fast binding rate of synthetic melanin nanoparticles compared to melanin polymers is due to the higher surface area to volume ratio<sup>73</sup>. The morphology of these nanoparticles was characterized by transmission electron microscopy (TEM) (**Figures 2.1C, 2.1D, Supplementary Figure S1**). All samples were spherical and monodisperse: Dynamic light scattering (DLS) (**Figure 2.1, Supplementary Figure S2**) showed

that the size of the SMNPs was 150 nm with a polydispersity index (PDI) of 0.11 +/- 0.03 (**Figure 2.1E**). The size of the Gd(III)-doped SMNP was 160 nm with a PDI of 0.18 +/- 0.03 (**Figure 2.1F**).

The concentration of metals ranged from 5.9-8.3% by weight with respect to the polydopamine as determined by ICP-OES (**Table 2.1**). Although the synthetic conditions were optimized for achieving uniform size and high loadings, there were slight variations in particle size and metal loading concentration. This is likely due to the changes in affinities and coordination geometries between dopamine and different metal ions that may significantly affect polymerization kinetics<sup>109</sup>. The zeta potential of Mn-SMNP was -10.7 mV while the zeta potential of the Gd(III)-doped SMNP was -9.5 mV.

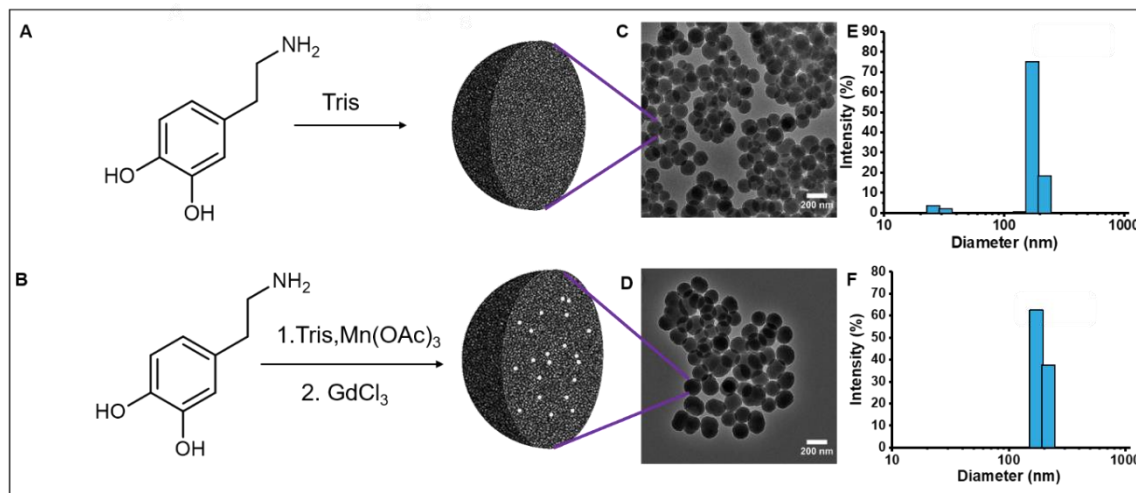


**Figure 2.1** Synthesis and characterization of synthetic melanin nanoparticles (SMNP). **A**) Molecular structure of dopamine and route to nanoparticles, **B**) synthesis of Gd(III)-doped SMNP, **C**) TEM micrograph of SMNP shows spherical morphology and uniform size, **D**) TEM micrograph of Gd(III)-doped SMNP shows spherical morphology and uniform size, **E**) DLS indicates a low dispersity solution and a particle size of 150 nm for SMNP, **F**) DLS data indicates a particle size of 160 nm for Gd(III)-doped SMNP.

**Table 2.1. ICP-OES measurements of metal-doped SMNP.** Metal loading varies from 5.9-8.3% by weight for metal-doped SMNP samples.

Sample	Metal Loading (Weight %)
Mn(III)-doped SMNP	6.0
Fe(III)-doped SMNP	5.9
Ni(II)-doped SMNP	5.9
Cu(II)-doped SMNP	6.2
Zn(II)-doped SMNP	8.3
Gd(III)-doped SMNP	6.4

### 2.3.2 Photoacoustic and MRI Performance.

The photoacoustic spectra of SMNP and metal-doped (Ni(II), Zn(II), Cu(II), Mn(III), Fe(III), and Gd(III)) SMNP indicated a broad peak across all samples from 720 nm – 760 nm (**Figure 2.2A**) with Gd(III)-SMNP showing the highest photoacoustic intensity amongst all samples from 680-850 nm. Photoacoustic imaging at 720 nm of SMNP and metal-doped SMNP (**Figures 2.2B-C**) showed that the gadolinium-based material exhibited the highest photoacoustic signal intensity at neutral pH (all samples 0.58 mg/mL with respect to polydopamine). This effect correlates with absorbance spectroscopy where Gd(III)-SMNP exhibits the strongest absorbance from 700-900 nm (**Figure 2.2D**). Miao et. al also showed that metal-chelated polydopamine nanoparticles show higher absorbance than polydopamine nanoparticles between 700-900 nm<sup>110</sup>. Importantly, a solution of GdCl<sub>3</sub> alone (no nanoparticles) had no absorbance (**Supplementary Figure S3**). Other lanthanides also produce a photoacoustic signal increase relative to metal-free SMNPs (**Supplementary Figure S4**). The Ce-doped SMNP had the highest photoacoustic signal of  $6 \times 10^4 \pm 1 \times 10^3$  a.u. while Er-doped had the lowest photoacoustic signal of  $9 \times 10^4 \pm 8 \times 10^2$  a.u.; however, Gd was used for further studies because Gd-based contrast agents also have high MRI signal<sup>96-99</sup>. Additionally, lanthanide-doped nanoparticles have been used in luminescent

imaging due to long luminescent lifetimes, large ranges of upconversion luminescent wavelengths, and high signal-to-noise ratios<sup>11</sup>.

To further understand the activatable nature of this phenomenon, we monitored the photoacoustic signal in real-time while adding Gd(III) to the manganese-loaded nanoparticles (**Figure 2.2E**). In aqueous solution, Gd(III) has low absorbance from 400-900 nm (**Supplementary Figure S3**). We initially observed a 2-fold intensity increase upon addition of Gd(III) (**Figure 2.2F**); the signal increased 16-fold with further mixing (**Figure 2.2G**, **Supplementary Video 1**).

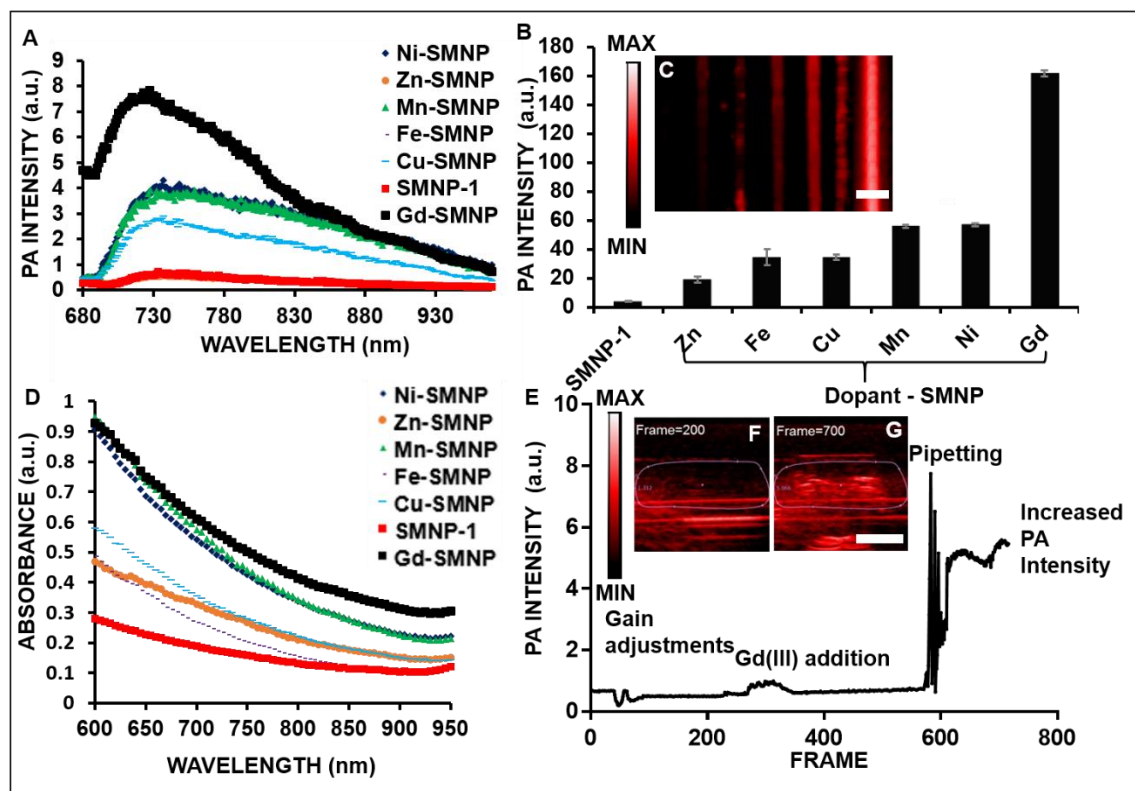


**Figure 2.2 Photoacoustic (PA) imaging and intensity data of SMNP and metal-doped SMNP.** **A)** Photoacoustic spectra from 680-970 nm indicates a broad peak for all nanoparticle samples from 720-760 nm. **B)** Gd(III)-SMNP has the highest photoacoustic signal of nanoparticles doped with Ni, Zn, Cu, Mn, Fe, or Gd. The Gd(III)-doped SMNP showed the highest photoacoustic signal and SMNP without doping showed the lowest signal. **C)** Photoacoustic imaging intensity of SMNP and metal-doped SMNP (Ni, Zn, Cu, Mn, Fe, and Gd). **D)** Absorbance data of SMNP and metal-doped (Ni, Zn, Cu, Mn, Fe, Gd-doped) SMNP indicated Gd(III) had the highest absorbance from 700-950 nm. **E)** Quantification of photoacoustic imaging intensity for live doping of Mn(III)-SMNP with Gd(III). Mn(III)-SMNP was used to increase the Gd(III) loading via Mn-Gd ion exchange to observe the photoacoustic intensity change in real-time with mixing via pipetting. The photoacoustic intensity shows a change in signal upon addition of Gd(III) (1 mg/mL) to Mn(III)-doped SMNP (0.68 mg/mL); **F)** and **G)** Snapshots from the in situ photoacoustic movie at frames 200 and 700, respectively.

To evaluate stability, photoacoustic signal from SMNPs was studied under continuous laser irradiation (pulse duration of 5 ns; 0.167 seconds between pulses) and showed constant signal over 15 minutes. The signal difference between the first 100 frames and the last 100 frames is 6.6% indicating that the SMNPs are stable under photoacoustic irradiation (**Supplementary Figure S5A**).



The photoacoustic signal intensity of Gd(III)-doped SMNP is dependent on the concentration of both SMNP and Gd(III). The Gd(III)-doped SMNP was measured from 0.068 – 0.68 mg/mL of nanoparticles and exhibited a linear increase ( $R^2 = 0.96$ ) with increasing SMNP concentration (**Figures 2.3A**). Methylene blue (MB, 0.4 mM) was a positive control<sup>112-113</sup>, and deionized water and Gd(III) solution (40 mg/mL) in water were negative controls. At higher concentrations of SMNP, the photoacoustic intensity with respect to SMNP continued to increase linearly from 0-3.5 mg/mL with  $R^2 = 0.98$  (**Supplementary Figure S5B**).

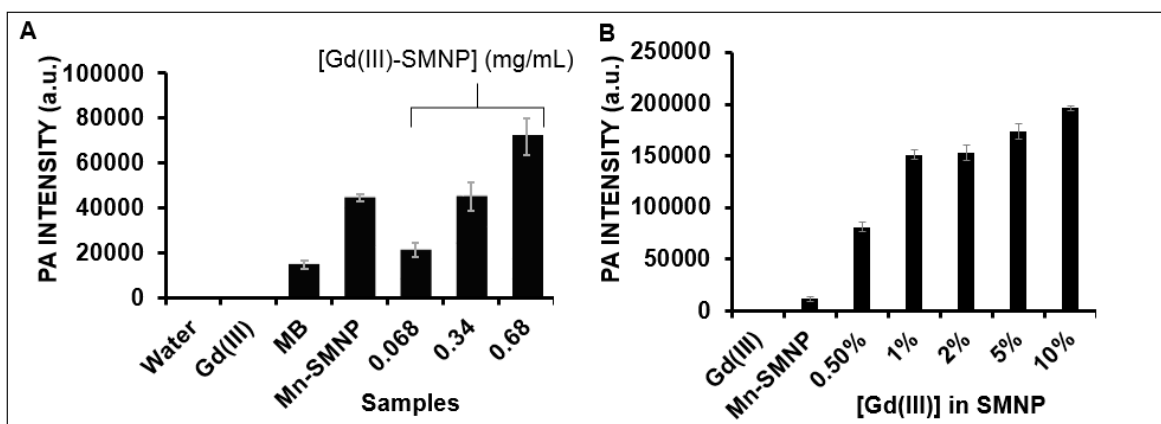


**Figure 2.3 Photoacoustic (PA) intensity of Gd(III)-doped SMNP particles is dependent on the concentration of SMNP and Gd(III).** **A)** Photoacoustic intensity data where 0.68, 0.34, and 0.068 represents the 5% Gd-SMNP concentrations (mg/mL). Mn(III)-SMNP without Gd(III) doping (0.68 mg/mL), MB (0.4 mM), H<sub>2</sub>O, and Gd(III) (40 mg/mL) are controls. **B)** Photoacoustic intensity data with constant Mn-SMNP concentration where 0.5% - 10% represent the concentration of Gd(III) in Mn-SMNP. Nanoparticle concentration for all is 0.2 mg/mL. The error bars represent the standard deviation of the ROIs (n=8).

This photoacoustic signal enhancement is likely due to an improved absorption cross-section via melanin coordination of the metal ions via catechol groups—this leads to increased absorption<sup>114</sup>. Indeed, the absorption (**Supplementary Figure S5C**) was higher for 5% and 10% Gd-SMNP compared to Mn-SMNP and 0.5 – 2% Gd-SMNP. The photoacoustic signal (**Figure 2.3B**) also increased with Gd(III) loading when the SMNP concentration was held constant. Photoacoustic signal is proportional to concentration. Related work has shown the presence of vinylene bonds to increase the mass absorption coefficient and photothermal conversion efficacy in polymers<sup>115</sup>. Related work has increased the photoacoustic signal of nanoparticles via the addition of a silica coat to gold nanorods or semi-conductor

polymer nanoparticles. This is because the silica shell has a lower thermal conductivity and heat capacity than water. Thus the coated particles achieve a higher temperature than bare particles leading to a higher thermal gradient and a higher photoacoustic signal<sup>57, 116-117</sup>.

The Gd(III)-SMNP was also studied in terms of MRI parameters. The  $r_1$  was  $3.35 \text{ mM}^{-1} \text{ s}^{-1}$  and  $2.90 \text{ mM}^{-1} \text{ s}^{-1}$  for 4.7 T and 7.0 T fields, respectively (**Supplementary Figure S6A-D**). These values are similar to commercially available agents, Gd-DOTA and Gd-DTPA<sup>118-119</sup>. Additionally, Gd(III)-SMNP subcutaneous injections were performed in mice (**Supplementary Figures S6E-F**), showing enhanced photoacoustic signal after injection with Gd(III)-SMNP.

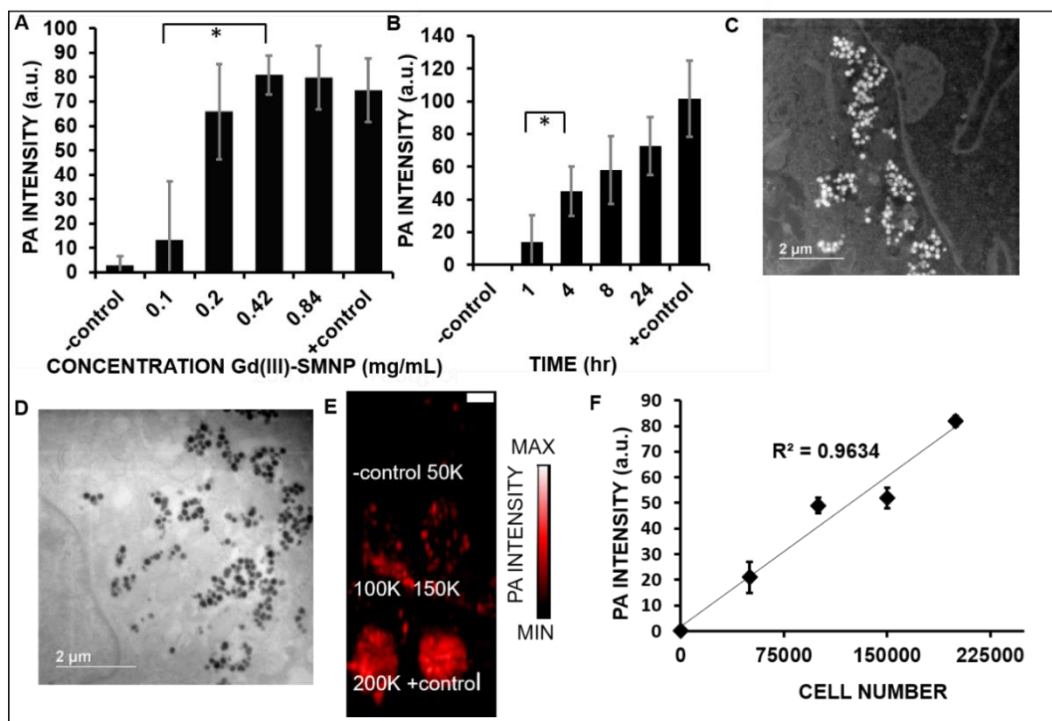


**Figure 2.4 Optimization of hMSC Labeling Parameters.** **A)** Increasing concentrations of nanoparticles (0.1 – 0.84 mg/mL) of Gd(III)-SMNP were used to label 150,000 hMSCs; the photoacoustic signal increased accordingly. For panels **A** and **B**, unlabeled hMSCs were the negative control. Gd(III)-SMNP (0.152  $\mu\text{mol/mL}$  Gd(III)) was the positive control.) **B)** The effect of incubation time on photoacoustic intensity of 150,000 hMSCs treated with 0.42 mg/mL of Gd(III)-SMNP. The photoacoustic intensity increased as time increased from 1-24 hours. \* Indicates p-value <0.05. **C)** Dark field STEM of hMSCs treated with Gd(III)-SMNP (4 hrs, 0.42 mg/mL), where the white dots indicate the Gd(III)-SMNP. **D)** TEM microscopy of hMSCs treated with Gd(III)-SMNP (4 hrs, 0.42 mg/mL) where the black dots indicate the Gd(III)-SMNP. **E)** Photoacoustic imaging data of hMSCs labeled with Gd(III)-SMNP particles. The photoacoustic intensity increased with increasing incubation time from 1 – 24 hrs suggesting increased internalization of the particles with increasing time. The scale bar represents 1 cm. **F)** Photoacoustic intensity data of 0 – 200,000 hMSCs labeled with Gd(III)-SMNP particles showed a linear relationship between cell number and photoacoustic intensity.

### 2.3.3 Cellular Imaging.

hMSC uptake of Gd(III)-SMNPs was measured to determine the optimal concentration and time for cell labeling<sup>120-121</sup>. The photoacoustic intensity was quantified for  $1.5 \times 10^5$  cells treated with 0-0.84 mg/mL of Gd(III)-SMNP at 8 hours of incubation time (**Figure 2.4A**). No further increase was seen after 0.42 mg/mL. We then studied the effect of time. The photoacoustic intensity of  $1.5 \times 10^5$  cells treated with 0.42 mg/mL of Gd(III)-SMNP particles at varying times (1-24 hours) was quantified (**Figure 2.4B**). The hMSCs labeled with 0.42 mg/mL Gd-SMNP had 8-fold higher photoacoustic signal than hMSCs labels with 0.1 mg/mL Gd-SMNP. hMSCs labeled for 4 hours with Gd-SMNP showed 3-fold higher photoacoustic intensity than cells treated with 1 hour of Gd-SMNP ( $p < 0.05$ ). An MTT assay revealed no significant difference ( $p$ -value  $> 0.05$ ) in cell viability of cells treated with up to 0.84 mg/mL of Gd(III)-SMNP (**Supplementary Figure S7**) suggesting good biocompatibility. Therefore, 4 hours of incubation with 0.42 mg/mL of Gd(III)-SMNP was determined to be the optimal incubation time without adverse effects on cell viability. Our prior work showed that there was no significant release of the Gd(III) ion from the SMNP over 7 days after incubation with  $\text{CaCl}_2$  and  $\text{ZnCl}_2$  solutions for 7 days as measured by ICP<sup>78</sup>. We repeated this experiment and found that 97.9% of Gd(III) was retained in the particle after 7 days of incubation in water at room temperature as measured by ICP.

Dark field scanning transmission electron microscopy (STEM), transmission electron microscopy (TEM), and bright field microscopy were used to confirm uptake of Gd(III)-SMNP in hMSCs (**Figures 2.4C-D** and **Supplementary Figures S8-S9**). Previous studies have shown mesoporous silica uptake in hMSCs from 1 - 4 hours<sup>122</sup> similar to our observed uptake of Gd(III)-SMNP in hMSCs. Parameters such as charge, composition, surface reactivity, and surface adsorption have been implicated in affecting the time of nanoparticle uptake in cells<sup>123</sup>.

Polydopamine-containing nanoparticles have shown good biocompatibility and are cleared from the body via the reticuloendothelial system<sup>80</sup>. PEGylation was not necessary because intravenous injection was not performed; the cells were labeled with the nanoparticles *ex vivo*, and the cells were then implanted into the myocardium. Photoacoustic images and imaging intensity of 0-200 K cells indicated a linear relationship ( $R^2 = 0.96$ ) between cell number and photoacoustic intensity (**Figures 2.4E-F**). The lowest number of cells we measured was  $5.0 \times 10^4$  and we calculated the lowest detectable number of cells to be  $2.3 \times 10^4$  based on three standard deviations above the background mean. Previous research reported cell detection limits varying from single cells -  $10 \times 10^4$  cells in MRI and photoacoustic imaging<sup>58, 124-125</sup>. However, achieving ultra-low detection limits is rarely clinically useful because human trials routinely use  $10^6$ - $10^8$  cells<sup>126-128</sup>.

We next conducted additional studies to understand what effects labeling has on the cells' biology. CD75, CD90, and CD105 were used as hMSC marker proteins for flow cytometry analysis. Analysis showed that the labeled hMSCs still express these three stem cell surface markers (**Supplementary Figures S10A-C**). However, the expression of CD90 in the labeled cells was 16% less than the expression of CD75 in the control cells suggesting that the SMNP labeling may be affecting the expression of CD75. The proliferation of unlabeled and labeled hMSCs was also measured over time. hMSCs were labeled by incubation with Gd(III)-SMNP for 4 h. Cells continued to proliferate for 3 weeks after labeling with the nanoparticles (**Supplementary Figure S8E**). Although labeled cells proliferated approximately 26% slower than the unlabeled hMSCs, both the labeled and unlabeled hMSCs doubled in approximately 3 days (**Supplementary Figure S11**). While chelation increases the biocompatibility of Gd-based agents<sup>129</sup>, it is possible that free Gd is present as cells internalize the particles, which may act to slow proliferation and affect the expression of marker proteins<sup>130</sup>.

Finally, *in vivo* experiments using 500,000 cells labeled with Gd(III)-SMNP particles were performed in mice (**Figure 2.5**). Bone marrow mononuclear cells has been found to promote heart function and neovascularisation after myocardial infarction via intramyocardial injection delivery<sup>131</sup>. Echocardiograms pre- and immediately post-injection are also shown in **Figure 2.5** and indicate that the photoacoustic signal increased 64-fold +11.3. Transverse MRI images pre- and post-injection show that the MRI signal increased 2.0-fold +/- 0.17 versus baseline (**Fig. 2.5C, D**).

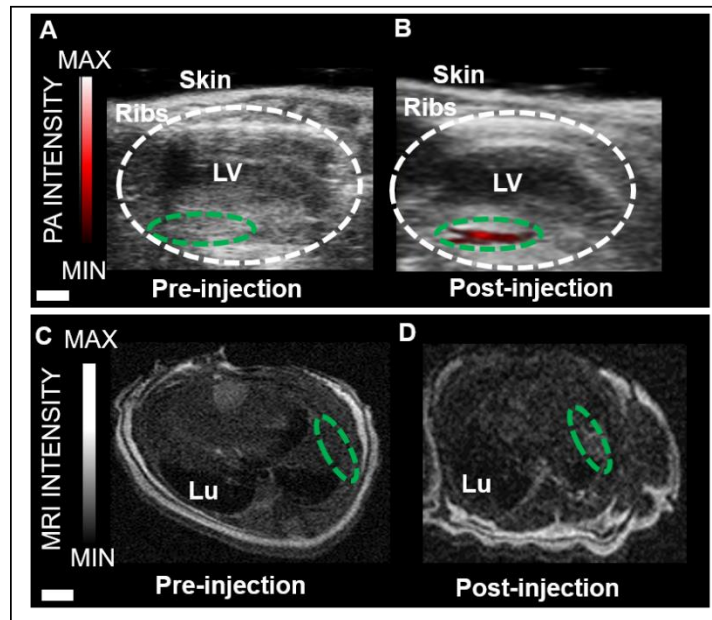


**Figure 2.5. Photoacoustic and MR imaging of Gd(III)-SMNP implanted into mouse hearts.** **A)** Photoacoustic imaging of longitudinal axis view of live mouse heart pre-injection. The area circled in white represents the left ventricle (LV). The area circled in green represents the area of the left ventricle wall before injection. **B)** Photoacoustic imaging of the longitudinal axis view of a live mouse heart post-injection. 500,000 hMSCs labeled with Gd(III)-SMNP were injected. The green-circled area shows the increase in photoacoustic imaging intensity (red). **C)** Transverse MRI view of a mouse heart pre-injection. The green-circled area represents the LV wall. Lu is the lung. **D)** Transverse MRI view of a mouse heart post-injection. 500,000 hMSCs labeled with Gd(III)-SMNP were injected. The green-circled area shows the increase in MRI signal intensity in the LV wall.

## 2.4. Conclusion

This study details a synthetic melanin-based contrast agent for photoacoustic imaging and MRI. The most important finding is that the photoacoustic intensity increased dramatically upon incorporation of metal ions into the polydopamine-based nanoparticles. Chelation is known to increase the biocompatibility of Gd-based contrast agents<sup>129</sup> and Gd-based contrast agents are clinically used in MRI<sup>132-133</sup>. We used the Gd(III)-enhanced photoacoustic signal to image stem cells *in vivo* coupling this modality with MRI. The labeled stem cells still expressed stem cell surface markers and continued to proliferate.

## 2.5 Author Contributions

The manuscript was written through contributions of all authors. All authors have given approval to the final version of the manuscript. ‡These authors contributed equally.

## 2.6 Acknowledgements

J.E.L. acknowledges funding from the National Institutes of Health (NIH) Institutional National Research Service Award T32 CA153915, Cancer Researchers in Nanotechnology. J.V.J. acknowledges funding from the NIH (Grants R00 HL117048 and DP2 HL137187) and infrastructure from Grant S10 OD021821. This work was performed, in part, at the San Diego Nanotechnology Infrastructure of UCSD, a member of the National Nanotechnology Coordinated Infrastructure, which is supported by the National Science Foundation (Grant ECCS-1542148). This work made use of the EPIC facility of Northwestern University's NUANCE Center, which has received support from the Soft and Hybrid Nanotechnology Experimental (SHyNE) Resource (NSF ECCS-1542205); the MRSEC program (NSF DMR-1121262) at the Materials Research Center; the International Institute for Nanotechnology (IIN); the Keck Foundation; and the State of Illinois, through the IINNotes.

Chapter 2, in full, is a reprint of the material as it appears in Chemistry of Materials, 2018, Lemaster, Jeanne E., Zhao Wang, Ali Hariri, Fang Chen, Ziyang Hu, Yuran Huang, Christopher V. Barback, Richard Cochran, Nathan C. Gianneschi, and Jesse V. Jokerst. The dissertation author was the co-first author of this paper.

## 2.7 Appendix

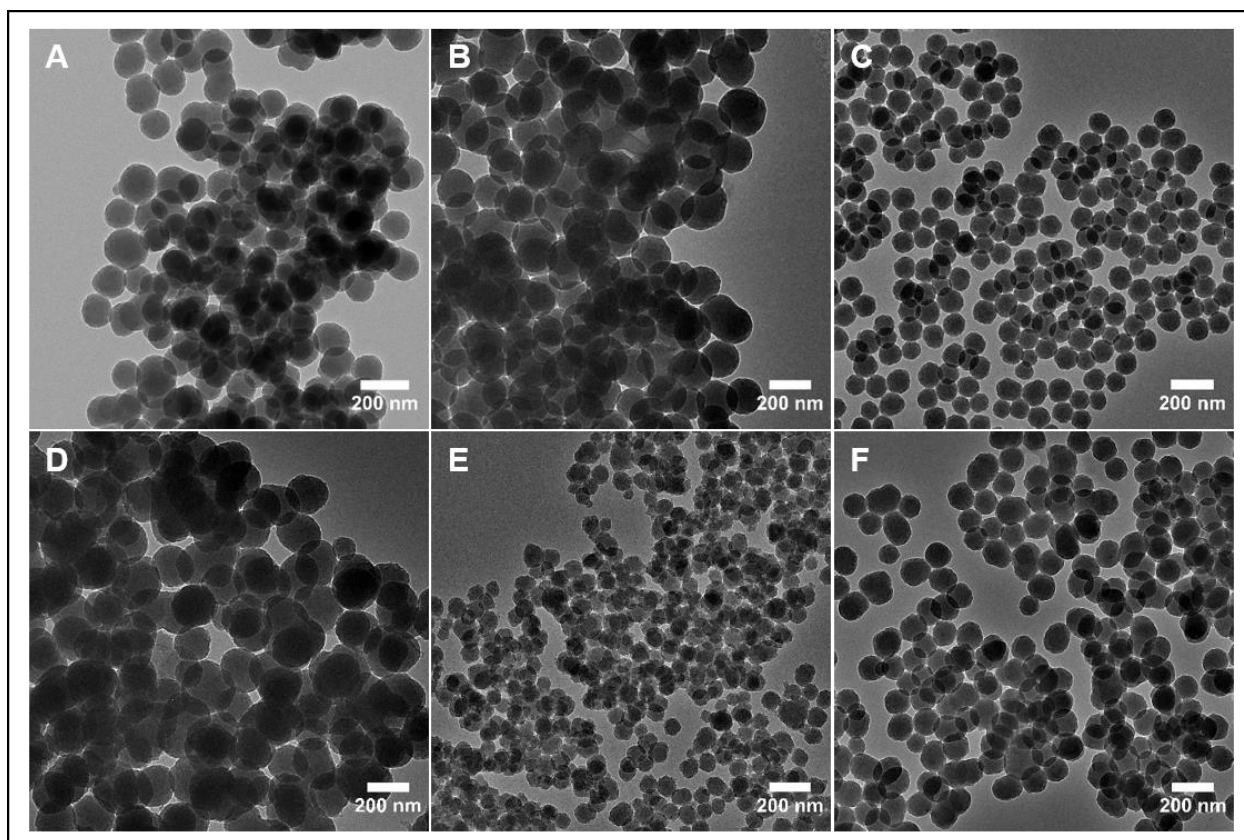


**Figure S1. Representative TEM images show spherical shape and uniform size distribution of synthetic melanin nanoparticles. A)** SMNP made by polymerization of L-3,4-dihydroxyphenylalanine. **Figures B-F** show metal-doped SMNPs. **B)** Mn-doped SMNP, **C)** Fe-doped SMNP, **D)** Ni-doped SMNP, **E)** Cu-doped SMNP, and **F)** Zn-doped SMNP.

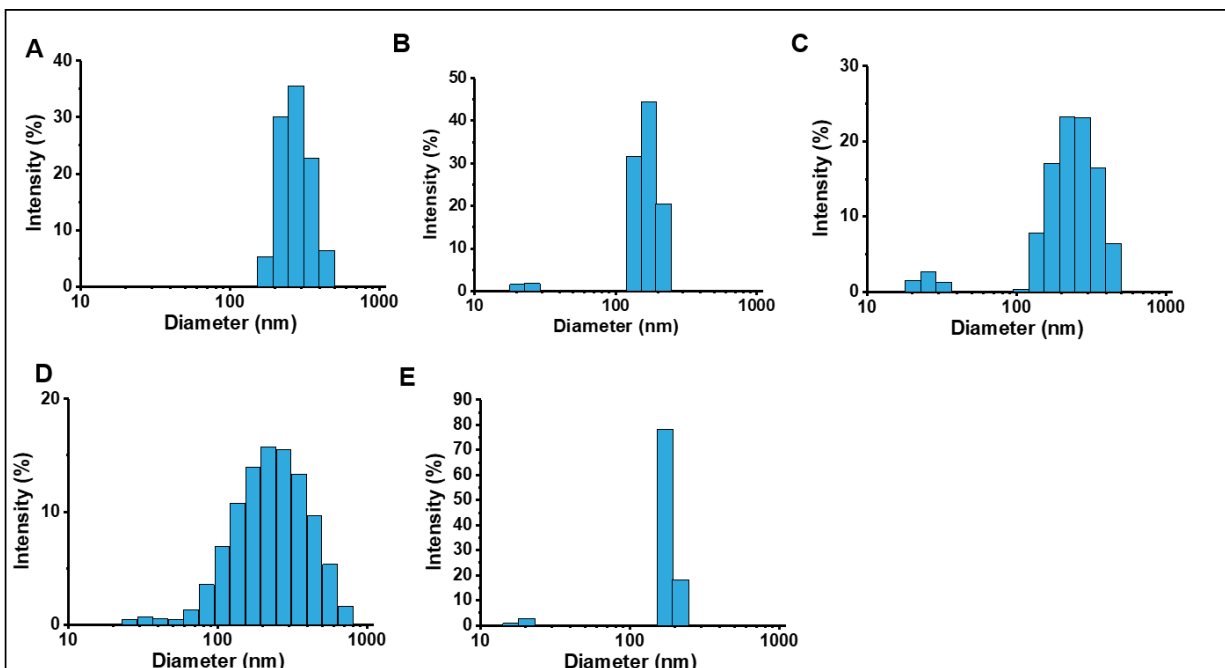


**Figure S2. Representative DLS data show size distribution of synthetic melanin nanoparticles. Figures A-F show metal-doped SMNPs. A) Mn-doped SMNP, B) Fe-doped SMNP, C) Ni-doped SMNP, D) Cu-doped SMNP, and E) Zn-doped SMNP.**



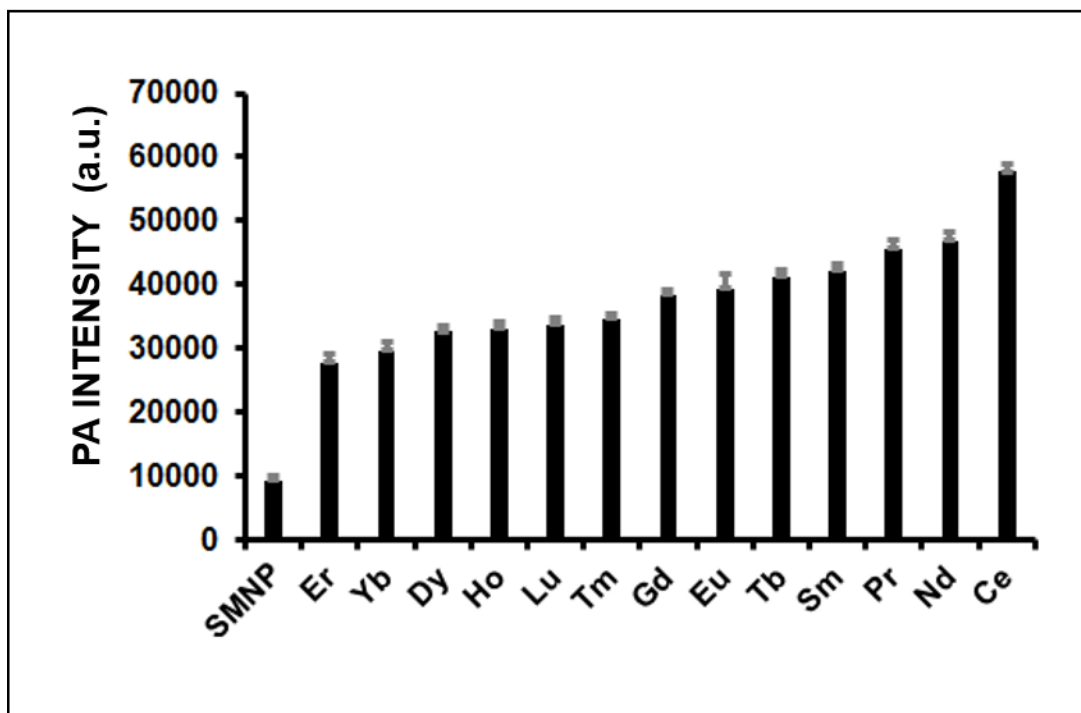


**Figure S3. PA intensity data of lanthanide-doped SMNPs.** Ce-doped SMNP had the highest PA signal of 57,766.6 +/- 1,073.5 while Er-doped had the lowest PA signal of 9,375.6 +/- 838.2 of the lanthanide-doped samples. Error bars represent the standard deviation (n=8).

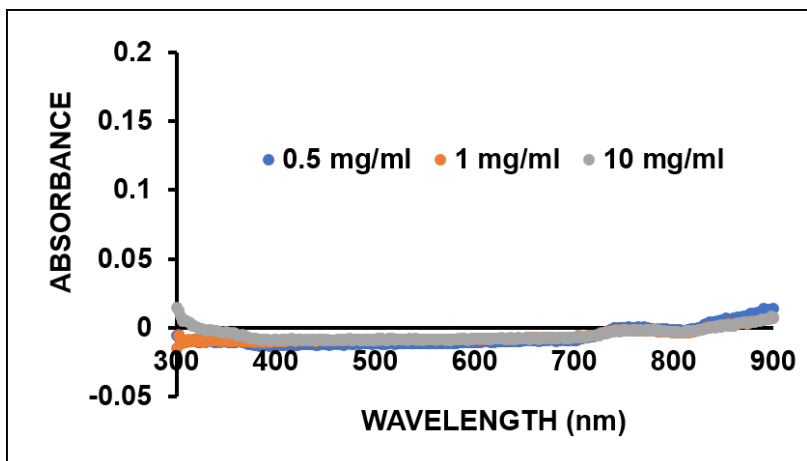


**Figure S4. Absorbance of Gd(III) solution.** Gd(III) was dissolved in water at 0.5 mg/ml, 1 mg/ml, and 10 mg/ml and showed low absorbance from 300-900 nm.

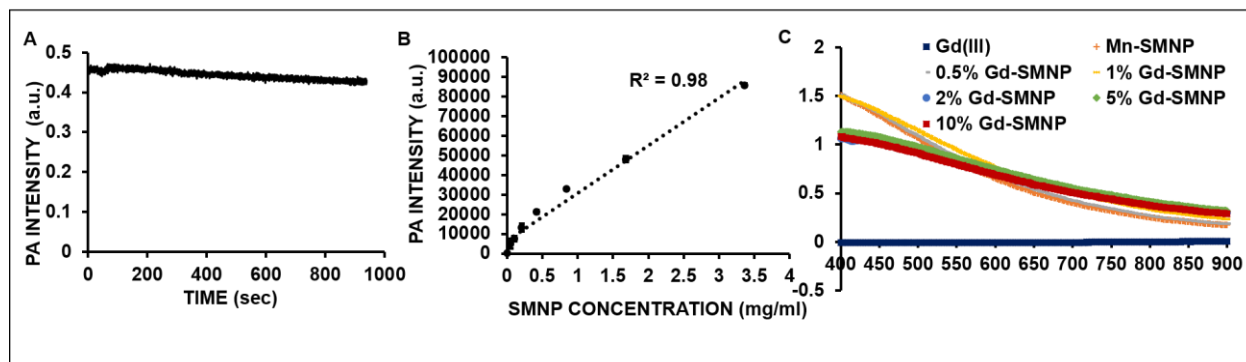


**Figure S5.** **A)** The PA signal difference between the first 100 frames and the last 100 frames is 6.6% indicating that the SMNPs are stable under photoacoustic irradiation. **B)** There is a linear relationship of PA signal based on SMNP concentration measured from 0-3.5 mg/mL. **C)** The absorbance of 5% and 10% Gd-SMNP was higher from 600-900 nm than Mn-SMNP and 0.5 – 2% Gd-SMNP.

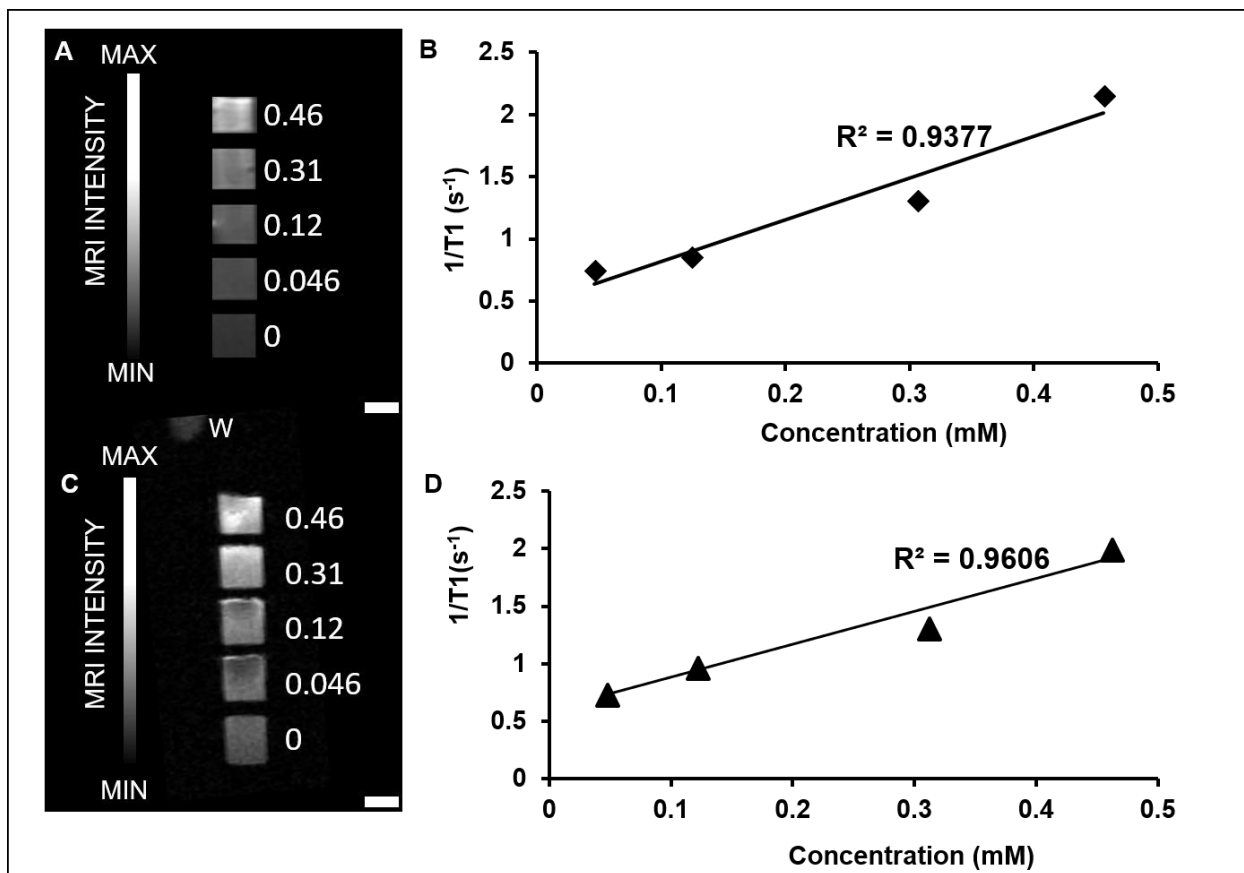


**Figure S6. MRI data of Gd(III)-SMNP.** **A)** MRI of Gd(III)-SMNP particles in 4.7 T. **B)**  $1/T_1$  ( $s^{-1}$ ) vs Concentration (mM) for 4.7T field. **C)** MRI of Gd(III)-SMNP particles in 7 T. **D)**  $1/T_1$  ( $s^{-1}$ ) vs Concentration (mM) for 7 T field. Scale bar = 2 mm.

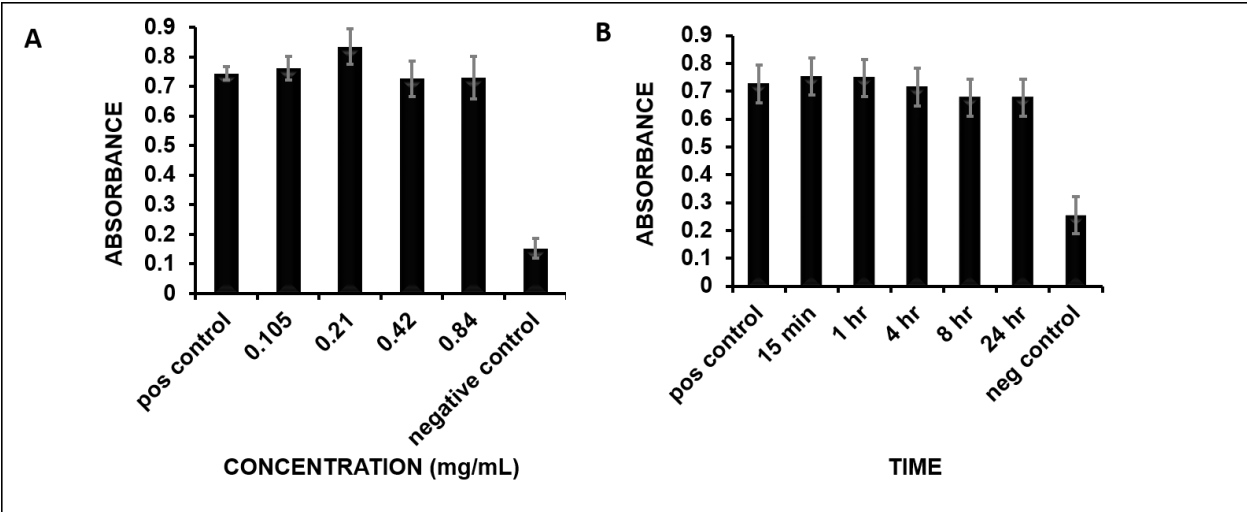


**Figure S7. MTT assays of Gd-SMNP labeled hMSCs. A)** Cell viability was not affected by increasing the concentration from 0.105 – 0.84 mg/mL of Gd(III)-SMNP. **B)** Cell viability decreased approximately 7% after 24 hours of treatment with Gd(III)-SMNP (0.42 mg/mL). The positive (pos) control was unlabeled cells. The negative (neg) control was cells treated with 70% ethanol. The error bars represent the standard error. N = 6.

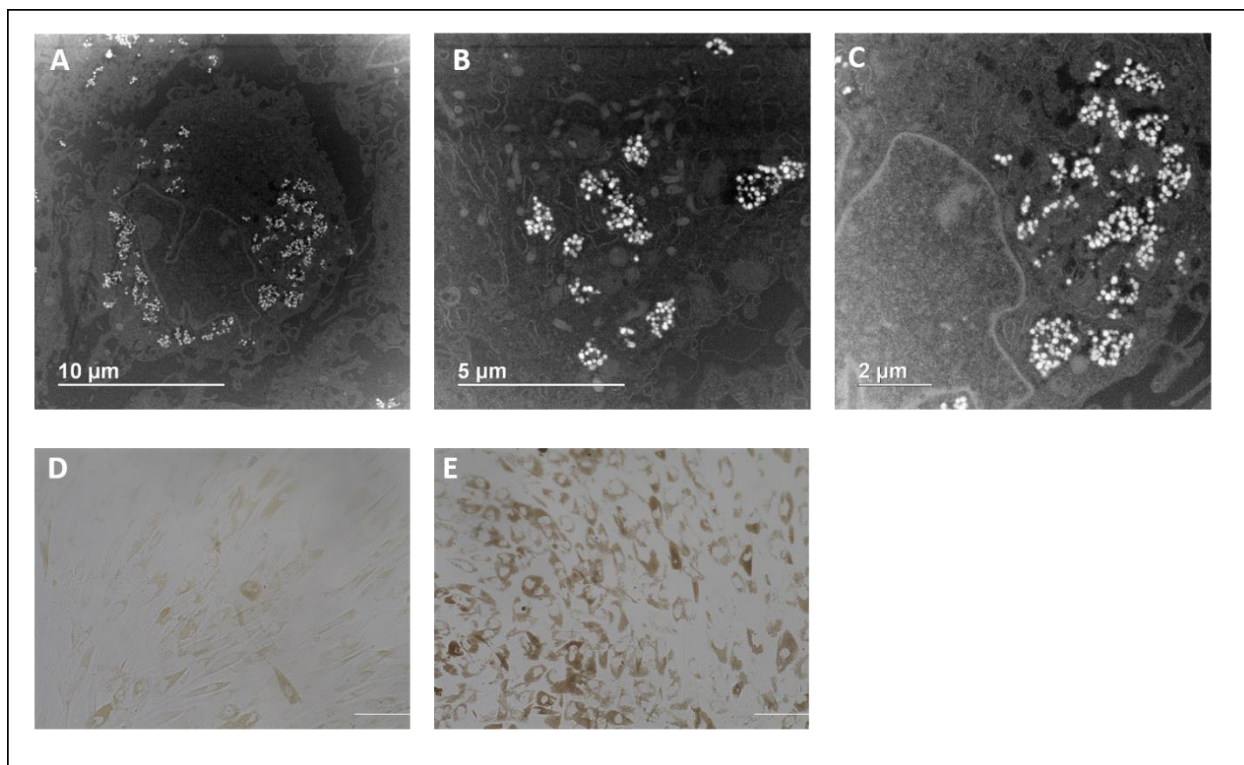


**Figure S8. Dark Field STEM microscopy and optical microscopy show internalization of nanoparticles.** **A-C)** Dark field STEM microscopy of hMSCs labeled with Gd-SMNP (4 hrs, 0.42 mg/mL). The Gd-SMNP particles (white spheres) are located in the in the cytoplasm of cells. **D)** Brightfield microscopy of unlabeled hMSCs. **E)** Brightfield microscopy of hMSCs labeled with Gd-SMNP (4 hrs, 0.42 mg/mL). The cells continued to proliferate for 3 weeks when labeled with Gd-SMNP. Scale bar = 200  $\mu\text{m}$ .

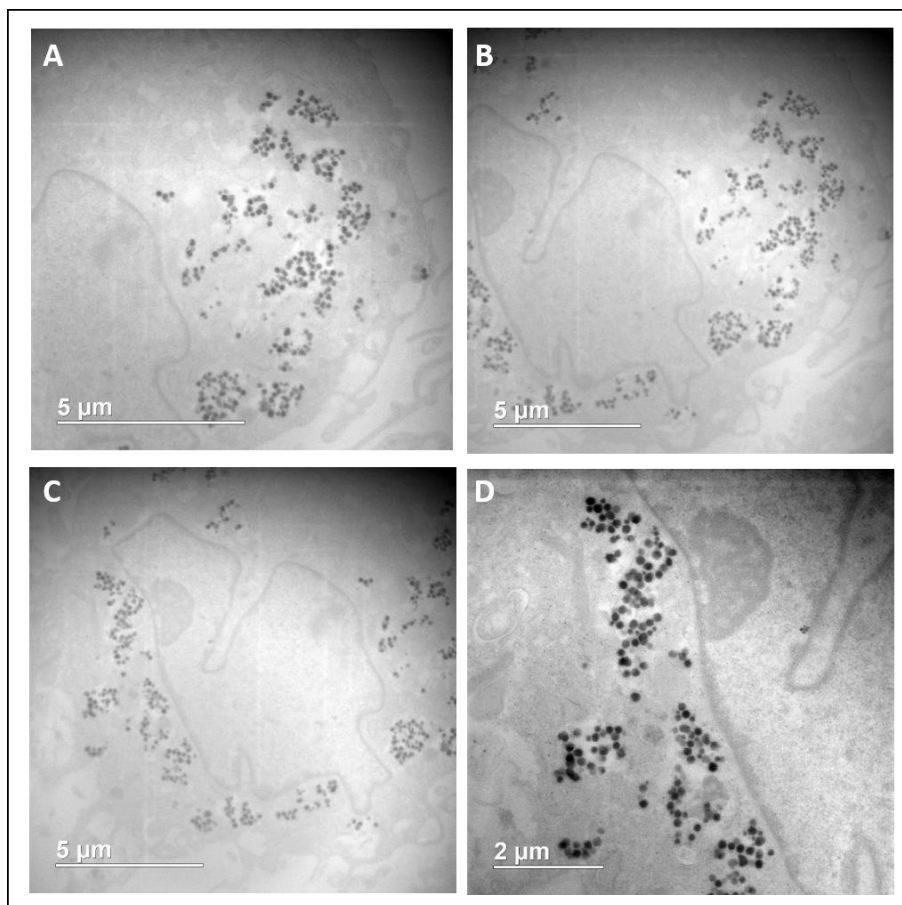


**Figure S9.** Figures A-D show TEM microscopy of hMSCs treated with Gd(III)-SMNP (4 hrs, 0.42 mg/mL). The Gd(III)-SMNP particles (black spheres) are located in the cytoplasm of cells.

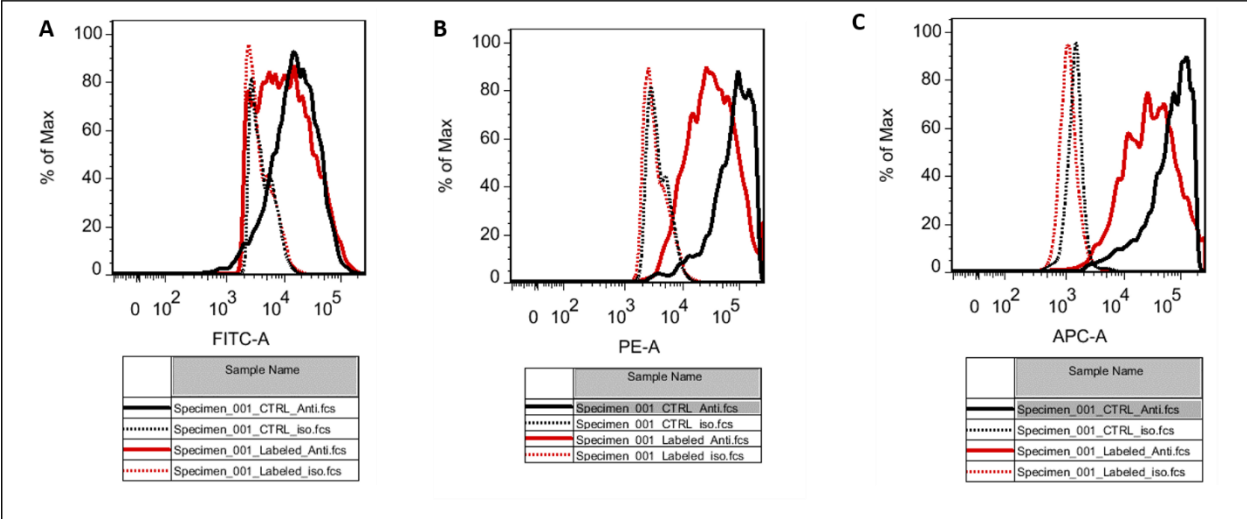


**Figure S10. Flow cytometry data of hMSCs labeled with 0.42 mg/mL of- Gd(III)-SMNP. A) CD90-FITC, B) CD75-PE, and C) CD105-APC.**



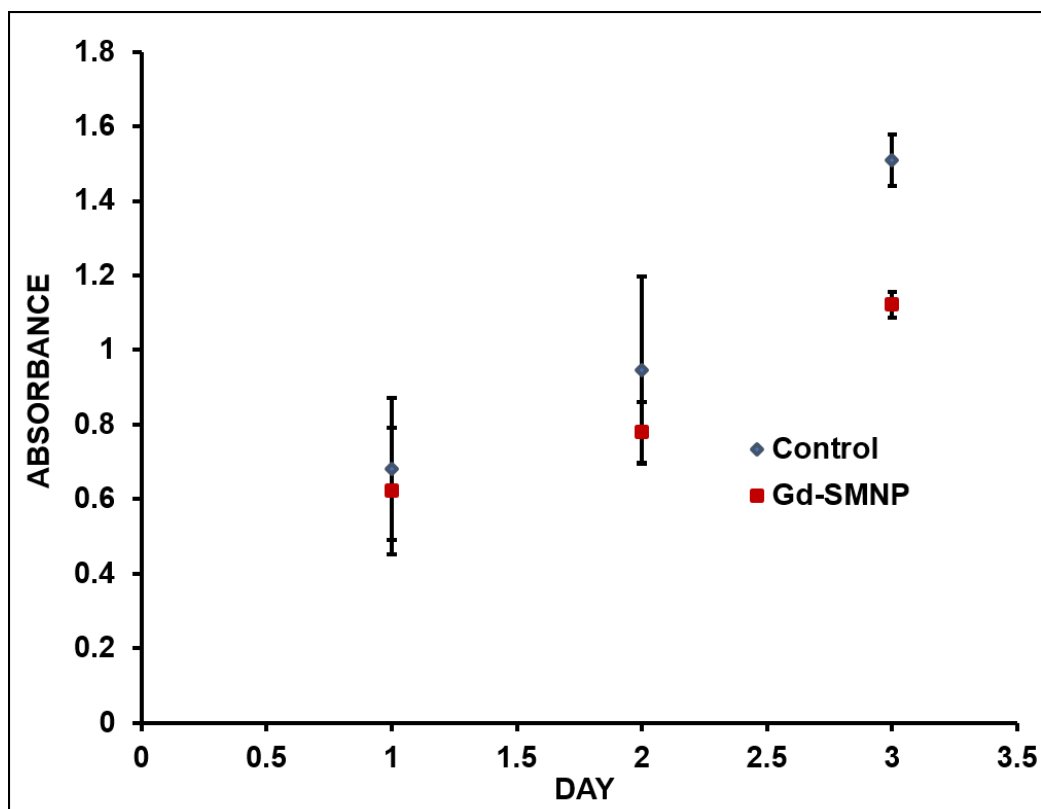


**Figure S11. Viability assay of Gd(III)-SMNP treated hMSCs.** Cells doubled in approximately 3 days for control (untreated hMSCs) and cells labeled with 0.42 mg/mL Gd(III)-SMNP. The error bars represent the standard error (n=8).

## CHAPTER 3: SYNTHESIS OF ULTRASMALL SYNTHETIC MELANIN NANOPARTICLES BY UV IRRADIATION IN ACIDIC AND NEUTRAL CONDITIONS

### 3.1 Introduction

Synthetic melanin nanoparticles (SMNPs) are an important class of bio-based synthesized nanomaterials that have been used as multimodal imaging agents<sup>77, 134</sup>, photo-thermal agents<sup>135-136</sup>, drug-delivery systems for chemotherapy<sup>70</sup>, and in the fabrication of stimuli-responsive films<sup>68</sup>. In humans, melanins play a diverse role in biological functions such as coloration<sup>69</sup>, chelation<sup>137</sup>, photoprotection<sup>138</sup>, thermoregulation<sup>139</sup>, and quenching of free radicals<sup>140</sup>. Melanins are present within the skin, eye, brain, and hair in two forms: pheomelanin and eumelanin<sup>65</sup>. Pheomelanin is a reddish-yellow pigment which produces free radicals under UV irradiation<sup>141</sup>, cell lysis in Ehrlich ascites carcinoma, and histamine release from mast cells<sup>142</sup>. Eumelanin is a brownish-black pigment and is a known photoprotector, antioxidant, and serves as a marker of Parkinson's disease and melanoma<sup>143</sup>. Eumelanin is typically considered a heterogenous macromolecule of 5,6-dihydroxyindole and the 2-carboxylated form, 5,6-dihydroxyindole-2-carboxylic acid. Pheomelanin is a similar heterogenous macromolecule but includes sulfur from cysteinyl-dopa<sup>66</sup>. Melanins are formed in nature through the catalytic oxidation of l-tyrosine with tyrosinase<sup>144</sup>. Interestingly, recent work has focused on using synthetic eumelanins as biocompatible platforms in organic electronics, hybrid materials, and biointerfaces<sup>145</sup>. Similar biological-inspired applications of polydopamine (PDA) structures have shown that thin PDA films can attach to a variety of inorganic and organic materials<sup>146</sup>, be used to improve energy production and storage<sup>147</sup>, be used in photocatalysis via Cd<sup>2+</sup> loaded PDA precursors<sup>148</sup>, and formulated as a PDA-based gel sunscreen<sup>149</sup>. Multifunctional PDA nanoparticles for tumor-targeted phototherapy using dual peptide RGD- and beclin 1-modified particles has been suggested for improved cancer therapy<sup>150</sup>.

The synthesis of SMNPs typically involves the reaction of dopamine hydrochloride in bases such as NaOH or tris base and subsequent auto-oxidation<sup>83, 151-152</sup>. One of the challenges in the fabrication of SMNPs is the synthesis of ultrasmall nanoparticles (UMNP) with diameters of <50 nm in acidic or neutral conditions. This limits the application of SMNPs where an alkaline condition is prohibited<sup>153</sup> or size control is critical for bioaccumulation in target tissues<sup>154</sup>. SMNPs from 25 to 120 nm have been formed by the autoxidation of dopamine in sodium hydroxide<sup>83, 152</sup>, but this approach required alkaline conditions. Microplasma electrochemistry has been used to synthesize fluorescent polydopamine nanoparticles with a size of 3.1 nm using dopamine hydrochloride<sup>155</sup>; however, this method utilized a low pH of 5 and required high energy electrochemistry, which is expensive. Amin et. al synthesized polydopamine-based melanin-mimetic nanoparticles with diameters from 25 - 120 nm using sodium hydroxide base<sup>152</sup>. Ultrasmall melanin nanoparticles with a size of  $4.5 \pm 0.5$  nm have also been synthesized by dissolving pristine melanin granules in 0.1 N NaOH and neutralizing under sonication, but required basic conditions and a top-down approach<sup>41</sup>. Wang et. added varying ratios of edaravone and 2-phenyl-4, 4, 5, 5,-tetramethylimidazoline-1-oxyl 3-oxide (PTIO') to dopamine hydrochloride and added aqueous ammonia to form nanoparticles with size ranging from 155 – 452 nm<sup>156</sup>. Chen et. al synthesized nanoparticles chelated with  $\text{Fe}^{2+}$  and  $\text{Fe}^{3+}$  using sodium hydroxide and polyethylene glycol (PEG)<sup>157</sup>. Ni et. al formed water-soluble chitosan-polydopamine nanoparticles with hydrodynamic diameters of approximately 10 nm using tris base and an electrostatic complexation between chitosan and the polymerized dopamine<sup>158</sup>, requiring the use of a base. Finally, Lie et. al formed fluorescent polydopamine dots from the degradation of polydopamine induced by hydroxyl

radicals by dissolving dopamine hydrochloride in sodium hydroxide, heating, and aging for 2 weeks.<sup>159</sup>

Synthetic SMNPs are routinely formed from dopamine under basic conditions in solution<sup>69, 83, 151, 159-160</sup>. This approach produces particles typically in size ranges from 100 – 500 nm via a base-mediated synthesis. In addition, PDA coatings have been described on a variety of underlying substrates using 3,4-dihydroxy-L-phenylalanine (DOPA)<sup>161</sup>, a precursor of dopamine. Interestingly, UV-initiated polymerization of dopamine hydrochloride was used to form polydopamine coatings in both acidic and basic conditions with rapid synthesis of 2 h and a polymerization rate controllable by varying the UV irradiation time<sup>162</sup>.

Inspired by this UV-initiated polymerization of polydopamine films, we used UV-irradiation to form ultrasmall melanin nanoparticles <50 nm with size control determined by pH. We believe this is the first example of UV-initiated polymerization of dopamine at this pH range. The product is ultrasmall synthetic melanin nanoparticles with exquisite size control and diameters from 9.4-31.4 nm. Additional advantages of this UV-initiated synthesis method include tunable pH conditions, rapid (2 h) synthesis, and controllable kinetics via UV irradiation dose and wavelength.

### **3.2. Methods**

*Reagents.* The following materials were acquired and used as received: dopamine hydrochloride (Sigma-Aldrich), tris base (Sigma-Aldrich), diethylhydroxylamine (DEHA, Sigma-Aldrich), acetone (Sigma-Aldrich), deuterium oxide (D<sub>2</sub>O, Cambridge Isotope Laboratories), Xzero Type 1 reference water (XZero).

*Instrumentation.* TEM imaging used a Jeol microscope operating at 200 kV. Micrographs were recorded on a 2 K X2 KGatan CCD camera. Absorbance measurements used a Molecular Devices SpectraMax M5 spectrometer, and the absorbance was read in 10-nm increments from 200 nm – 1000 nm. Zeta potential was measured using a Zetasizer-90 (Malvern Instruments). pH measurements utilized a Milwaukee MW 102 pH meter and Hydrion pH paper. UV irradiation utilized an 8-Watt, 0.2 Amps, 115 V, 60 Hz 3UV-38 UV lamp (UVP, USA) at 254 nm unless otherwise indicated. Multispectral advanced nanoparticle tracking analysis (MANTA) utilized the MANTA Instruments ViewSizer™ 3000 (USA). The FTIR spectrums were collected using a PerkinElmer spectrometer (USA). The samples were scanned from 1500-600 cm<sup>-1</sup> and the data were analyzed by PerkinElmer software. The molecular structure was studied by <sup>1</sup>H NMR utilizing a 300 MHz Bruker NMR spectrometer. The spectra were processed using the Topspin 3 program.

*Nanoparticle Syntheses.* UMNP was prepared from dopamine hydrochloride in a method inspired by the synthesis of polymerized dopamine films<sup>107</sup>. In a typical reaction, 200 microliters of dopamine hydrochloride aqueous solution was added to a 96-well plate and constantly stirred. The samples were irradiated under UV (254 nm) for 2 h at a constant distance of 3 cm unless otherwise noted. The SMNPs were centrifuged and washed with deionized water 3 times. The photopolymerized fractions were isolated by filtration through a centrifuge filter with 30000 Da molecular weight cutoff.

*TEM Preparation.* Five microliters of each sample were placed on a Ted Pella 300 mesh Cu TEM 0753-F F/C TEM sample grids. The samples were dried in dark conditions for 1 h prior to imaging.

*Size Analysis.* TEM images of at least five fields-of-view of approximately 150 nanoparticles were analyzed using ImageJ software for each synthesis condition. The average size

and polydispersity index (PDI) were analyzed for each sample. For multispectral advanced nanoparticle tracking analysis (MANTA) analysis, solutions were prepared with Xzero Type-1 reference water with 30 videos per trial and automated stirring between each video.

*Zeta Potential.* UMNP and SMNP was diluted in 500 microliters of Millipore water, phosphate buffered saline (PBS) and analyzed with a Zetasizer 90.

*pH Readings.* The pH of solutions was measured by analyzing 10 microliters of solution with pH paper and/or 1 mL of solution with a pH meter.

*Absorbance Readings.* 200 microliters of solution were added to wells in 96-well plates. The absorbance was read from 200 – 1000 nm with a UV-Vis spectrometer and plotted using GraphPad Prism Software.

*NMR Preparation.* Glassware was washed thrice with acetone and D<sub>2</sub>O to remove contaminants. 1 mL of samples (1 mg/mL) was added to 10 mL of D<sub>2</sub>O and analyzed in the NMR.

### **3.3. Results and Discussion**

The polymerization schematic of dopamine to form synthetic melanin nanoparticles in aqueous solutions with and without UV irradiation is shown in **Figure 3.1**. We noted significant changes in the product as a function of the reaction conditions including pH and UV stimulus suggesting that ultrasmall synthetic melanin nanoparticles could be formed as a function of pH and UV irradiation. The amount of absorbance measured at  $\lambda = 280$  nm is proportional to the initial concentration of dopamine (**Supplementary Figure 1**) indicating that this characteristic peak can be used to estimate the amount of dopamine in solution. The continued presence of this

peak at  $\lambda = 280$  nm after UV irradiation is likely due to either non-reacted dopamine or the presence of small aggregates of dopamine- 5,6-dihydroxyindole<sup>8,163</sup>.

From pH 8.0-10.0, dopamine polymerizes to form synthetic melanin nanoparticles with or without UV due to the deprotonation of the amine group<sup>73</sup>. At pH 6.4-7.0, dopamine polymerizes under UV irradiation at wavelength of 254 nm; samples without UV mostly remain as the dopamine monomer. Using DOPA as a precursor, Kim et. al suggested that above a pH of 7.0, a deprotonation of the amine site accelerates the intramolecular cyclization to 5,6-dihydroxyindole-2-carboxylic acid<sup>73</sup>; a similar effect may be occurring to deprotonate the amine in our experiments with dopamine. Oxidizing the catechol to benzoquinone and the intra- and inter-molecular addition of the catechol amines also requires the deprotonation of the amine group<sup>73, 164</sup>. UV irradiation is known to generate reactive oxygen species (ROS), which acts as an accelerant in the oxidation steps<sup>162</sup>.

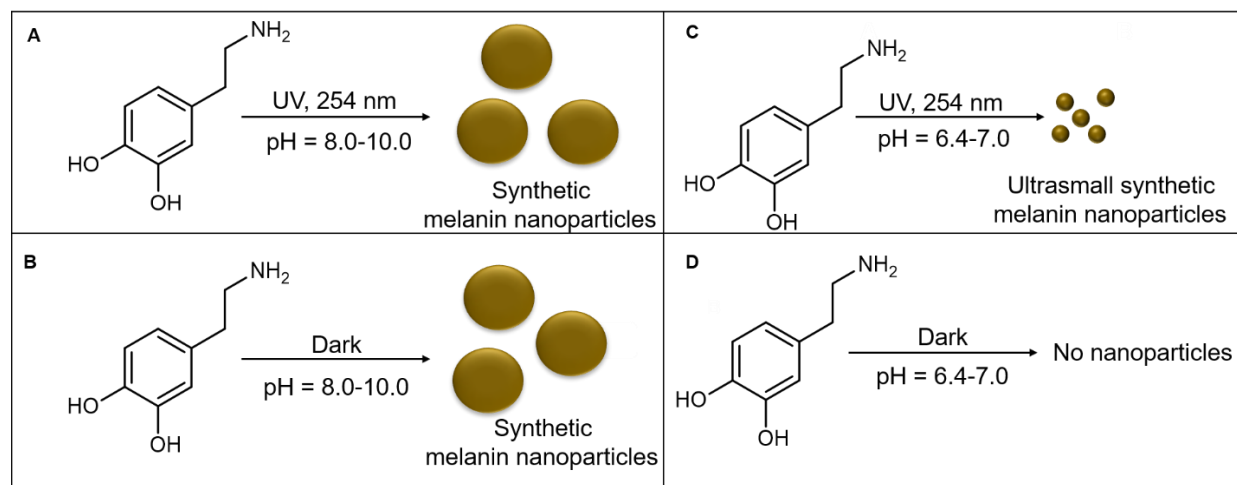


**Figure 3.1 Synthesis and characterization of ultrasmall synthetic melanin nanoparticles.** Ultrasmall synthetic melanin nanoparticles were made by the polymerization of dopamine in aqueous solution with UV irradiation at a wavelength of 254 nm. **A**) Dopamine polymerizes under UV in basic conditions at pH = 8.0-10.0 to form synthetic melanin nanoparticles (SMNPs). **B**) Dopamine polymerizes in the dark in basic conditions at pH = 8.0-10.0 to form synthetic melanin nanoparticles, **C**) Dopamine polymerizes under UV in acidic conditions at pH = 6.4-7.0 to form ultrasmall synthetic melanin nanoparticles (UMNPs). **D**) Dopamine does not polymerize in the dark at pH = 6.4-7.0 conditions.

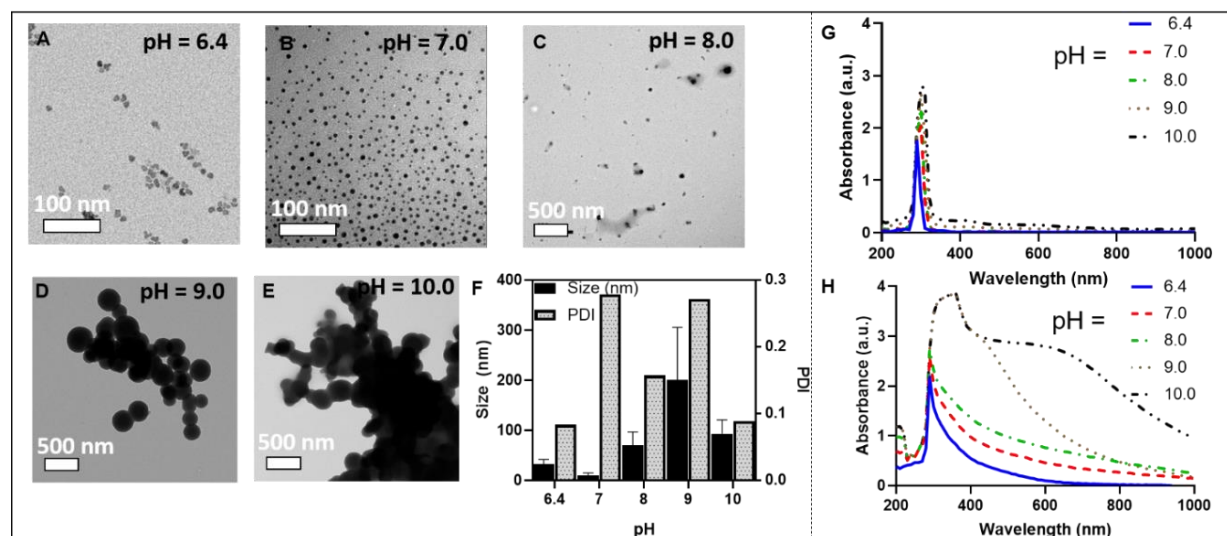


**Figure 3.2. TEM and absorption spectrum of SMNP and UMNP at initial concentration of 1 mg/mL dopamine.** **A)** TEM image of UMNP formed at pH 6.4 with 24 h UV irradiation; the average size is 31.4 nm. The size was confirmed with multispectral advanced nanoparticle tracking analysis (MANTA) analysis<sup>165</sup>, indicating a mode size of 34 nm of all particles measured. **B)** TEM image of UMNP formed at pH 7.0 with 24 h UV irradiation indicated an average size of 9.40 nm. **C)** TEM image of SMNP formed at pH 8.0 with 24 h UV irradiation indicated average size of 69.2 nm. **D)** TEM image of SMNP formed at pH 9.0 with 24 h UV irradiation indicated average size of 200 nm. **E)** TEM image of SMNP formed at pH 10.0 with 24 h UV irradiation indicated average size of 92.8 nm. **F)** Size dependence on pH. The sample with pH 7.0 yielded the smallest spherical UMNP under UV irradiation. **G)** Absorbance spectrum based on pH from 6.4-10.0 prior to UV irradiation shows the characteristic dopamine peak at 280 nm. **H)** Absorbance spectrum based on pH from 6.4-10.0 shows a broadening of the characteristic dopamine peak from 280 nm – 1000 nm indicating polymerization of UMNP and SMNP.

### 3.3.1 Size control.

We synthesized synthetic melanin nanoparticles with controllable size ranges from 9.40 nm – 200 nm by varying the pH of the solution (**Figures 3.2A-3.2E**). The average size of the nanoparticles from pH 6.4 – 10.0 is quantified in **Figure 3.2F**. The difference in size is likely due to the difference in deprotonation of the amine group and oxidation steps under UV irradiation<sup>73</sup>. From pH 6.0 – pH 7.0 with UV irradiation, ROS acts as the accelerant in the oxidation steps<sup>162</sup> to oxidize the catechol to benzoquinone and initialize polymerization. At pH > 7.0, the amine site is deprotonated which accelerates the intramolecular cyclization<sup>73</sup>. Previous studies using a base-



mediated approach in synthesis showed that the size of nanoparticles decreases with an increase in pH when  $\text{pH} > 8.0$ <sup>166-167</sup>, consistent with our findings that the size decreases from pH 9.0 – pH 10.0. Oxidizing the catechol to benzoquinone and the intra- and inter-molecular addition of the catechol amines also requires the deprotonation of the amine group<sup>73,164</sup>. Size control is important for biodistribution of injected particles for vascular targeting, and the enhanced permeability and retention effect (EPR) has can facilitate nanoparticle accumulation with diameters less than 500 nm in tumors<sup>168</sup>. Nanoparticles with diameters  $< 20$  nm have been shown to cross tight endothelial junctions, and gold nanoparticles with a diameter of 10 nm were shown to have the widest biodistribution to the blood, liver, spleen, kidney, testis, thymus, heart, lung and brain compared to larger particles when injected intravenously in rats<sup>154,168</sup>. Dopamine was the only peak observed in the absorbance spectrum in all samples prior to UV irradiation (**Figure 3.2G**) with a characteristic peak at 280 nm<sup>169</sup>. After UV irradiation (254 nm), the absorbance spectrum broadened amongst all samples from a peak at  $\lambda = 280$  nm to an increase in absorbance 400 nm – 1000 nm. This change in absorbance spectrum is a characteristic indication of the formation of melanins<sup>143,170</sup> as the broad absorption band in conjugated systems is caused by the oxidative-polymerization of dihydroxyindole (DHI) and dihydroxyindole-2-carboxylic acid (DHICA)<sup>73</sup>. The careful correlation between TEM and absorption spectroscopy shown here suggested that the width of the absorbance peak directly reports on the extent of dopamine polymerization and thus, subsequent studies primarily utilized absorbance data rather than TEM.

### **3.3.2 Reaction Time.**

The polymerization reaction is also dependent on time; dopamine (5 mg/mL) polymerized after 2 h of UV irradiation (**Supplementary Figure S2A**), and polymerization increased as UV irradiation time increased. Liu et. al showed synthetic melanin nanoparticle synthesis with a 70

nm size and a 24 h reaction time<sup>171</sup>. Cho and Kim formed synthetic melanin nanoparticles with size range of 80–490 nm using a 3 h reaction time with a hydroxide-ion mediated synthesis<sup>172</sup>. Dopamine (5 mg/mL) in dark conditions at a pH of 6.4 (**Supplementary Figure S2B**) does not polymerize even after 8 h, indicating that UV irradiation is necessary under pH conditions of 6.4 to deprotonate the amine and accelerate the intramolecular cyclization to 5,6-dihydroxyindole-2-carboxylic acid<sup>73</sup>.

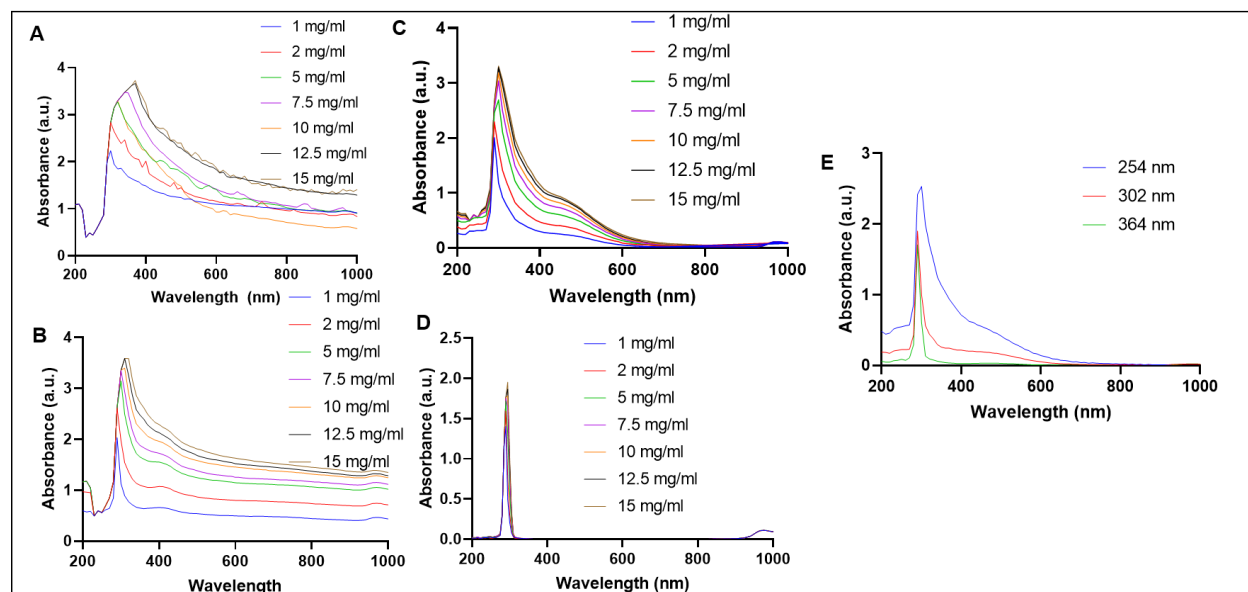


**Figure 3.3. Characterization of SMNP and UMNP formed in water with UV irradiation at varying concentrations.** **A)** Basic dopamine solutions with pH = 10.0 displayed polymerization with UV irradiation (254 nm) for 24 h and showed a broad peak shift from 290 – 400 nm at initial concentrations of dopamine of 1 – 15 mg/ml. **B)** Dopamine solutions with pH = 10 showed polymerization in the dark after 24 h. **C)** Acidic dopamine solutions with pH = 6.4 with initial dopamine concentrations from 1 mg/ml – 15 mg/ml were irradiated with UV light (254 nm) for 24 hours to form UMNP. Absorbance increased as concentration of dopamine increased with a red shift in the absorbance spectrum. **D)** Acidic dopamine solutions with pH = 6.4 in dark conditions for 24 h showed a characteristic dopamine peak at 280 nm and did not show polymerization. **E)** UV wavelength of 254 nm irradiated for 24 h causes higher polymerization in dopamine than samples irradiated at 302 nm and 364 nm for 24 h. Polymerization does not occur when samples are irradiated at 364 nm for 24 h.

SMNP formed at pH = 10.0 with UV irradiation for 24 h showed increased polymerization (**Figure 3.3A**) versus SMNP formed in basic conditions of pH = 10.0 in the dark for 24 h (**Figure 3.3B**). This was indicated by the broadening of the absorbance peak from 280 nm to 400 nm

(**Figure 3.3C**). Dopamine solution with pH = 6.4 in dark conditions for 24 h did not show a change in the characteristic absorbance peak of 280 nm indicating no polymerization and no nanoparticles observed (**Figure 3.3D**). UV-irradiated samples of dopamine (5 mg/mL) in pH = 6.4 and samples of dopamine (5 mg/mL) in pH = 9.0 in dark conditions show a linear, first-order reaction over 2 h (**Supplementary Figure S3**). This is consistent with the findings of Herlinger et. al who proposed first-order reaction in the autooxidation of dopamine where he found the reaction to be first-order in [dopamine].<sup>173</sup> Additionally, the reaction rate increased 4.3 times with UV irradiation versus the dark (**Supplementary Figure S4**) showing that UV irradiation is necessary to accelerate the reaction. The change in polymerization rate for 0.1 mg/mL – 1 mg/mL initial concentration of dopamine in water is shown in **Supplementary Figure S5**; polymerization was observable at 0.2 mg/mL.

#### 3.3.4 Wavelength Effects

The wavelength of UV irradiation was varied from 254 nm – 365 nm and solutions at 254 nm showed the highest amount of polymerization due to higher energy at shorter wavelengths (**Figure 3.3E**). At a wavelength of 254 nm, the energy is approximately  $7.83 \times 10^{-19} J = 4.89 \text{ eV}$  and the energy is approximately  $366 \text{ nm} = 5.43 \times 10^{-19} J = 3.39 \text{ eV}$  at a wavelength of 365 nm<sup>174</sup>. It is likely that the higher energy at 254 nm is required to deprotonate the amine and initiate the further oxidation steps.

#### 3.3.4 FTIR Characterization

Changing the pH from 6.4 – 10.0 did not greatly affect the FTIR spectra suggesting that the core composition did not change significantly (**Supplementary Figure S6**).

### 3.3.4 NMR Characterization

The molecular structure of the UMNP formed during the reaction was studied by  $^1\text{H}$  NMR spectrum. For this experiment, dopamine monomer and SMNP prepared by base-catalyzed polymerization were used as positive and negative controls. Dopamine hydrochloride dissolved in  $\text{D}_2\text{O}$  yielded two triplets at 2.77 and 3.13  $\delta$  (**Fig 3.4A**) corresponding to the aliphatic side chains. The aromatic protons on dopamine hydrochloride appeared as closely grouped peaks between 6.3.-6.83  $\delta$ . The SMNP showed no interpretable  $^1\text{H}$  NMR signals owing to low solubility. The UMNP showed three peaks between 4.00-3.00  $\delta$  (**Fig 3.4B**). These peaks included two multiplets with intensity ratios of 1:1 and a low broad multiplet. The absence of any aromatic proton signals in the photopolymerized fraction showed that polymerization has occurred due to UV exposure. The relatively narrow appearance of the NMR peaks in the photopolymerized fractions point to the low molecular weight of the chains. The zeta potential of the SMNP was  $-18.8$  mV in water and  $-19.1$  mV in PBS. The zeta potential of the UMNP was  $-8.49$  mV in water and  $-5.50$  in PBS. The less negative surface charge of the UMNP may be due to less deprotonation of the amine group compared to the SMNP. A previous report found the zeta potential from pH 2.5–9.0 ranged from approximately  $+20$  mV to  $-40$  mV based on pH with an isoelectric point at pH 4.0-4.1<sup>152</sup>. Zeta potentials from synthetic melanin nanoparticles formed with varying ratios of edaravone, a radical scavenger, and PTIO $\cdot$ , stable free radicals, ranged from  $-39.8$  to  $-24.0$  mV at a pH of 9.55<sup>156</sup>. Additionally, a previous report of water-soluble chitosan-polydopamine nanoparticles measured the zeta-potential to be  $48$  mV.<sup>158</sup>

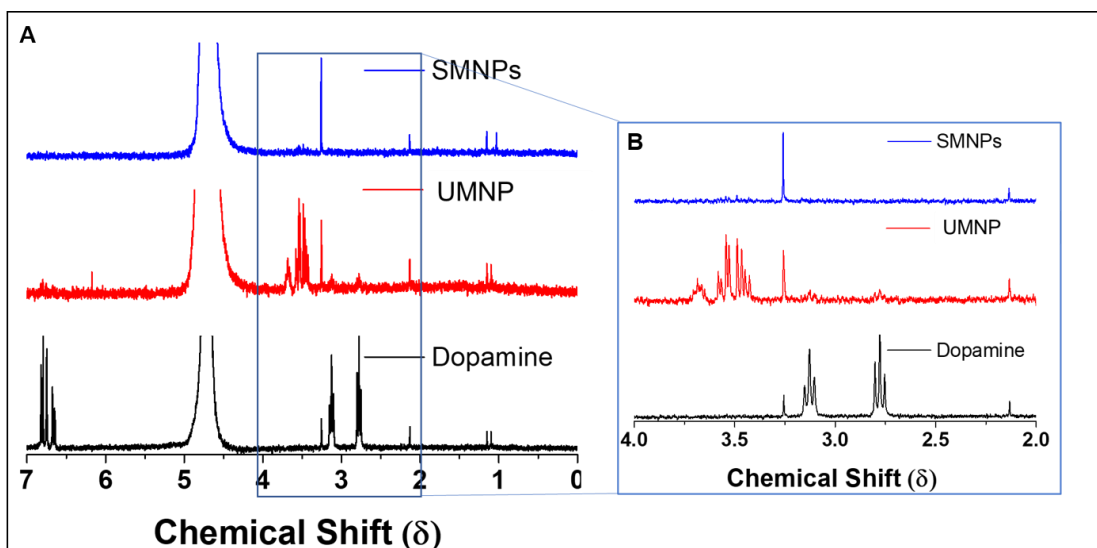


**Figure 3.4** NMR spectroscopy shows loss of aliphatic side chains in UMNP indicating that polymerization has occurred. **A)** Stacked NMR spectrum of SMNPS, UMNP, and dopamine. **B)** Dopamine hydrochloride dissolved in D<sub>2</sub>O yielded two triplets at 2.77 and 3.13  $\delta$  corresponding to the aliphatic side chains.

### 3.3.5 Mechanism

Despite the prevalence of melanin nanoparticle synthesis, the exact formation mechanism remains unclear. *Ab initio* calculations have suggested that planar oligomers are stacked together via  $\pi$ - $\pi$  interactions in synthetic melanin synthesis<sup>175</sup>. Hong et. al. suggested that the dopamine and 5,6-dihydroxyindole self-assemble forming a physical trimer structure<sup>163</sup>. Zhang et. al showed that singlet oxygen ( $^1\text{O}_2$ ), superoxide ( $\text{O}_2^-$ ), peroxide ( $\text{O}_2^{2-}$ ), as well as hydroxyl radicals ( $\cdot\text{OH}$ ) are essential to the polymerization of dopamine<sup>176</sup>. Reactive oxygen species including hydroxyl radicals, superoxide radicals, and singlet oxygen are generated under UV irradiation and have increased chemical activity over molecular oxygen. Previous studies showed that ROS can initiate the polymerization of dopamine, and UV irradiation initiates the formation of ROS<sup>162</sup>.

Our data validates the proposed mechanism for dopamine polymerization via UV irradiation suggested by Du et. al<sup>162</sup> (**Figure 3.5A**). Dopamine is oxidized to dopamine quinone followed by an intramolecular Michael addition and deprotonation leading to leuco-dopamine chrome<sup>162, 177</sup>. Additional

oxidation and rearrangement leads to the formation of indole-quinone which then rearranges to form 5,6-dihydroxyindole<sup>143, 162</sup>. Dopamine quinone, leuco-dopamine chrome, and 5,6-dihydroxyindole then copolymerize; this polymerization is similar to the natural synthesis of eumelanin. In nature, eumelanin is synthesized from the orthohydroxylation of tyrosine and catalyzed by tyrosine oxidase to yield L-DOPA<sup>143</sup>. With an oxidant such as oxygen or metal cations, an oxidation yields dopaquinone; a Michael addition followed by oxidation yields 5,6-dihydroxyindole or 5,6-dihydroxyindole-2-carboxylic acid, foundations of eumelanins<sup>143</sup>. In our experiments, degassing the atmosphere with nitrogen showed reduced UV-vis absorption and less color change suggesting the formation of fewer nanoparticles. A lack of oxygen slows the kinetics of polymerization underscores the need for oxygen (**Figure 3.5B, inset**).

To further elucidate the role that oxygen plays in the polymerization of dopamine, the diethylhydroxylamine (DEHA) oxygen scavenger was added to the dopamine solution to prevent ROS generation while under UV irradiation (**Figure 3.5C**). The polymerization of the UV-irradiated samples was decreased when DEHA was added. Basic conditions were used with the addition of Tris base because DEHA is basic in water. The reduction in polymerization as measured by absorbance suggests that the dopamine polymerization is triggered by ROS generated by UV irradiation.

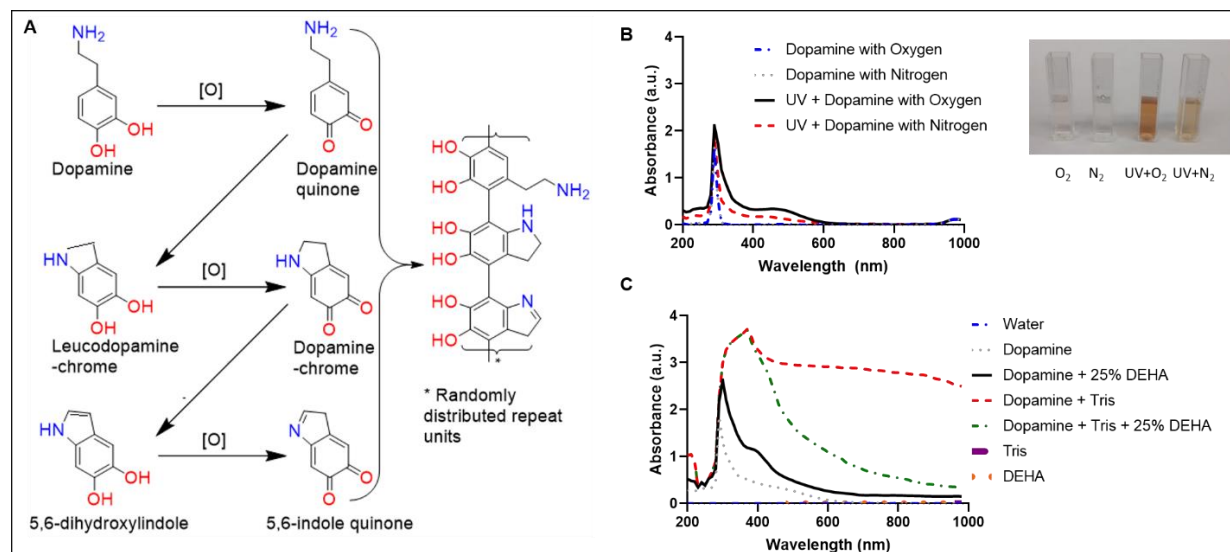


**Figure 3.5 Mechanism of UV-initiated polymerization.** **A)** Adapted from Du. et al.<sup>162</sup>. Under the presence of oxygen, dopamine forms dopamine quinone, dopamine-chrome, and 5,6-indole quinone. **B)** Dopamine under typical atmosphere (inset, O<sub>2</sub>) and nitrogen degassed atmosphere (inset, N<sub>2</sub>) without UV irradiation display a characteristic peak at 280 nm with no polymerization after 24 h. Dopamine irradiated with UV under an oxygenated atmosphere displays polymerization by turning to the characteristic dark brown color (inset, UV + O<sub>2</sub>). Dopamine irradiated with UV under a nitrous atmosphere displays little polymerization (inset, UV + N<sub>2</sub>). **C)** Dopamine under basic conditions (Tris base) shows increased polymerization as indicated by a broad absorption from 280 nm – 1000 nm when compared to dopamine with tris base and 25% DEHA (oxygen scavenger) indicating that oxygen plays a critical role in the polymerization mechanism.

### 3.4. Conclusion

This study details a synthetic melanin-based contrast agent synthesized under UV irradiation. The most important finding is that the synthetic melanin particles could be synthesized under acidic and neutral conditions to form ultrasmall particles via UV irradiation. UV irradiation produces ROS that initiate the polymerization. Size control of the nanoparticles was possible from 9.40 nm – 200 nm by varying the pH during synthesis.

### 3.5 Author Contributions

The manuscript was written through contributions of all authors. All authors have given approval to the final version of the manuscript.

### **3.6 Acknowledgements**

J.E.L. acknowledges funding from the National Institutes of Health (NIH) Institutional National Research Service Award T32 CA153915, Cancer Researchers in Nanotechnology (Zhang). J.V.J. acknowledges funding from the NIH (Grants R00 HL117048 and DP2 HL137187) and infrastructure from Grants S10 OD021821 and S10 OD023555. The electron micrographs were taken in the Cellular and Molecular Medicine Electron microscopy core facility which is supported in part by National Institutes of Health Award number S10 OD023527. This work was performed, in part, at the San Diego Nanotechnology Infrastructure of UCSD, a member of the National Nanotechnology Coordinated Infrastructure, which is supported by the National Science Foundation (Grant ECCS-1542148).

Chapter 3, in full, is a reprint of the material as it appears in ACS Applied Bio Materials, 2019, Lemaster, Jeanne E., AnanthaKrishnan Soundaram Jeevarathinam, Ajay Kumar, Bhargavi Chandrasekar, Fang Chen, and Jesse V. Jokerst. The dissertation author was the primary investigator and author of this paper.



### 3.7 Appendix

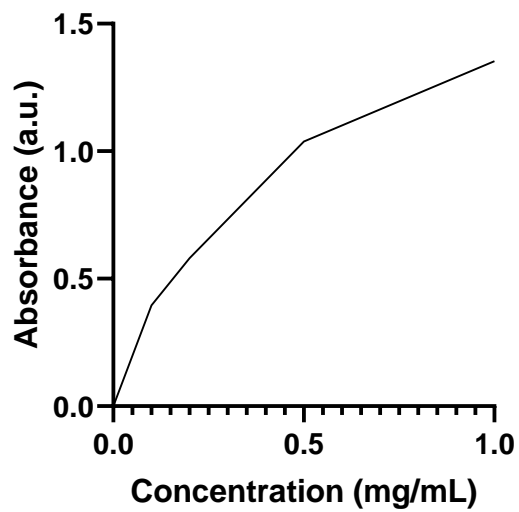


**Figure S1. Absorbance vs. Concentration of Dopamine.** The amount of dopamine in the initial solution correlates with the absorbance at 280 nm.

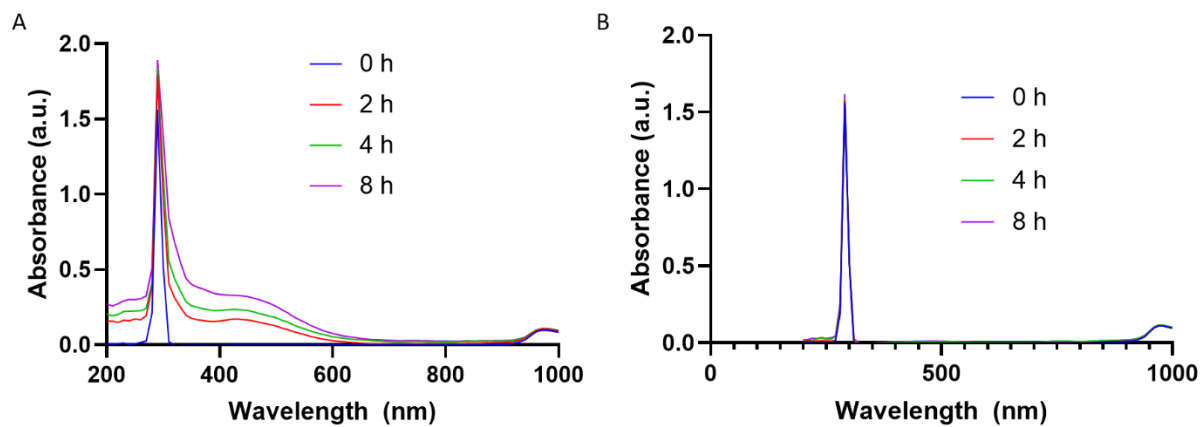


**Figure S2. Effect of UV irradiation time on polymerization.** **A)** UV-irradiated samples of dopamine (5 mg/mL) in pH = 6.4 for 0 – 8 h display polymerization as indicated by a broadening of the absorbance at 290 nm. **B)** Dopamine (5 mg/mL) in pH = 6.4 for 0 – 8 h displays no polymerization with no change in absorbance spectrum.

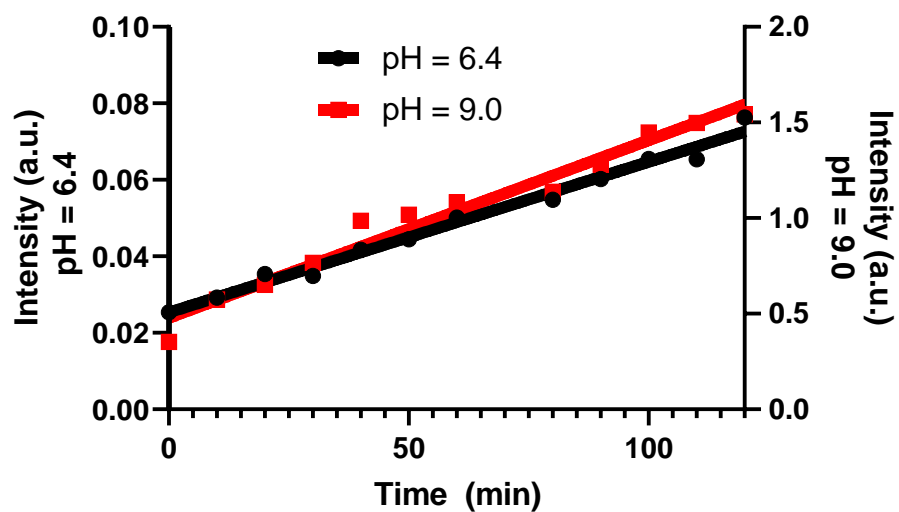


**Figure S3. Reaction kinetics of SMNP and UMNP.** UV-irradiated samples of dopamine (5 mg/mL) in pH = 6.4 as well as samples of dopamine (5 mg/mL) in pH = 9.0 in dark conditions show a linear, first-order reaction over 2 h with  $R^2$  values = 0.98 and 0.96 respectively.

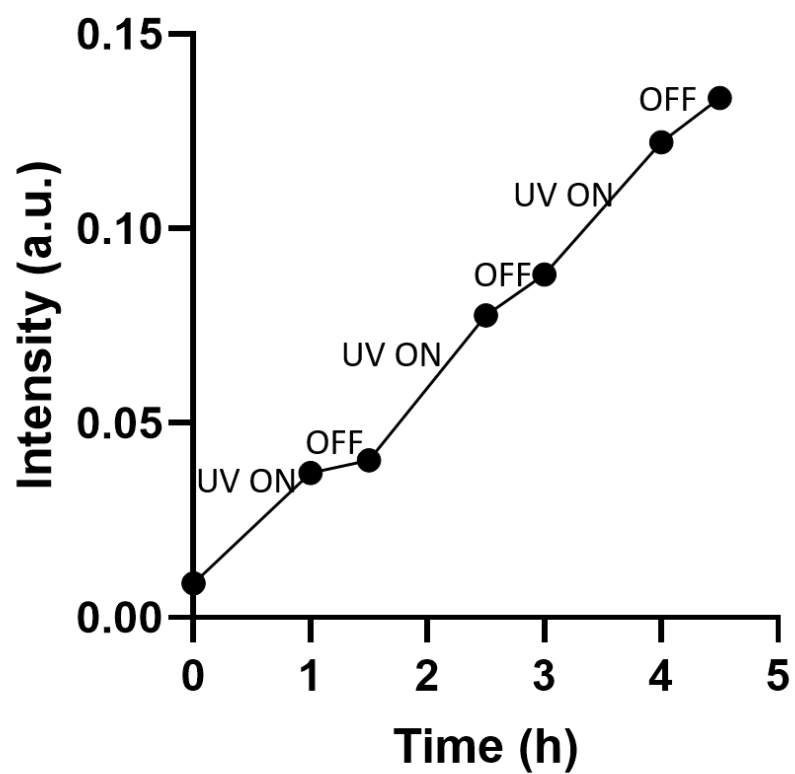


**Figure S4. Controllable on/off reaction using UV irradiation.** Dopamine (5 mg/mL) in pH = 6.4 was irradiated with UV for 1 h and the samples were placed in dark conditions for 30 min. The samples with UV irradiation showed a 4.3-fold increase in reaction rate after 1 h of UV irradiation as opposed to the samples in dark conditions.

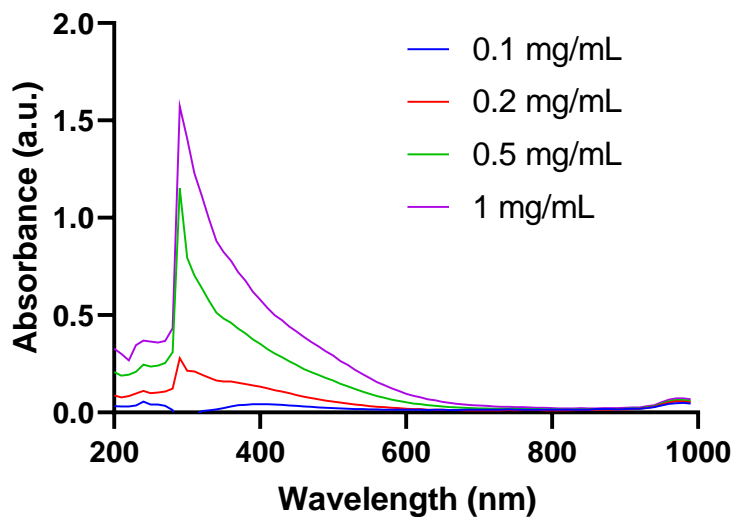


**Figure S5. Low concentration of dopamine and polymerization.** The effect of polymerization on absorbance from 0.1 – 1 mg/mL initial concentration of dopamine in water.

## CHAPTER 4: THE DEVELOPMENT OF A TRIMODAL CONTRAST AGENT FOR ACOUSTIC AND MAGNETIC PARTICLE IMAGING OF STEM CELLS

### 4.1 Introduction

Stem cells have regenerative potential to remodel bone, cartilage, and cardiac tissue. Recent studies using nanolayered hybrids of ligand and ligand activators<sup>178</sup> as well as bioadhesive supramolecular gelatin hydrogels<sup>179</sup> have been used to facilitate stem cell regeneration of bone tissue. Self-assembled N-cadherin mimetic peptide hydrogels have also been shown to regenerate cartilage through canonical Wnt/ $\beta$ -catenin signaling<sup>180</sup>. Studies of ligand oscillation integrin used an oscillating magnetic field to characterize the adhesion as well as differentiation of stem cells<sup>181</sup>. After myocardial infarction, stem cell therapy can increase regeneration of cardiac tissue<sup>182-186</sup> and has been used in multiple clinical trials<sup>187-188</sup> for thousands of patients. A meta-analysis of these trials has shown a modest improvement in cardiac function, but the mechanism of this improvement remains somewhat unclear with both differentiation and paracrine effects implicated<sup>189-190</sup>. One challenge to the efficacy of stem cell therapy is poor viability of transplanted stem cells<sup>191-194</sup>, which adversely affects tissue regeneration<sup>195</sup>. Additional challenges include cell contamination, cell mis-delivery<sup>182</sup>, and the interaction of cells with their host environment<sup>196</sup>.

Imaging can help improve stem cell therapy and ensure proper cell delivery while also monitoring the location, number, and fate of delivered cells<sup>197</sup>. For cardiac stem cell trafficking, imaging can help determine the best route for cell delivery as well as the biodistribution of delivered stem cells<sup>198</sup>. Stem cell imaging typically involves labeling a cell with a reporter gene<sup>191</sup>,<sup>195</sup> or an exogenous contrast agent<sup>199</sup>. Various types of imaging have been used for tracking stem cells—with pros and cons for each. Magnetic resonance imaging (MRI) is the gold standard because of the established use of iron oxide nanoparticles, ferric nanoparticles, and gadolinium

chelates<sup>200-201</sup>, and has shown detection of single cells<sup>202</sup>. Recently, a 2-dimensional graphene oxide-based nanomaterial was used as a T1 contrast agent in MRI to label stem cells<sup>203</sup>. However, MRI suffers from low contrast, low specificity, long scan times, and T2 saturation<sup>204</sup>. Positron emission tomography has also been used with reporter genes to track stem cells *in vivo*<sup>205-206</sup> or with exogenous radiolabeled nanoparticles<sup>207</sup>. While positron emission tomography offers high resolution, sensitivity, and quantification<sup>208</sup>, it suffers from high cost<sup>209</sup> and poor spatial resolution.

More recently, we and others<sup>103, 210-211</sup> have shown that ultrasound-based imaging has utility in imaging stem cells. The advantages of ultrasound include up to 300 Hz temporal resolution and good penetration through tissue. In addition, the established use of echocardiography in clinics makes ultrasound a natural fit for cardiac-based stem cell therapy. Mesoporous silica has been used as to image stem cells with ultrasound<sup>211</sup>. However, ultrasound is limited by the lack of contrast of stem cells above background tissue. Photoacoustic imaging can further increase contrast<sup>57, 212-218</sup> and has recently been used in imaging protein sulfenic acids<sup>219</sup>, multimodal imaging of tumors<sup>220</sup>, and biological imaging in the second near-infrared window<sup>221</sup>, but photoacoustic imaging alone has limitations in deep tissue imaging. Contrast agents used to image stem cells for photoacoustic imaging include Prussian Blue–poly(L-lysine) Nanocomplexes<sup>100</sup> as well as DiR<sup>222</sup>. While photoacoustics offers enhanced contrast over ultrasound, penetration depth is limited. One recent solution to low contrast and poor penetration depth in molecular imaging is magnetic particle imaging (MPI).

MPI applies a magnetic gradient field with a central field-free point to the imaging field of view; this field saturates the nonlinear magnetization of magnetic particles<sup>223</sup>. Electromagnets scan the field free point to form an image and MPI signal is generated when the field-free point passes an area with magnetic particles<sup>224</sup>. The magnetization of the magnetic particles changes in

orientation and magnitude which is detected via a coil and the resultant voltage is used to reconstruct the MPI image. MPI most often utilizes Resovist<sup>®</sup> superparamagnetic iron oxide<sup>225</sup>, which is cleared via the hepatobiliary system and approved for clinical use<sup>226</sup>. MPI has been used to track stem cells *in vivo*<sup>224</sup> and image the cardiovascular system<sup>227</sup>. Additionally, MPI shows a linear response to iron oxide dose, unlike T2 magnetic resonance imaging which saturates at high concentrations. Recently, MPI has been used combined with magnetic fluid hyperthermia, showing potential therapeutic coupling capability of MPI with other superparametric iron oxide-based modalities<sup>228</sup>, especially for deep tissue imaging. Additionally, MPI has been used to image labeled mesenchymal stem cells and neural stem cells in the mouse brain to detect approximately 50,000 implanted cells<sup>229</sup>. However, MPI suffers from low temporal resolution and offers no details on the surrounding anatomy.

To overcome the limitations of each of these modalities alone, a multimodal approach combines the advantages of each modality by combining the multifunctionality of nanoparticles<sup>230</sup> and advances in biomedical imaging. For example, combining MRI with a photoacoustic/surface-enhanced Raman scattering contrast agent was used to define brain tumor margins and guide resection<sup>49</sup>. Additionally, tri-modal imaging probes using PET, optical microscopy, and radiometal chelates have been created by combining <sup>64</sup>Cu-DOTA and <sup>111</sup>In-DOTA, with dual MRI/optical probes<sup>231</sup>. Sulfonate-based saline inorganic-organic hybrid nanoparticles have been developed as a multimodal contrast agent for optical, photoacoustic, and magnetic resonance imaging and showed improved T1 values over Gd-based particles<sup>230</sup>. Here, we report a combination approach that uses high frame rate of acoustic imaging with the good contrast and penetration depth of MPI. We report a hybrid nanobubble with ultrasound, photoacoustic, and MPI signal. Because the success of stem cell injections has previously been hindered by inaccurate



injections<sup>232</sup>, we utilized acoustic modalities for real-time guided injections and MPI for long-term, high-resolution imaging. This PLGA-based nanobubble formulation contains iron oxide nanoparticles with a core size of 4.2 nm and mean hydrodynamic diameter of 62 nm to generate MPI signal and a 1,1'-dioctadecyl-3,3,3',3'-tetramethylindotricarbocyanine iodide (DiR)<sup>233</sup> fluorophore to enhance the photoacoustic signal<sup>234</sup>. The bubble conformation increases the ultrasound signal<sup>235</sup>. We studied the effect of the nanobubbles on viability, differentiation, cytokine expression, and migration ability of human mesenchymal stem cells (hMSCs). We then used them to label hMSCs and injected these labeled cells intracardially into living mice. This multimodal contrast agent tracks cells and can also be used in other imaging applications that require good contrast, temporal resolution, and high penetration depth.

## 4.2 Materials and Methods

**Reagents.** The following materials were acquired and used as received: Vivotrax iron oxide nanoparticle solution (5.5 mg/mL, Magnetic Insight, Inc); poly(lactic-co-glycolic acid) (PLGA, Sigma Aldrich); poly vinyl alcohol (PVA, MD Biochemicals); chloroform (Fisher Chemical); DiR (Invitrogen); phosphate buffered saline (PBS, Thermo Fisher); matrigel (Corning); 5% silver nitrate (American Mastertech Scientific, Inc.), 5% sodium thiosulfate (American Mastertech Scientific, Inc.), and Oil Red O (Sigma Aldrich).

**Instrumentation.** Dynamic Light Scattering (DLS) measured the size and zeta potential (Zetasizer-90, Malvern Instruments) of the nanobubbles in water. Transmission electron microscopy (TEM) was performed with the JEOL JEM-1200 EXII operating at 120 kV. We performed photoacoustic and ultrasound imaging with the Vevo 2100 instrument (Visualsonics) with a 21 MHz-centered transducer as described previously<sup>58</sup>. The distance between the imaging transducer and phantom was maintained throughout the scans. We collected at least eight fields

of views (FOVs) for each sample. MPI was performed using the Magnetic Insight MOMENTUM imager<sup>236</sup>. MPI utilized 6T/m gradients with a 45 kHz receiver bandwidth, 20mT peak amplitude, and X-space reconstruction. All absorbance measurements utilized a SpectraMax M5 spectrophotometer from Molecular Devices. Inductively coupled plasma optical emission spectrometer (ICP-OES, Optima 3000DV, Perkin Elmer) was used to determine the number of nanobubbles endocytosed by the cells.

**PLGA Nanobubble Synthesis.** PLGA/Iron oxide/DiR nanobubbles were fabricated via an approach modified from literature<sup>237</sup>. An iron oxide nanoparticle solution (5.5 mg/mL) was added to 1 mL of chloroform. Then, 100  $\mu$ L of DiR (10 mg/mL in DMSO) was added to the solution and vortexed for 10 seconds (Fisher Scientific, Fixed Speed Vortexer). Next, 30 mg of PLGA was dissolved into this solution, and 200  $\mu$ L of Millipore water was added into the solution and sonicated (Branson Sonifier 450) for 1 minute in an ice bath forming a water-in-oil emulsion. Six mL of Millipore water with 2% PVA was added to initiate a secondary emulsion. The solution was sonicated for five minutes and stirred for 24 hours to evaporate the chloroform unless otherwise noted. The iron oxide and DiR-containing nanobubbles were centrifuged (Fisher Scientific Legend XR1) at 22,000 x g for 25 minutes. The nanobubbles were then washed three times with Millipore water to remove excess PVA, iron oxide, and DiR and diluted in Millipore water.

**Cell Culture.** Poietics human mesenchymal stem cells (Lonza, PT-2501) were grown in supplemented media (Lonza, PT-3001) and seeded in a T75 flask at a concentration of 5,000 cells/cm<sup>2</sup>. These cells were labeled with nanobubbles and incubated under standard conditions for 6 hours unless otherwise noted. The hMSCs were washed with PBS to remove free nanobubbles 3 times and detached using TrypLE Express (Life Technologies). Cell viability was determined

using the Cell Viability Kit MTT 3-(4,5-dimethylthiazol-2-yl)-2,5-diphenyltetrazolium bromide (MTT) assay (Biotium). Ten  $\mu\text{L}$  of the MTT solution was added to 100  $\mu\text{L}$  of medium in each well, mixed briefly, and incubated at 37°C for 4 hours; 200  $\mu\text{L}$  of DMSO was added to each well and pipetted to dissolve the resulting formazan salt. The absorbance was read at 570 nm on a spectrophotometer. The MTT assays were conducted by plating 8,000 cells/well in replicate (n=8) in 96 well plates and treated at varying timepoints (0-24 hrs) at a constant concentration (240  $\mu\text{g}/\text{mL}$ ) as well as at varying concentrations (0-480  $\mu\text{g}/\text{mL}$ ) at a constant time (8 hours unless otherwise noted). Wells were analyzed in replicate (n=8). For differentiation studies, adipogenic cells were stained with Oil Red O and osteogenic-differentiated cells were stained with a Von Kossa stain as described previously<sup>238</sup>.

***In vitro* phantom preparation, US imaging, PA imaging, and MPI Imaging.** For US imaging and PA imaging of cells, PLGA nanobubbles or cells (100,000 unless otherwise noted) labeled with nanobubbles were immobilized in a 1% agarose phantom gel. Nanobubble or cell solutions were sonicated and mixed with the 1% agarose solution at a 1:1 ratio. 100  $\mu\text{L}$  of the mixture was pipetted into the phantom gel. 1% agarose solution was used to cover the samples after solidification.

For PA imaging of nanobubbles, PLGA nanobubbles were loaded into polyethylene tubes, sealed, and placed in a 3D-printed phantom holder to maintain constant height of 1 cm between the transducer and the phantom<sup>239</sup>. The gain was set to 30-40 dB and read at a wavelength of 730 nm. Eight fields of views were collected for each sample. For MPI imaging, PLGA nanobubbles or cells (100,000) labeled with nanobubbles were loaded into polyethylene tubes, sealed, and fixed in a sample holder.

**Data analysis.** ImageJ 1.48v 58 was used to quantitate the B-mode signal, PA signal, and MPI signal for nanobubbles via the region of interest (ROI) analysis in arbitrary units for 8-bit images<sup>108</sup>. The US, PA, and MPI means and standard error were calculated from eight field of views in each sample. Error bars represent the standard error of measurements unless otherwise noted. ImageJ was also used to quantitate osteogenic and adipogenic differentiation via ROI for induced and non-induced cells.

**Cytokine Expression.** We plated cells with and without nanobubbles at 200,000 cells per well in a 6-well plate and cultured for 24 hours. We removed the media from the positive and control cells and compared it to the control cells. The protein analysis was performed by MyriadRBM Inc. (Austin, TX).

**Flow Cytometry.** For flow cytometry studies, labeled and unlabeled hMSCs ( $400 \times 10^3$  cells, respectively) were resuspended in PBS; 1  $\mu$ L of monoclonal antibody specific for mesenchymal stem cells (CD73-PE/CD90-FITC/CD105-APC) was added to the cells. Flow cytometry analysis was run by FACSCalibur (BD Biosciences, San Jose, CA, USA) and FlowJo software was used to analyze the results (Becton Dickinson and Company).

***In vivo* Animal Studies.** Adult nu/nu mice (12 weeks old) were used for this study. Animal studies were conducted in accordance with our institution's IACUC animal use committee. Mice were anesthetized with 2% isoflurane in oxygen at 2 L/min that was confirmed with a tail pinch. The labeled cell pellets were re-suspended in 50  $\mu$ L of PBS and mixed in a 1:1 ratio with matrigel. They were loaded into a 24-gauge syringe and then injected using B-mode ultrasound for injection guidance. For MPI imaging, mice were anesthetized, sacrificed, and injected intramyocardially with nanobubble-labeled hMSCs. Mice were then frozen and sent to Magnetic Insight, Inc.

(Alameda, CA) to conduct MPI. For animal studies, Matlab was used to colormap the signal from MPI. Images were overlaid on stock CT images of adult mice.

### 4.3 Results and Discussion

**Figure 4.1A** presents a schematic of this work—a PLGA-based nanobubble with DiR and iron oxide was used as a MPI/PA/US contrast agent to image stem cells in mice. Nanobubbles were synthesized with DiR and iron oxide, used to label hMSCs, injected intramyocardially into mice, and imaged. DiR was used to enhance the PA signal of the particle, and iron oxide provided the MPI contrast. Our results showed that the PLGA-nanobubble increased the US signal 3.8-fold *in vivo*, building off of previous studies<sup>240</sup>.

#### 4.3.1 Synthesis and Physical Characterization

Transmission Electron Microscopy (TEM) imaging showed that the nanobubbles (NBs) were spherical in shape and uniform in size of approximately 185 nm. **Figure 4.1B** shows TEM imaging of the PLGA nanobubbles without iron oxide. **Figures 4.1C** and **4.1D** show TEM imaging of the nanobubbles with iron oxide; the black particles are the iron oxide nanoparticles. TEM imaging showed that the iron oxide particles were present in approximately 70% of the PLGA nanobubbles (**Figure 4.1C** and **Supporting Information Table S.1**).

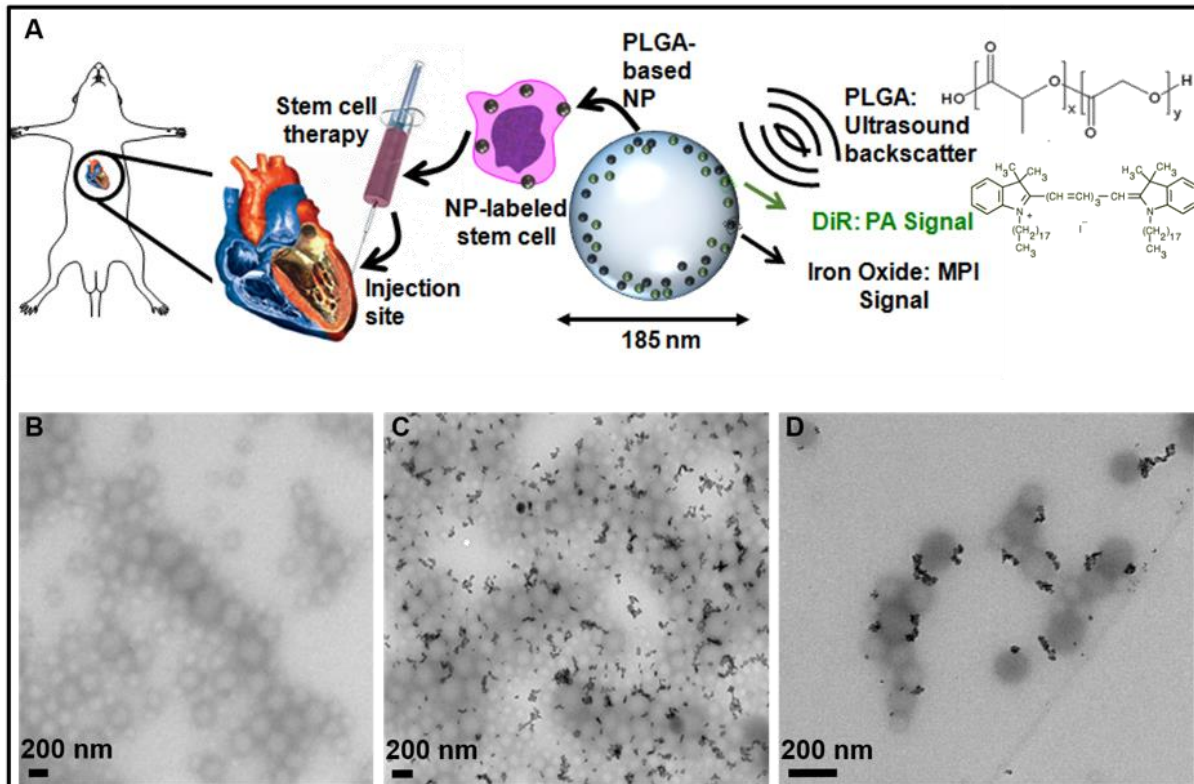


**Figure 4.1. Nanobubble Schematic and Synthesis.** A) Schematic of cells labeled with the trimodal nanobubble being injected intracardially into a murine model. PLGA and DiR molecular structures are shown. B) TEM image of PLGA nanobubbles without iron oxide. C) TEM image of iron oxide-loaded PLGA particles. D) Higher magnification TEM image of iron oxide-loaded PLGA particles.

#### 4.3.2 Optimization, Viability, and Cellular Uptake

**Figure 4.2** shows optimization parameters of the nanobubble synthesis, cell number detection, viability assay of hMSCs, and uptake of the nanobubbles. The effects of sonication time on the size (z-avg, nm) and polydispersity index (PDI) of the nanobubbles are shown in **Figures 4.2A** and **4.2B** respectively. The size of the nanobubbles was tuned by changing the sonication time from 1-10 minutes for the double emulsion and the impact on size was negligible after 5 minutes of sonication. This produced nanobubbles with a size of 185 nm +/- 2 nm (**Figure 4.2A**). The PDI decreased from 0.60 to 0.19 after increasing sonication time from 1 to 2 minutes; the PDI decreased to 0.15 after 5 minutes of sonication, indicating a monodisperse solution (**Figure 4.2B**).

Additionally, we varied the amount of iron oxide loading from 0-1000  $\mu\text{L}$  and showed no significant effect on size (**Supplementary Figure S1A**) or PDI (**Supplementary Figure S1B**) as measured by DLS. This indicates that the amount of iron oxide present in the nanobubbles did not significantly change the monodispersity of the solution. The final conditions chosen for the nanobubble synthesis were 5 minutes of sonication and 1000  $\mu\text{L}$  of iron oxide loading. These conditions resulted in iron oxide in approximately 70% of nanobubbles (**Table S1**) and a PDI of 0.15.

We measured the ultrasound (**Figure 4.2C**) and photoacoustic (**Figure 4.2D**) intensities of the nanobubbles in solution for 7 days and found consistent US and PA signal over days 1-4. After 7 days, the ultrasound signal of the nanobubbles decreased by 35%; the photoacoustic signal of the nanobubbles decreased 28%. We monitored the size (**Supplementary Figure S1C**) and PDI (**Supplementary Figure S1D**) of the nanobubbles in solution at room temperature for 4 days and found no significant difference in these parameters as measured by DLS indicating good stability of the nanobubble conformation for 4 days. Finally, we compared the ultrasound signal of control nanobubbles without DiR and iron oxide to ultrasound signal of the nanobubbles with these contrast agents (**Supplementary Figure S1E**). We found that the ultrasound signal of the nanobubbles with the contrast agents was 13% higher than the ultrasound signal of the nanobubbles without the contrast agents. This increase in ultrasound signal may be due to the higher impedance mismatch of particle with both iron oxide and PLGA than PLGA alone.

We imaged nanobubble-labeled cells in a phantom and found the detection level of hMSCs. **Figure 4.2E** shows the US and PA detection level of hMSCs labeled with nanobubbles (incubation time = 6 h, concentration = 240  $\mu\text{g}/\text{mL}$ ) in a phantom. The limit of detection of hMSCs labeled with nanobubbles was 10,461 cells for ultrasound imaging and 996 cells for photoacoustic

imaging. Previous research has indicated that the limit of detection for MPI is approximately 200 cells, and the theoretical detection limit of a single cell<sup>241</sup>. We measured the photoacoustic signal of 100,000 labeled cells (incubation time = 6 h, concentration = 240  $\mu\text{g/mL}$ ) in a phantom and found that the photoacoustic signal was detectable over the control non-labeled cells for 10 days (**Figure 4.2F**). We also conducted a viability analysis to show that the growth kinetics of the hMSCs were not affected by cell treatment with the nanobubbles (**Figure 4.2G**). There were no significant differences in viability ( $p > 0.05$ , two-tailed  $t$  test) for hMSCs that were treated (incubation time = 6 h, concentration = 240  $\mu\text{g/mL}$ ) compared to control cells; both cell populations doubled in approximately 3 days. TEM imaging of the treated hMSCs confirmed cellular uptake of the nanobubbles in the cytoplasm of the cell as indicated by the black arrows (**Figure 4.2H**).



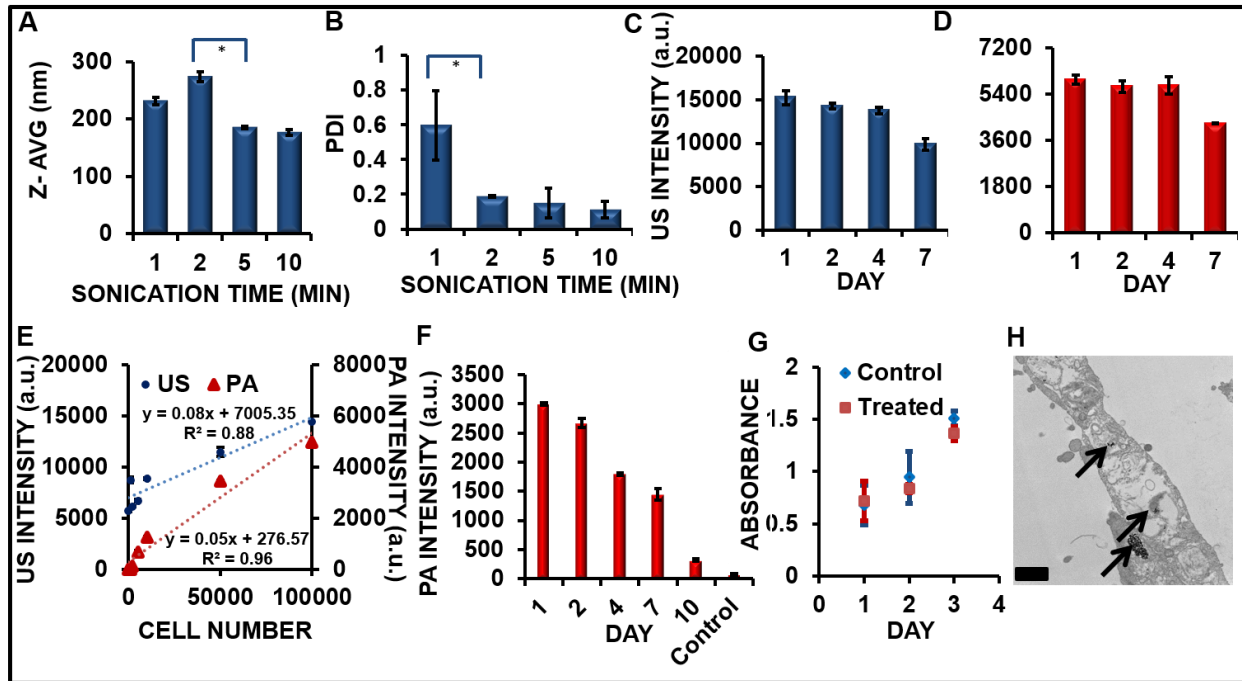


**Figure 4.2. Optimization of synthesis parameters and cell number detection.** **A)** Increased sonication time after 2 minutes resulted in a smaller nanobubble size with effects negligible after 5 minutes of sonication, \*p-value<0.05. **B)** Increasing the sonication time from 1 to 2 minutes resulted in a decrease in PDI from 0.60 to 0.19, \*p-value<0.05. **C)** The ultrasound signal of the nanobubble remained stable for 4 days and decreased by approximately 35% after 7 days (p-value<0.05). **D)** The photoacoustic signal of the nanobubble remained stable for 4 days and decreased by approximately 28% after 7 days (p-value<0.05). **E)** The limit of detection of hMSCs labeled with nanobubbles (incubation time = 6 h, concentration = 240  $\mu\text{g}/\text{mL}$ ) was 10,461 cells for ultrasound imaging and 996 cells for photoacoustic imaging. The primary y-axis indicates the ultrasound intensity (blue circles) of hMSCs treated with nanobubbles from 0-100,000 cells. The secondary y-axis indicates the photoacoustic intensity (red triangles) of hMSCs treated with nanobubbles from 0-100,000 cells. Error bars represent the standard error (n=8). **F)** Photoacoustic intensity data shows that cells (100,000 cells, incubation time = 6 h, concentration = 240  $\mu\text{g}/\text{mL}$ ) were detectable for 10 days in a phantom, p-value<0.05. **G)** A cell viability assay showing the growth kinetics of hMSCs. Treated cells (red squares) and control cells (blue diamonds) doubled in approximately 3 days. Error bars represent the standard error (n=8). **H)** TEM imaging of a hMSC treated with nanobubbles. The black arrows indicate the location of the nanobubbles within the cytoplasm of the hMSC. Scale bar = 0.5  $\mu\text{m}$ .

The zeta potential of the PLGA-only nanobubble was 1.25 mV compared to -0.169 mV for the version with iron oxide and DiR. The zeta potential of the iron oxide nanobubbles without DiR in water was -0.222 mV consistent with the slightly negative zeta potential of the final nanobubble. This indicates that the addition of the iron oxide caused the zeta potential to change from slightly positive to slightly negative in the final nanobubble.

### 4.3.3 Concentration Dependence and Cell Labeling Optimization

We imaged the nanobubbles in a phantom and found a linear relationship between the concentration of the nanobubble and the intensity for ultrasound, photoacoustic, and MPI (**Figure 4.3A**). This is an important relationship to quantify the amount of hMSCs present in cell tracking applications. **Supplementary Figure S1F** details this linear relationship between imaging modalities and shows  $R^2$  values of above 0.80 for all 3 modalities. We also identified the optimum incubation time and concentration for cell labeling. Dosage conditions were optimized so that MPI, US, and PA signals could be detected in hMSCs with no adverse effects on cell differentiation, protein expression, or toxicity.

The US, PA, and MPI signals of the labeled cells at various time points were studied to determine the signal intensity and proper conditions for cell labeling and *in vivo* studies. For ultrasound and photoacoustic studies, phantoms were prepared in a 1% agar gel for imaging. For MPI studies, cells were placed in tubes, sealed, and imaged. The concentration/time were held constant across the three different modalities and these images were processed as maximum intensity projections to help normalize the data across modalities. Uptake of the nanobubbles (concentration = 240  $\mu\text{g/mL}$ ) was observed in US, PA, and MP imaging at 4 h (**Figures 4.3B, 4.3D, 4.3F**) with p-values < 0.05, indicating statistically significant signal over the negative control (water). Flow cytometry data indicated fluorescent signal from the nanobubbles increasing from 0.25 hr incubation to 1 hour (**Supplementary Data, Figure S2A**). **Figure 4.3C** quantifies the US and PA image intensity. MPI signal was observed at 4 hours of incubation with the nanobubbles with a p-value < 0.05 (**Figures 4.3E, 4.4F**).

MTT 3-(4,5-dimethylthiazol-2-yl)-2,5-diphenyltetrazolium bromide (MTT) assays were performed to evaluate the toxicity of the nanobubbles. The results suggested that there was a slight

decrease of approximately 14% in viability of hMSCs treated for 24 hours (**Supplementary Data, Figure S3A**). Therefore, the optimal incubation time of the hMSCs with the nanobubbles was determined to be 6 hours to produce sufficient US, PA, and MPI signal while maintaining maximum cell viability. Other studies have found similar incubation times of nanoparticle-treated hMSCs ranging from 10 minutes – 24 hours. Uptake of mesoporous silica labeled with fluorescein isothiocyanate were found to be internalized as early as 10 minutes and maximized at 2 – 4 hours in hMSCs<sup>122</sup>; uptake of magnetic silica nanoparticles in hMSCs was observed at 1 hour<sup>242</sup>. Transfection agents combined with superparamagnetic iron oxides have also been used to study iron oxide uptake in various cell lines including hMSCs and showed uptake from 2 – 48 hours of incubation time<sup>243</sup>.

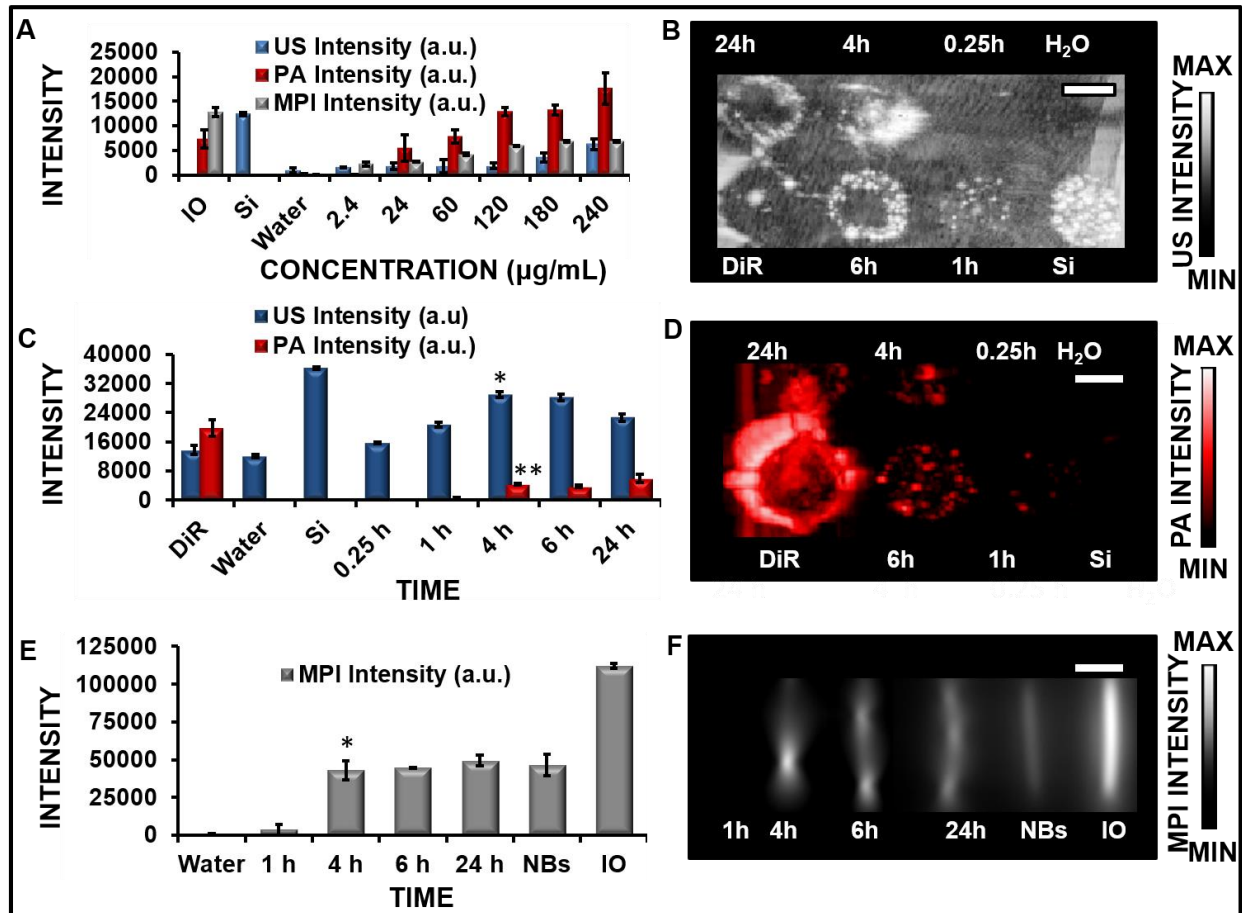


**Figure 4.3. Signal intensity of the multimodal contrast agent and effect of incubation time on labeled cells.** A) US, PA, and MPI signal of the nanobubbles as a function of concentration in a phantom are shown. IO = iron oxide nanoparticles (5.5 mg/mL) and Si = Stoba silica (SiO<sub>2</sub>) nanoparticles (5 mg/mL) are positive controls for MPI and US respectively; water is a negative control. There is a linear relationship in detection in these modalities, which is an important aspect in quantifying the number of labeled cells present. B) US imaging of hMSCs treated with nanobubbles from 0.25 to 24 hours, concentration = 240 µg/mL. C) US and PA imaging quantification at various times up to 24 hours. Signal was detected at 4 hours incubation for both modalities, compared to the negative control (water). \*, \*\* indicate p-value < 0.05 compared to the negative control. D) PA imaging of hMSCs treated with nanobubbles from 0.25 – 25 hours, concentration = 240 µg/mL, E) MPI quantification of hMSCs treated with nanobubbles from 1 - 24 hours, concentration = 240 µg/mL, \* indicates p-value < 0.05 compared to the negative control (water); nanobubbles (NBs, 24 µg/mL) and IO (5.5 mg/mL) are positive controls. F) MPI imaging data of hMSCs treated with nanobubbles at varying times from 1 - 24 hours, concentration = 240 µg/mL. MPI signal was detected at 4 hours of incubation. Error bars represent the standard error (n=8). Scale bars are 4 mm.

Next, we studied the impact that concentration (**Figure 4.4**) had on the hMSCs' signal intensity. The lowest concentration of nanobubbles that produce signal in hMSCs and significantly elevated relative to the untreated hMSCs was 180 µg/mL for US (**Figure 4.4A, 4.4C**), 120 µg/mL for PA (**Figure 4.4B, 4.4D**), and 24 µg/mL for MPI (**Figures 4.4E, 4F**). Flow cytometry data

further confirmed the effects of concentration on intensity and showed increasing intensity as concentration increased from 2.4-60  $\mu\text{g/mL}$  (Supplementary Data, Figure S2B). An MTT assay was also performed and showed no effect on toxicity of the cells at a concentration of up to 480  $\mu\text{g/mL}$  for cells treated for 8 hours (Supplementary Data, Figure S3B).

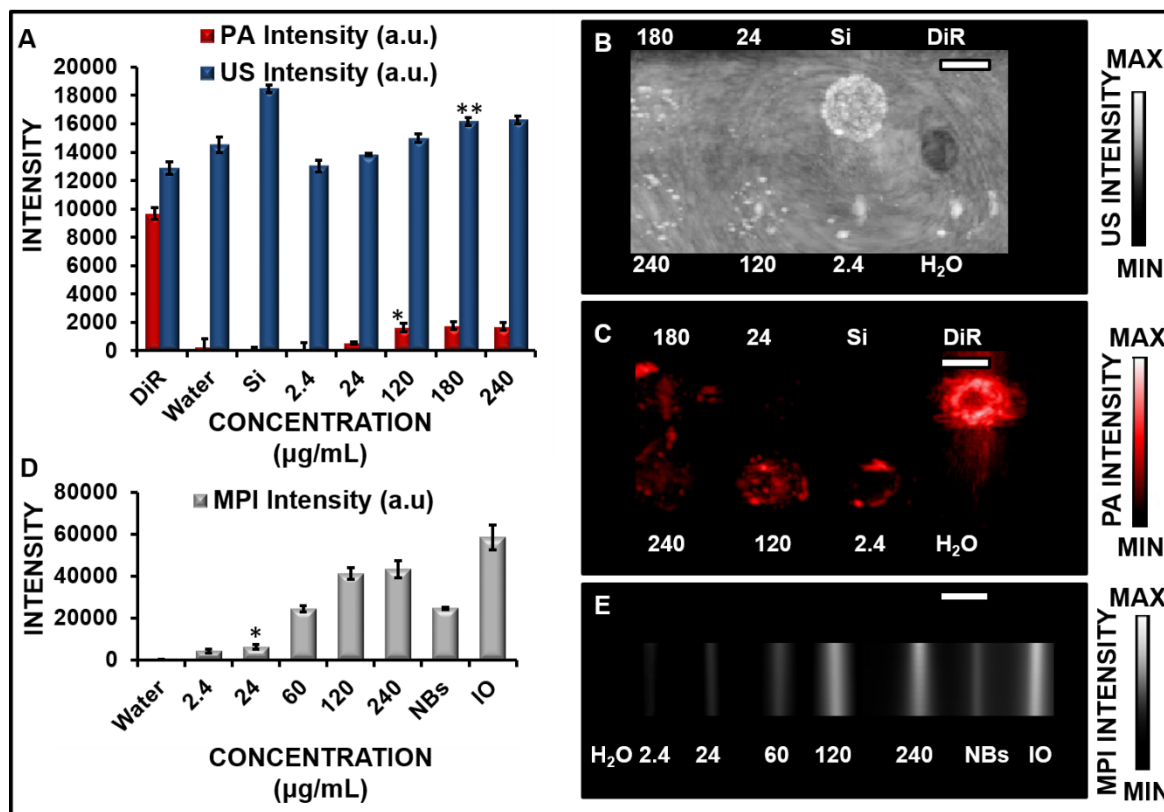


**Figure 4.4 Effect of concentration on US, PA, and MPI signal in labeled cells.** A) Quantification of US and PA imaging data of cells treated from 2.4 - 240  $\mu\text{g/mL}$  of nanobubbles for 6 hours. Si = Stoba silica ( $\text{SiO}_2$ ) nanoparticles (5 mg/mL) and DiR (5 mg/mL) were positive controls for US and PA imaging respectively. Water was a negative control. \*, \*\* = p-value < 0.05 compared to the negative control (water). B) US imaging of cells (100,000) treated with 2.4 - 240  $\mu\text{g/mL}$  of nanobubbles for 6 hours. C) PA imaging of cells (100,000) treated with 2.4 - 240  $\mu\text{g/mL}$  of nanobubbles for 6 hours. D) Quantification of MPI data from cells treated with 2.4 - 240  $\mu\text{g/mL}$  of nanobubbles for 6 hours where NBs = nanobubbles, IO = iron oxide (1 mg/ml) as a positive control. \* = p-value < 0.05 compared to the negative control (water). E) MPI imaging data of cells (100,000) treated with 2.4 - 240  $\mu\text{g/mL}$  of nanobubbles for 6 hours. Error bars represent the standard error (n=8). Scale bars are 4 mm.

Inductively coupled plasma optical emission spectrometer (ICP-OES) analysis was also conducted. ICP-OES measurements showed that there were  $1.04 \times 10^3$ ,  $1.40 \times 10^3$ ,  $4.54 \times 10^3$ ,  $9.07 \times 10^3$ ,  $11.1 \times 10^3$ , and  $11.2 \times 10^3$  iron oxide particles in cells treated with concentrations of

2.4, 24, 60, 120, 180, and 240  $\mu\text{g/ml}$  nanobubbles respectively for 6 hrs. This corresponds to 24, 32, 103, 205, 251, and 255 nanobubbles/cell respectively, as determined from the diameter of the iron oxide nanoparticles and their initial concentration. It is possible that this *in vivo* concentration resides in vacuoles within the cytoplasm<sup>244</sup> which prevent toxic effects.

**Pluripotency and Cytokine Analysis.** Next, we used differentiation reagents to determine if the nanobubbles affected the pluripotency of the hMSCs. The hMSCs labeled with nanobubbles differentiated into lineages of adipocytes and osteocytes, similar to the untreated hMSCs with similar morphology and staining. We labeled cells with the nanobubbles (240  $\mu\text{g/ml}$ , 6 hrs) and washed the cells 3 times with PBS to remove non-endocytosed nanobubbles. We then monitored the differentiation of the cells for 3 weeks in induction and control media.

**Figures 4.5A and 4.5B** show Von Kossa staining for osteocytes of noninduced, unlabeled and labeled cells. There was no significant black calcium staining for these non-induced cells. **Figures 4.5C and 4.5D** show Oil Red O staining for adipocytes; no red staining was observed for these cells. **Figures 4.5E and 4.5F** show unlabeled and labeled cells in typical media. There were no significant morphological changes suggesting that the nanobubble does not induce spontaneous differentiation by itself. Unlabeled and labeled hMSCs differentiated into osteogenic (**Figures 4.5G, 4.5H**) and adipogenic cell lines (**Figure 4.5I, 4.5J**) with the use of induction media. Osteogenic induction produced black calcium-staining from the Von Kossa stain in the treated and untreated cells. Adipogenic induction produced characteristic lipid-containing vacuoles<sup>245</sup> and red staining with Oil Red O in the treated and untreated cells. Image analysis of the osteogenic cell differentiation images (**Figure 4.5K**) and adipogenic cell differentiation images (**Figure 4.5L**) showed that labeling the cells with the nanobubbles did not reduce the number of differentiated cells. These findings indicated that the hMSCs still retained the ability to differentiate into

adipogenic and osteogenic cells. Flow cytometry data indicated that the labeled hMSCs retained surface markers CD90, CD73, and CD105 (**Figure 4.5M, Supplementary Data, Figures S4A, S4B**) as compared to unlabeled hMSCs, indicating that the cells were still expressing characteristic stem cell phenotypes. Additionally, a cell migration assay was conducted to ensure that the hMSCs retained the ability to migrate (**Supplementary Data, Figures S5A-F**). We found that cells treated with nanobubbles (6 h, 240  $\mu\text{g/mL}$ ) migrated at a similar rate to untreated cells over 7 days. Overall, these results suggest that the nanobubble treatment did not affect the differentiation, surface marker expression, or migration ability of the hMSCs as compared to untreated hMSCs.

There are three main types of endocytosis processes involving nanomaterials including caveolae-mediated endocytosis, clathrin-mediated endocytosis, and micropinocytosis. We used Dynasore, a clathrin-mediated endocytosis inhibitor, to treat the cells to determine if cell labeling was hindered. Cells treated with Dynasore and labeled with nanobubbles did not show fluorescence (**Supplementary Figure S4C**) compared to cells labeled with nanobubbles (**Supplementary Figure S4D**), indicating clathrin-mediated endocytosis as the mechanism of cellular uptake.

We also studied the secretome of the nanobubble-treated and control cells by measuring 17 cytokines in cell culture media to determine if expression patterns changed with the nanobubble treatment. The treated hMSCs showed increased expression over untreated cells for ferritin and alpha-1 antitrypsin of 5.3 and 2.8 times, respectively (**Figure 4.5N**). Other cytokines tested did not show significantly increased expression over untreated cells. Ferritin, an iron binding protein, has been implicated in the biodegradation of magnetic iron oxide nanoparticles, suggesting that the hMSCs were metabolizing the iron oxide<sup>246</sup>. Alpha-1 antitrypsin has been shown to increase

fibroblast proliferation by inducing the activation of p42<sup>MAPK</sup> and p44<sup>MAP</sup> pathways<sup>247</sup>, which may suggest that the treated cells had increased fibroblast production as compared to the nontreated cells. However, the other 15 cytokines measured were detected at the same or lower levels in treated cells as compared to untreated cells, indicating that the expression levels of these proteins were not dysregulated by treating the hMSCs with nanobubbles.



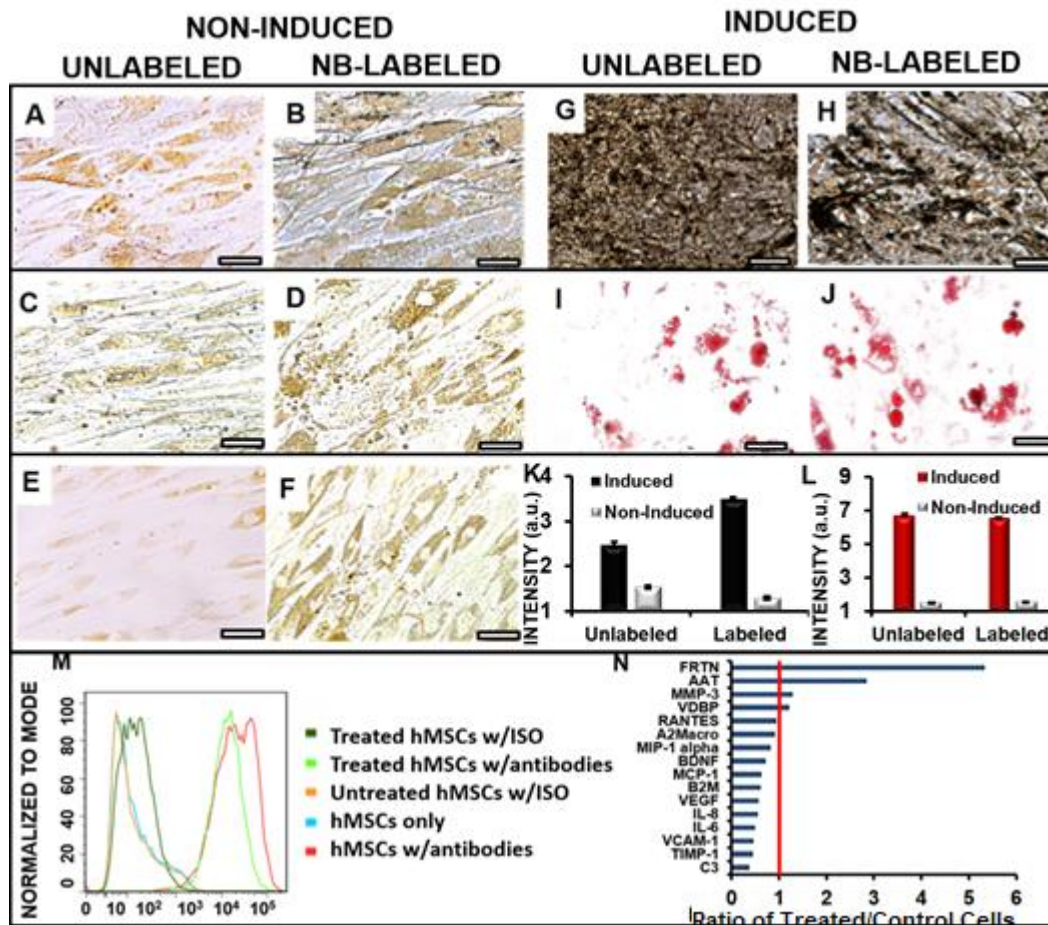


**Figure 4.5. The differentiation ability of hMSCs is unaffected by the nanobubble labeling** (240  $\mu\text{g/ml}$  nanobubbles, 6 hours incubation). Panels **A-F** indicate control cells without induction media. Panels **G-J** indicate cells with induction media. **A)** Osteogenic staining of noninduced, unlabeled cells did not produce black calcium staining. **B)** Osteogenic staining of noninduced, labeled cells did not produce significant black calcium staining. **C)** Adipogenic staining of noninduced, unlabeled cells did not produce characteristic red staining. **D)** Adipogenic staining of noninduced, labeled cells did not produce characteristic red staining. **E)** Unlabeled cells in typical media. **F)** Labeled cells in typical media. **G)** Induced, unlabeled cells showed characteristic black calcium staining from the Von Kossa stain. **H)** Induced, labeled cells showed characteristic black calcium staining from the Von Kossa stain. **I)** Unlabeled cells in adipogenic media showed characteristic red staining and globular morphology from the Oil Red O stain. **J)** Labeled cells in adipogenic media showed characteristic red staining and globular morphology from the Oil Red O stain, Scale bar for all images = 100  $\mu\text{m}$ . **K)** Image analysis of the osteogenic cell differentiation images showed that labeled cells did not reduce the number of differentiated cells for cells treated with induction media. **L)** Image analysis of the adipogenic cell differentiation images showed that labeled cells did not reduce the number of differentiated cells for cells treated with induction media. **M)** CD73 flow cytometry data showing that treated hMSCs retain the ability to express characteristic phenotypes. **N)** Cytokine analysis of labeled hMSCs showing the ratio of expression to unlabeled cells. Ferritin (FRTN), Alpha-1-Antitrypsin (AAT), Matrix Metalloproteinase-3 (MMP-3), Vitamin D-Binding Protein (VDBP), T-Cell-Specific Protein RANTES (RANTES), Alpha-2-Macroglobulin (A2Macro), Macrophage Inflammatory Protein-1 alpha (MIP-1 alpha), Brain-Derived Neurotrophic Factor (BDNF), Monocyte Chemotactic Protein 1 (MCP-1), Beta-2-Microglobulin (B2M), Vascular Endothelial Growth Factor (VEGF), Interleukin-8 (IL-8), Interleukin-6 (IL-6), Vascular Cell Adhesion Molecule-1 (VCAM-1), Tissue Inhibitor of Metalloproteinases 1 (TIMP-1), Complement C3 (C3).

***In Vivo* Imaging.** **Figure 4.6** shows real-time PA and US imaging for clear anatomic differentiation and high contrast of injections of labeled hMSCs into nude mice. Here, 800,000 hMSCs treated with nanobubbles labeled with 240  $\mu\text{g/ml}$  nanobubbles for 6 hours were injected intramyocardially into nude mice ( $n=3$ ). Ultrasound was used in real-time to guide the initial injection of the stem cells, photoacoustic imaging was used to confirm the location of the stem cells in the myocardial tissue with higher contrast than ultrasound, and MPI was used to confirm location of the stem cells long-term due to its very high contrast above background and depth of penetration. **Figures 4.6A-D** show the longitudinal axis view of the mouse hearts. **Figure 4.6A** shows pre-injection of PBS, a negative control, and **Figure 4.6B** shows post-injection of PBS. **Figure 4.6C** shows pre-injection of labeled cells and **Figure 4.6D** shows post injection of labeled cells. US imaging showed a 3.8-fold increase of labeled cells post-injection (**Figure 4.6D**) compared to baseline, and PA imaging showed a 10.2-fold increase in signal post-injection (**Figure 4.6D**); injection of PBS did not show any increase in signal. **Figure 4.6F** shows MPI imaging data of mice (M1, M2) injected with 800,000 nanobubble-labeled hMSCs; M3 was a negative control. **Figure 4.6G** shows MPI quantification of the injections. The MPI intensity of the nanobubble-treated hMSCs injected into the hearts of mice (M1 and M2) was compared to the negative control (M3). The signal intensity from mice M1 and M2 was 25.8 and 21.2 times respectively higher than the untreated mouse M3. Previous studies have indicated a spatial resolution in MPI of approximately  $1.5 \text{ mm} \times 3.0 \text{ mm} \times 3.0 \text{ mm}$  in z-, x- and y-direction, consistent with our results<sup>56</sup>. The signal intensity in MPI is proportional to the amount of contrast agent present<sup>56</sup>, thereby making MPI a viable option for tracking the number of stem cells *in vivo*. **Supplementary Data, Figures S6A-E** show imaging data of 100,000 – 800,000 hMSCs injected subcutaneously into a murine model, showing the ability to discriminate between different cell numbers *in vivo*. This is

important to track the number of injected stem cells *in vivo*. Additionally, the hMSCs were tracked *in vivo* and showed signal after 3 days of injection (**Supplementary Data, Figure S7**).

One of the challenges of stem cell imaging is the real-time monitoring of cellular injection with differentiation of anatomical features. The Video **S1** shows video of an ultrasound-guided intramyocardial injection of nanobubble-treated hMSCs into a live mouse. The contrast increased 3.8-fold after the injection of the nanobubble-treated hMSCs. Finally, histology sections of labeled-hMSCs injected into cardiac tissue of living mice showed fluorescent signal indicating that the labeled cells were in the cardiac tissue (**Supplementary Data, Figures S8A, B**).

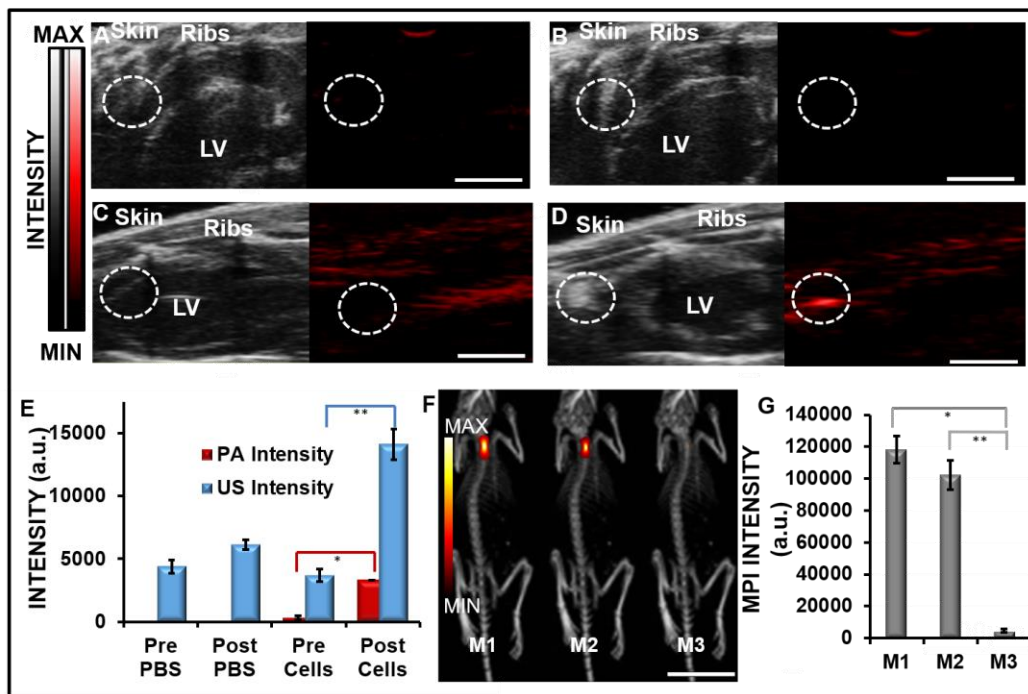


**Figure 4.6. In vivo imaging.** **A**) Ultrasound (black and white) and photoacoustic images (red) pre-injection of PBS show low signal intensity in circled areas of the longitudinal axis of cardiac tissue. LV indicates left ventricle. **B**) Ultrasound and photoacoustic images post-injection of PBS show low signal intensity, **C**) Ultrasound and photoacoustic images before injection of labeled hMSCs, **D**) Post-injection of 800,000 labeled hMSCs (240  $\mu\text{g/ml}$  nanobubbles, 6 hours incubation). Scale bar for images A-D is 0.5 cm. **E**) Quantification of US and PA signal increase post-injection of labeled cells, **F**) MPI imaging of mice injected with labeled hMSCs (yellow/red images, 240  $\mu\text{g/ml}$  nanobubbles, 6 hours incubation). Mice M1 and M2 were injected with 800,000 labeled hMSCs. Mouse M3 was a negative control. Scale bar is 2.5 cm. **G**) Quantification of MPI data. \*, \*\* indicate p-values <0.05.

#### 4.4 Conclusion

We synthesized PLGA-based iron oxide nanobubbles labeled with DiR to use as a trimodal contrast agent to label hMSCs. The nanobubbles were imaged *ex vivo* in an agarose phantom and 3D-printed based phantom; they were imaged *in vivo* after intramyocardial injection. We confirmed that cell metabolism, proliferation, and differentiation ability were not adversely affected by treatment with the nanobubbles. This suggests that this contrast agent can be used with hMSCs for improving stem cell therapy imaging. Clinical trials typically involve millions of cells<sup>126, 128</sup> and ultra-low cell number detection is rarely a true clinical need. However, future research directions include more careful evaluation of the detection limit and *in vivo* tracking capabilities of this approach. Alternative applications include immune cell trafficking such as imaging macrophages and/or Car T-cells *in vivo*.

#### 4.5 Acknowledgements

Jeanne E. Lemaster acknowledges funding from the NIH Institutional National Research Service Award T32 - Cancer Researchers in Nanotechnology (Dong, Kummel). J. Lemaster would like to thank C. Isaac and P. Castillo for ICP-OES analysis and J. Gaudet and A. Clemmensen for magnetic particle imaging scans. Jesse V. Jokerst acknowledges funding from the NIH R00 HL117048 and DP2 HL137187 and infrastructure from S10OD021821. This work was performed in part at the San Diego Nanotechnology Infrastructure (SDNI) of UCSD, a member of the National Nanotechnology Coordinated Infrastructure, which is supported by the National Science Foundation (Grant ECCS-1542148).

Chapter 4, in full, is a reprint of the material as it appears in ACS Applied Nano Materials, Lemaster, Jeanne E., Fang Chen, Taeho Kim, Ali Hariri, and Jesse V. Jokerst, 2018. The dissertation author was the primary investigator and author of this paper.

## 4.6 Appendix

**Table S1. A comparison of different field of views in TEM imaging.** The total number of nanobubbles was counted for five fields of view. The number of nanobubbles without iron oxide particles was counted. The number of free iron oxide particles was also counted. Approximately 70% of the nanobubbles contain iron oxide particles.

	Total number of nanobubbles	Nanobubbles without iron oxide particles	Free iron oxide particles	% Nanobubbles without iron oxide particles	% Nanobubbles with iron oxide particles
Field of View 1	175	90	0	51%	49%
Field of View 2	60	16	7	27%	73%
Field of View 3	58	9	22	16%	84%
Field of View 4	110	29	13	26%	74%
Field of View 5	29	9	9	31%	69%

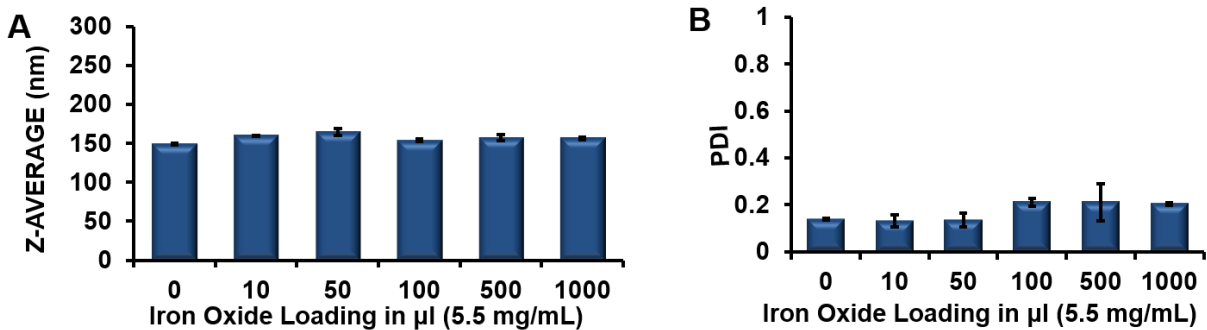


**Figure S1.** The effect of iron oxide loading on particle size (z-avg) and PDI. **A)** Varying the amount of iron oxide loading (from 0-1000  $\mu\text{l}$ ) did not significantly affect the particle size. **B)** Increasing the iron oxide loading (from 0-1000  $\mu\text{l}$ ) did not significantly affect the PDI.

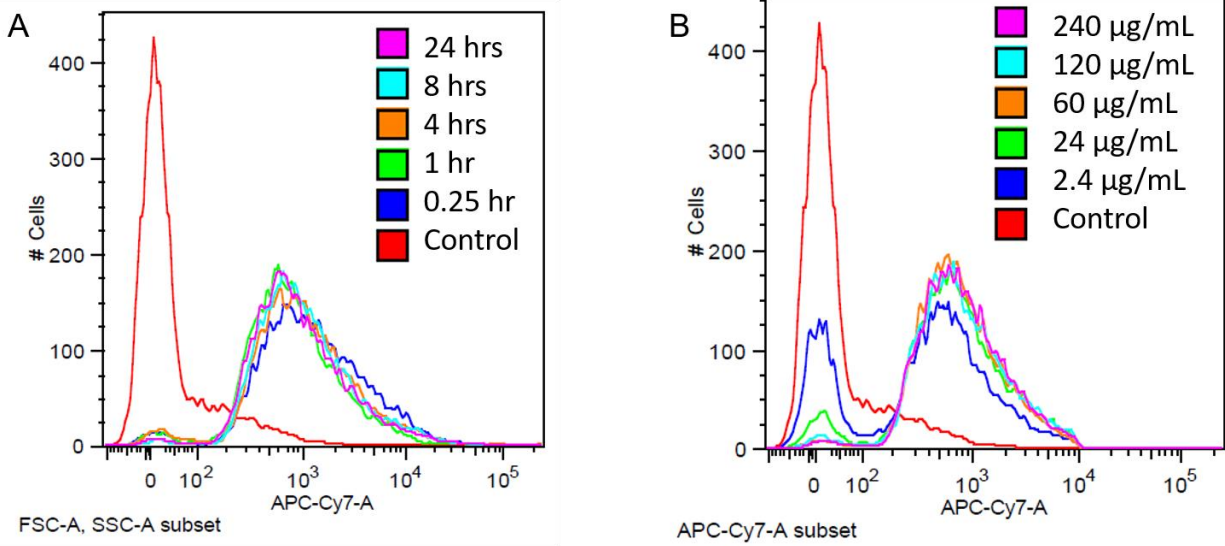


**Figure S2. Flow Cytometry data of hMSCs treated with nanobubbles.** The control indicates cells not treated with nanobubbles. **A)** Effects of varying incubation time for hMSCs treated with nanobubbles at a concentration of 240 µg/mL. Increasing incubation time from 0.25 – 24 hrs showed higher cell populations labeled. **B)** Effects of varying concentration for hMSCs treated for 8 hours with nanobubbles (µg/mL). Increasing the concentration of nanobubbles showed an increase in the fluorescence of the cells.

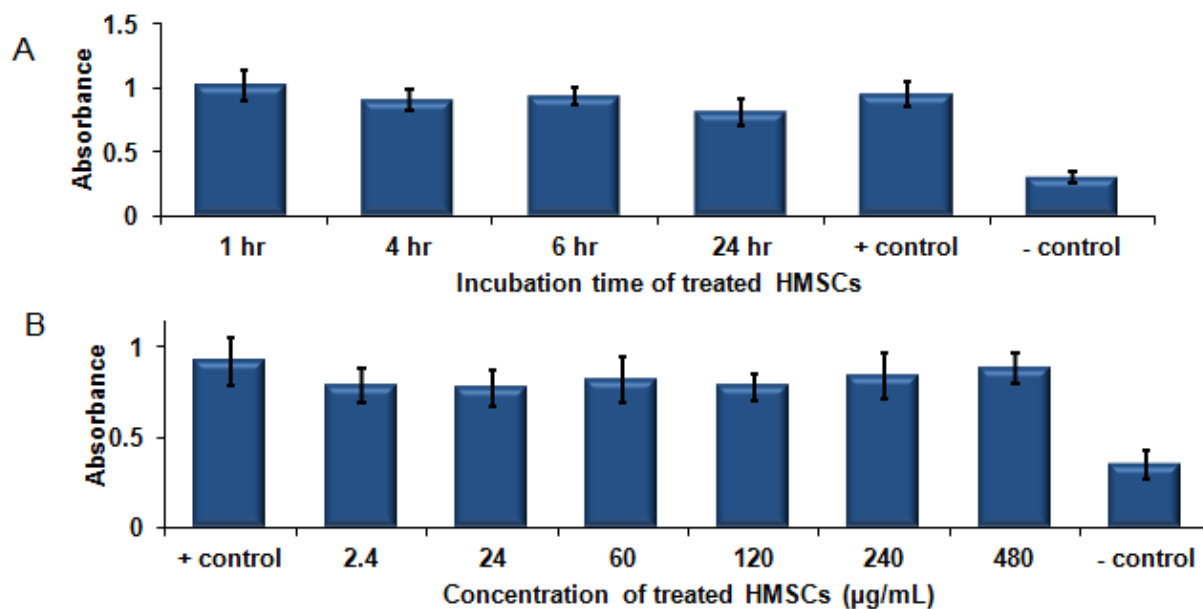


**Figure S3. MTT assays of HMSCs treated with nanoparticles.** **A)** Effects of incubation time for HMSCs treated with nanobubbles at a concentration of 240 µg/mL. Cell viability decreased by approximately 21% at 24 h of incubation with the nanobubbles. **B)** Effects of concentration for HMSCs treated for 8 hours at varying concentration with nanoparticles. The concentration up to 480 µg/mL of nanobubbles did not show toxic effects towards cells. The error bars represent the standard error between samples (N=8).



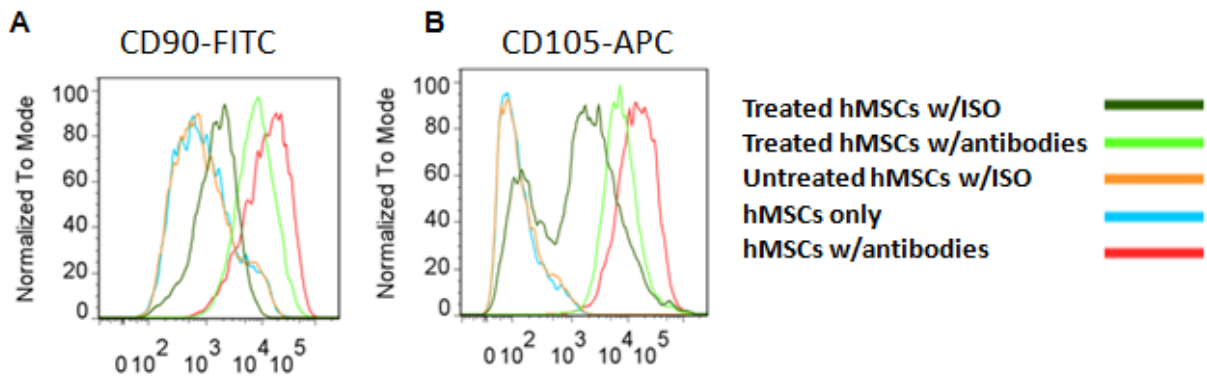


**Figure S4. Flow cytometry data showing that nanoparticle-treated hMSCs retain characteristic markers as compared to untreated hMSCs.** The treated hMSCs showed positive expression for surface markers (A) CD90 and (B) CD105. Isotype (ISO) controls for unlabeled and labeled hMSCs had low signal.

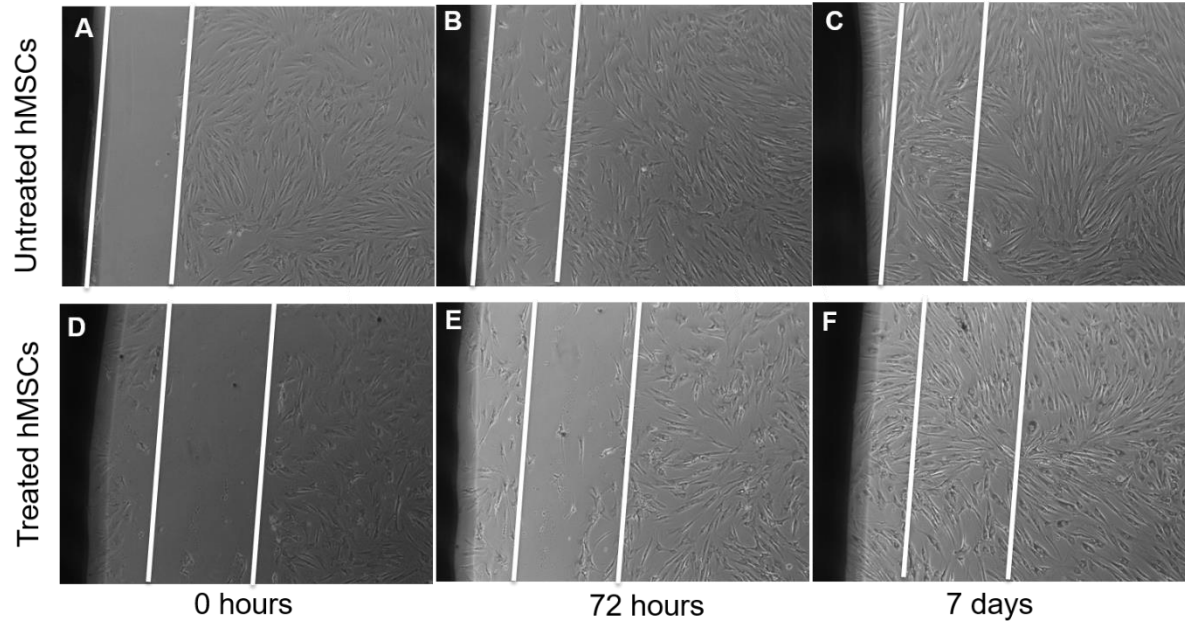


**Figure S5. Cell migration assay.** The migration ability of hMSCs treated with nanobubbles (240  $\mu\text{g}/\text{mL}$  for 6 h) was studied by Leica optical microscopy with a monochrome camera at (A, C) 0 hours, (B, E) 72 hours, and (C, F) 7 days. The white line indicates the area where cells were removed. The black area is the fiducial marker used to orient the plate for imaging. The treated hMSCs (D, E, F) migrated to an area depleted of hMSCs in 7 days, similar to the untreated hMSCs (A, B, C).

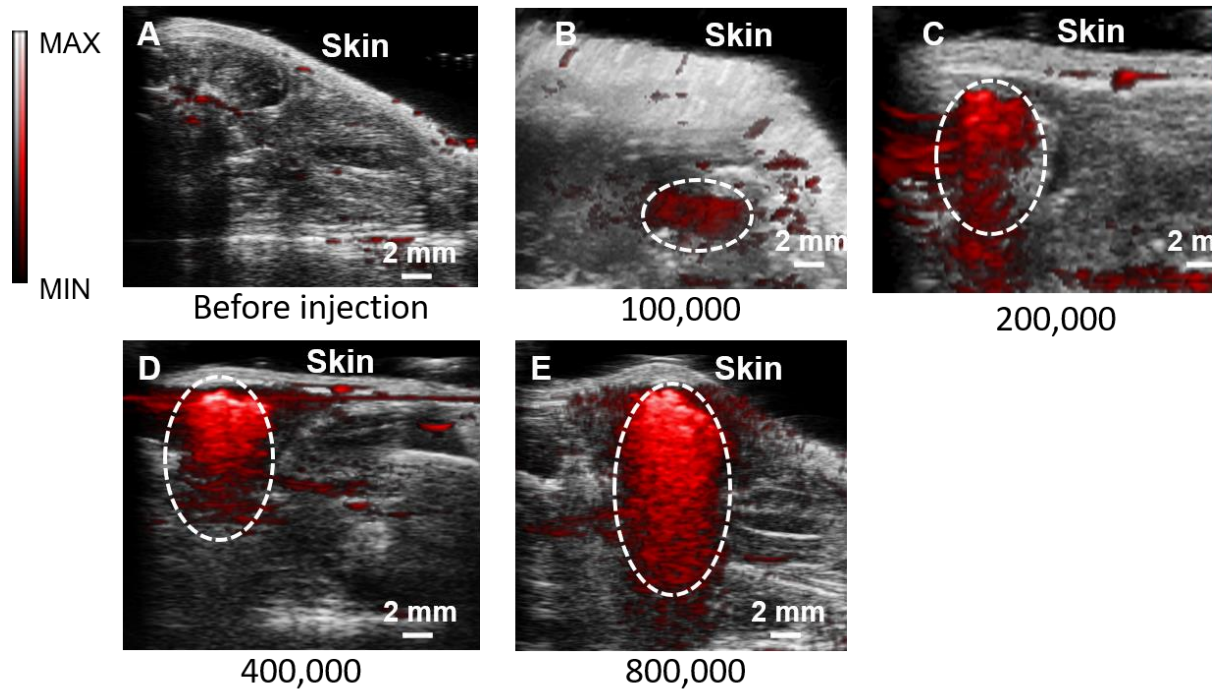


**Figure S6. Subcutaneous injections of varying numbers of hMSCs treated with nanobubbles at a concentration of 240  $\mu\text{g}/\text{mL}$  for 6 h. A) Before injection, B) Injection of 100,000 treated hMSCs, C) Injection of 200,000 treated hMSCs, D) Injection of 400,000 treated hMSCs, E) Injection of treated 800,000 hMSCs. The red area within the dotted white circle shows the PA signal from the injected cells.**

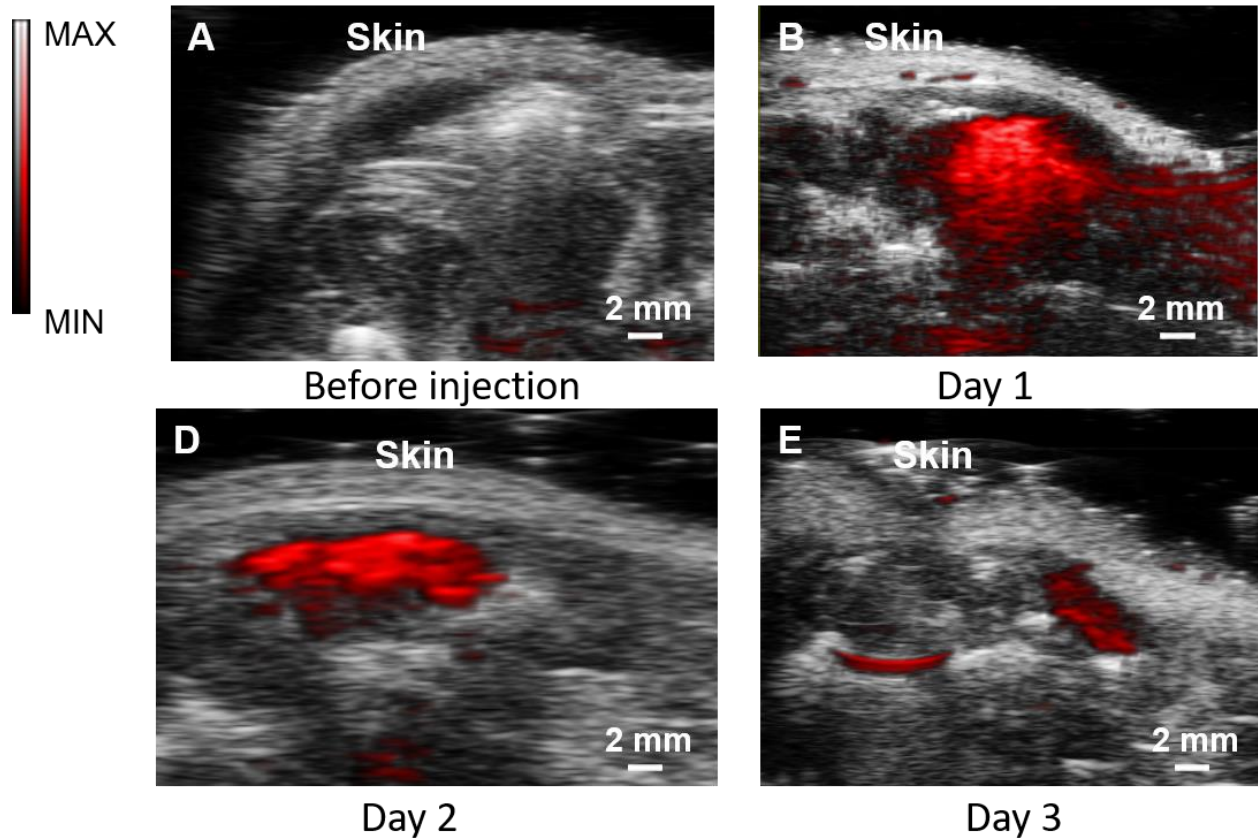


**Figure S7. The signal from the nanobubble-treated hMSCs decreased from Day 1 – Day 3 in subcutaneous injections. A) Before injection, B) Day 1 of injection, C) Day 2 after injection, D) Day 3 after injection. hMSCs were treated with 240  $\mu\text{g}/\text{mL}$  nanobubbles for 6 h. 400,000 hMSCs were injected.**

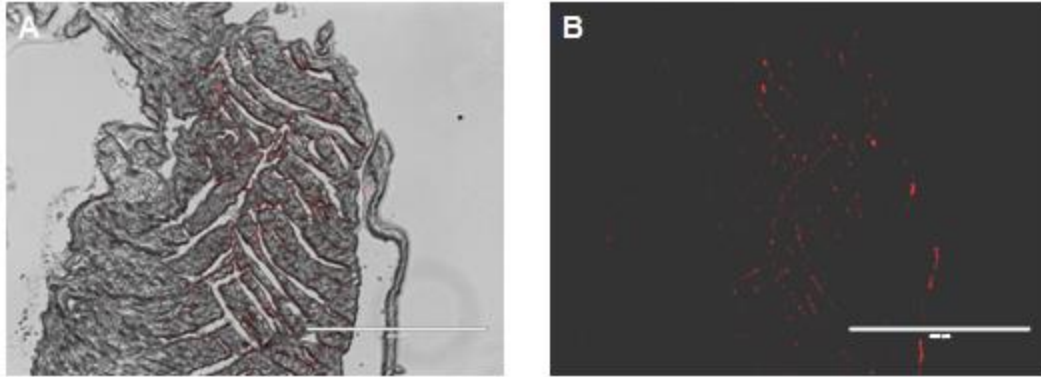


**Figure S8. Histology sections show nanobubble-treated hMSCs were injected into mouse cardiac tissue (red dots).** **A)** Overlay microscopy. **B)** Fluorescent microscopy of the nanobubble-injected hMSCs with Cy7 filter. The red fluorescence shows the presence of cells labeled with nanobubbles in the cardiac tissue. 800,000 nanobubble-treated hMSCs (240  $\mu\text{g}/\text{mL}$  of nanobubbles for 6 h) were intramyocardially injected into a live mouse. Scale bar = 400  $\mu\text{m}$ .

## CHAPTER 5: PHOTOACOUSTIC IMAGING QUANTIFIES DRUG RELEASE FROM NANOCARRIERS VIA REDOX CHEMISTRY OF DYE-LABELED CARGO

### 5.1 Introduction

Nano-based drug delivery can improve bio-distribution, enhance efficacy, and reduce toxicity.<sup>248</sup> The therapeutic efficacy is highly dependent on the drug pharmacokinetics (PK) and pharmacodynamics (PD), but such kinetics can be difficult to measure *in vivo*. Recently, the failure of a liposomal cisplatin formulation was attributed to poor tumor penetration and insufficient free drug release during the phase II clinical study.<sup>249</sup> Thus, monitoring bio-distribution of both the nanoparticle carrier and their active pharmaceutical ingredient after systemic administration is a top challenge in nanomedicine.<sup>250</sup> While periodic blood sampling coupled with LC-MS analysis<sup>251</sup> will likely remain the gold standard for PK/PD, it does not offer anatomic information on the site of release, timing, or release.<sup>252-253</sup>

Imaging is an important solution to this vexing problem. Radiolabeled analogues or fluorescent tags can monitor bio-distribution after administration for image-guided drug delivery.<sup>254-255</sup> However, these approaches are often “always on” and cannot answer questions about drug status, i.e., encapsulated or released from carrier. While fluorescence resonance energy transfer (FRET) has been used as a strategy to monitor release<sup>256-257</sup>, fluorescence imaging suffers from poor resolution in deep tissue imaging. In contrast, photoacoustic imaging offers high contrast imaging and can be easily co-registered to anatomic ultrasound imaging.<sup>258</sup> It does not use ionizing radiation and offers video frame rates.<sup>259</sup> Some recent approaches using photoacoustics for drug delivery are core-satellite nanoparticle system and polylactic acid-based particles to monitor distribution of carrier particles with photoacoustics.<sup>260-261</sup>

Here, we report a strategy to monitor drug release from a nanocarrier via photoacoustic imaging. This strategy utilizes the popular ‘blue bottle reaction’ where the clinically approved methylene blue (MB) switches between a colored oxidized form and a colorless reduced form.<sup>262</sup> Such switching leads to “turn-on” photoacoustic signal as the MB is oxidized upon release from the protective nanocarrier<sup>263</sup> even when covalently conjugated to paclitaxel. After preparing this drug-dye conjugate, we evaluated the IC<sub>50</sub> on CT26 cells and then used an *in vivo* model to validate the imaging and therapeutic features of this construct.

## 5.2 Materials and Methods

**Reagents.** Paclitaxel was purchased from Biotang Inc. (Massachusetts, USA). Polyvinyl alcohol (PVA), polylactic-co-glycolic acid polymer (PLGA), succinic anhydride, ascorbic acid, and D,L-dithiothreitol (DTT) were purchased from Sigma Aldrich Inc. (Missouri, USA) and used without further purification. Normal mouse serum was purchased from Fisher Scientific (Texas, USA). D-Luciferin was purchased from Biosynth (Illinois, USA). RPMI 1640 media was purchased from Sigma Aldrich Inc. (Missouri, USA). CT26-Luc cells were a kind gift from Prof. Nicole Steinmetz.

**Instruments.** Mass spectrometry of all intermediates was performed using the Micromass Quattro Ultima Mass spectrometer using electrospray ionization mass spectrometer. Liquid chromatography-mass spectrometry (LC-MS) analysis of paclitaxel methylene blue conjugate (PTX-MB), 2'-succinimidylpaclitaxel (PTX-COOH), and hydroxyl-terminated methylene blue (III) was performed using the Thermo LCQ deca-MS mass spectrometer equipped with HP1100 LC station. The <sup>1</sup>H NMR spectrum of PTX-MB was acquired on Bruker 300 NMR spectrometer in deuterated chloroform medium. Transmission electron microscopy (TEM) micrographs of the particles were recorded on a JEOL JEM 4000 transmission electron microscope. UV-Vis spectra

were recorded using Spectromax M5 plate reader using a 75  $\mu$ l quartz cuvette. Photoacoustic imaging was performed with a Vevo 2100 instrument (Visualsonics) with a 21 MHz-centered transducer. IVIS imaging utilized a Perkin-Elmer Illumination system and LivingImage software.

**Synthesis of precursors.** PTX-COOH<sup>264</sup> and the hydroxy-terminated dye (III), 3-(dimethylamino)-7-((2-hydroxyethyl)(methyl)amine) phenothiazin-5-ium iodide<sup>265</sup> were synthesized according to the previously reported procedures. (See Supporting Information).

**Synthesis of paclitaxel-methylene blue conjugate (PAC-MB).** In a typical reaction, hydroxy-terminated dye (III) (M.W., 441.33 g/mol; 2.0 mg;  $5.66 \times 10^{-6}$  mol; 1.0 equiv.) and PTX-COOH (M.W. = 953.97; 17.5 mg;  $1.80 \times 10^{-5}$  mol; 3.1 equiv.) were first dissolved in dry chloroform (4 mL) under nitrogen atmosphere. Next, N,N'-dicyclohexylcarbodiimide (DCC) (M.W. = 206.33 g/mol; 4.5 mg ;  $2.18 \times 10^{-5}$  mol; 3.85 equiv.) dissolved in 1 mL of dry chloroform and N,N-dimethylaminopyridine (M.W. = 122.17 g/mol; 0.4 mg;  $1.63 \times 10^{-6}$  mol; 0.57 equiv.) dissolved in dry chloroform (400  $\mu$ l) were directly injected into the reaction vessel. The mixture was stirred under a nitrous atmosphere for 3 hours, and product formation was monitored with electrospray ionization (ESI) mass spectrometry (MS). The crude reaction mixture was evaporated under vacuum. Finally, the purified product was obtained by reverse phase high performance chromatography (RP-HPLC) with a mobile phase of 30-60% acetonitrile in water with trifluoroacetic acid (overall concentration 0.01% v/v). The fraction with product was collected and lyophilized. <sup>1</sup>H NMR (300 MHz, CDCl<sub>3</sub>)  $\delta$  0.5-1.3 (m, 13 H), 1.4-1.9 (m, 11H), 2.0-2.2 (m, 4 H), 2.2-2.7 (mm, 7H), 3.0-3.6 (m, 8H), 3.7-4.5 (m, 7H), 7.1-7.4 (m, 10H), 7.8-8.3 (m, 6H) ppm; MS (LC-ESI) m/z calcd for C<sub>88</sub>H<sub>73</sub>N<sub>4</sub>O<sub>17</sub>S<sup>+</sup> 1249.47; Found 1249.79. <sup>1</sup>H NMR and liquid chromatographic mass spectrometry (LC-MS) were used to analyze the yield of the reaction and to study the purity.



### **Synthesis of PLGA nanoparticles with reduced PTX-MB (PTX-MB @ PLGA NPs).**

To prepare the PLGA nanoparticles, poly(D,L-lactic-co-glycolic acid) (60 mg, Resomer RG 504 H; acid terminated;  $M_w$  38000-54000; lactide:glycolide 50:50) and PTX-MB (M.W. 1377.29 g/mol; 2.0 mg;  $1.46 \times 10^{-6}$  mol) of PTX-MB were dissolved in chloroform (2 mL). Then, 1,4-dithiothreitol (DTT) (M.W. 154.25 g/mol; 4.6 mg;  $2.98 \times 10^{-5}$  mol) was added dissolved in the mixture and ethylenediamine (M.W. = 60.10 g/mol; 1  $\mu$ L;  $7.47 \times 10^{-6}$  mol) was spiked into the solution. The deep blue solution turned to colorless within 120 s. The polymer solution with PTX-MB was then mixed with 3 mL of aqueous solution containing 2% polyvinyl alcohol (PVA) (M.W. range 31000-50000; 2 % w/v) and ascorbic acid (M.W. = 176.12 g/mol; 60 mM) by vortexing the mixture vigorously to form an emulsion. The emulsion was then mixed with 9 mL PVA solution (2% w/v) and sonicated with a probe sonicator for 5 minutes with 10 s bursts and a gap of 10 s between each burst. The resulting white emulsion was mixed with 12 mL PVA solution (2% w/v) and stirred at 600 rpm under a constant stream of nitrogen for 12 h to remove chloroform.

The PLGA NPs with PTX-LMB were isolated by centrifuging the emulsion at 14000 rpm for 10 minutes. The particles were washed twice with 60 mM aqueous solution of ascorbic acid and once with pure Millipore water purged with nitrogen to avoid oxidation of the PTX-MB. The particles were re-suspended in nitrogen-purged Millipore water with trehalose (7.5 mg mL<sup>-1</sup>) (cryoprotectant) was added to the particle suspension<sup>266-267</sup>. Finally, the suspension was frozen and lyophilized at 0.02 mBar. The lyophilized particles with trehalose were stable for over a period of 3-4 months when stored in dark conditions at -20 °C. Experimental controls were similarly prepared.

***In vitro* study of drug release.** PTX-MB @ PLGA NPs (10 mg) were suspended in deionized water and divided into 10 equal portions in separate containers. The portions of PLGA

NP suspensions were lyophilized and mixed with mouse serum (200  $\mu$ L; 20 % v/v in PBS) <sup>268</sup> in phosphate buffer saline with sonication for 5 minutes. The particle suspensions were incubated for 1, 3, 6, 12, 24, 48, 72, 96, or 120 hours. The particle suspensions were mixed initially for 10 minutes in a rotary mixer and then incubated at 38 °C. The samples were mixed for 10 minutes every 24 h. The supernatants from each samples were placed in separate 0.86 mm polyethylene tubes to acquire 3D photoacoustic image with excitation at 680 nm.

**Cell culture.** Colon cancer cell line CT26 labeled with luciferase were cultured using RPMI1640 media supplemented with fetal bovine serum (10%), L-glutamine (2 mM), sodium pyruvate (1mM), and 1% antibiotic-antimycotic. Cells were incubated at 37 °C and media was replaced every 1-2 days. Cells were passaged at 80-90% confluence using Trypsin-EDTA (0.25 %)

**Cytotoxicity.** CT26 were plated in 96-well plates (1,250 cells/well) and incubated overnight. The media was then replaced with 200  $\mu$ l media with either PLGA or PTX-MB @ PLGA NPs at various concentrations. The highest concentration of the nanoparticles was 864  $\mu$ g mL<sup>-1</sup> (corresponding to 4000 nM PTX-MB released after 1 hour). The cells were incubated with the nanoparticle suspension for 48 hours. A resazurin assay was used to determine the cell viability.

***In vitro* inhibitory effect of PTX-MB.** The *in vitro* inhibitory effect of PTX-MB was tested with CT26 colon cancer cells. The cells were plated in 96-well plates (2,500 cells/well) and incubated overnight. PTX-MB, paclitaxel, and methylene blue were added at different concentrations to cell media with 0.1% DMSO to assist the dissolution of the drugs. Live cells in media without DMSO and dead cells were also included as controls. These cells were incubated 48 hours followed by a Resazurin assay (Sigma).

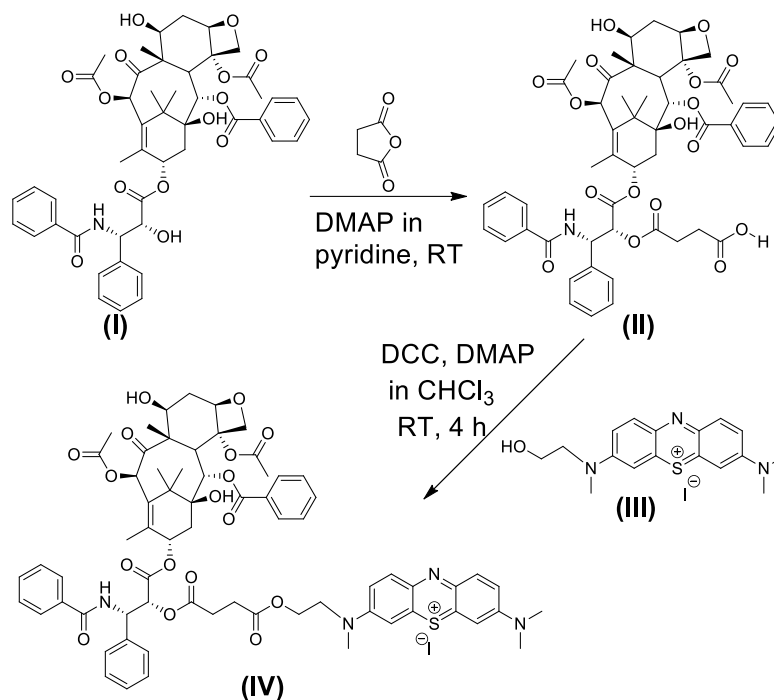
**Photoacoustic imaging of *in vivo* drug release.** Mice were divided into two groups (control and experimental groups). The PTX-MB @ PLGA NPs (25 mg mL<sup>-1</sup>) and blank PLGA NPs (25 mg mL<sup>-1</sup>) were suspended in a mixture of matrigel, normal mice serum, and 1X PBS (50%, 10%, and 40% respectively). The nanoparticle suspension (100 μL) was subcutaneously injected in each of the mice of the experimental group. The photoacoustic image of the injected region on each of the mice were obtained at 2, 4, 6, 8, 10, and 12 hours with 690 nm excitation. Mice in the control set were injected with similarly prepared suspension containing blank PLGA NPs (100 μL, 25 mg mL<sup>-1</sup>). The 3D photoacoustic images were analyzed on Image J to obtain the intensity. Statistical analysis used t-tests via Microsoft Excel.

***In vivo* activity.** Mice were divided into five groups and 250K CT26 cells in 50% matrigel and PBS were injected in each mouse (day 1). On days 3, 5, and 7, the animals in each respective group were injected with the following: PTX-MB @ PLGA NPs (10 mg/kg PTX equivalent), PTX (10 mg Kg<sup>-1</sup>), PBS (100 μL), PTX (20 mg/kg), and PLGA nanoparticles (100 μL of 25 mg mL<sup>-1</sup>). Animals were injected with luciferin (150 mg/kg in PBS) immediately prior to imaging and were imaged on days 3, 5, 7, 11, and 14 to measure tumor volume.

### 5.3 Results and Discussion

We designed an imaging-based drug release monitoring strategy because direct monitoring of drug release and drug distribution release remains a challenge.<sup>256-257, 260, 269</sup> Therefore, a broadly applicable strategy for monitoring drug release and local distribution is highly desirable. We adopted a covalent labeling strategy where the methylene blue (MB) is linked to paclitaxel to form a photoacoustically active conjugate (PTX-MB). Using the redox property of the MB moiety in PTX-MB molecule, we chemically reduced it to a colorless, acoustically silent leuco form (PTX-

LMB) (no absorbance at 640 nm) and encapsulated it inside PLGA nanocarriers. Upon release from PLGA NPs, the PTX-LMB spontaneously oxidized to acoustically active (PTX-MB with strong absorbance at 640 nm) form.



**Scheme 5.1 Design and synthesis of paclitaxel-methylene blue conjugate (PTX-MB).** PTX-MB was synthesized through a three step synthesis. The crude product was purified by reverse phase HPLC and isolated as trifluoroacetate salt. The overall isolated yield after HPLC was 13.6%. Inset is a sample of PTX-MB purified by HPLC.

### 5.3.1 Synthesis of PTX-MB

The synthesis of PTX-MB is outlined in **Scheme 5.1**. We used the FDA-approved methylene blue to label paclitaxel.<sup>270-271</sup> The 2' hydroxy group on the paclitaxel molecule is reactive and is a versatile moiety for functionalization.<sup>264, 272</sup> A reaction of paclitaxel with succinic anhydride in dry pyridine resulted in the hemisuccinate form of paclitaxel (II) (see LC-MS in **Figure S1** and **S2**).<sup>264</sup> The functionalization of either 2' or 7 hydroxy groups in paclitaxel did not

affect the cytotoxicity significantly.<sup>272-273</sup> Hence, the functionalization of 2' or/and 7 hydroxy groups in paclitaxel is used to tag a target ligand and to make water-soluble derivatives.

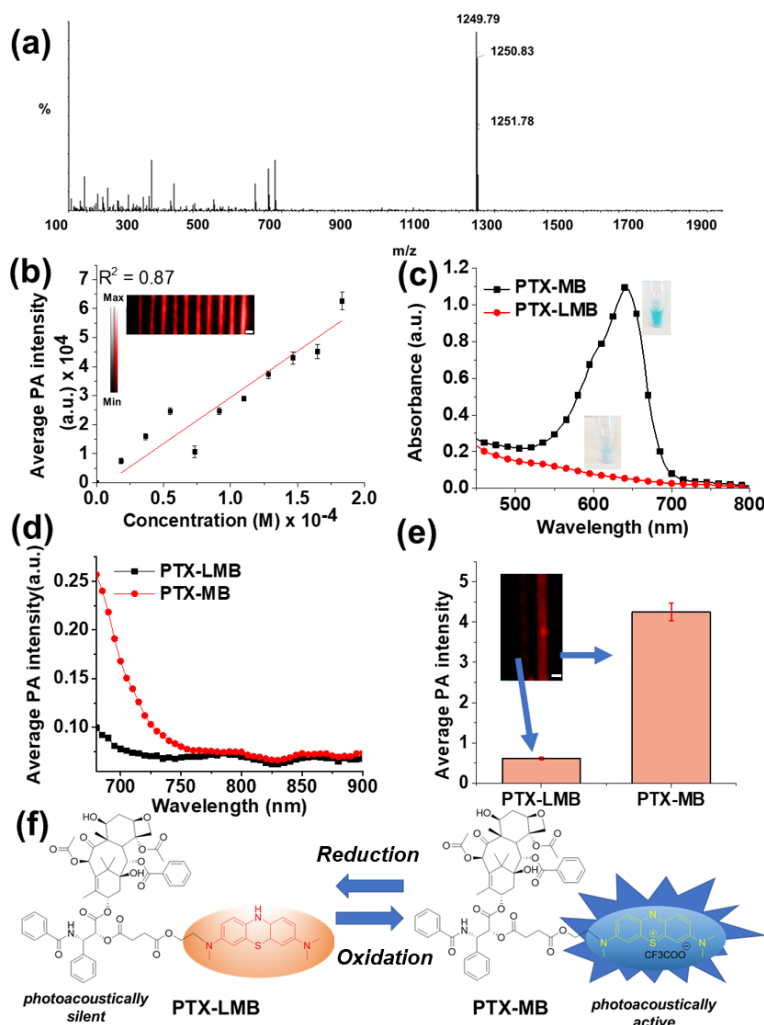


**Figure 5.1. Structural, spectral and photoacoustic characterization of PTX-MB.** (a) Mass spectrum of HPLC purified sample of PTX-MB shows the molecular ion peak ( $m/z = 1249.79$ ,  $C_{88}H_{73}N_4O_{17}S^+$ ). (b) The photoacoustic signal intensity ( $\lambda_{exc} = 640$  nm) shows a linear relationship with concentration of PTX-MB ( $4.91 \times 10^{-5}$  to  $4.91 \times 10^{-6}$  mil  $L^{-1}$  in PBS containing 20% v/v mice serum,  $R^2 = 0.87$ ). (c) The absorbance spectrum of PTX-MB (black square) and PTX-LMB (red circle) ( $7.3 \times 10^{-5}$  M in PBS with 20% v/v mice serum) shows approximately 20-fold difference in absorbance at 640 nm. Inset in (c) shows photos of  $7.3 \times 10^{-5}$  M solutions of PTX-MB (blue) and PTX-LMB (faint blue). (d) The photoacoustic spectra shows an increase in photoacoustic intensity in the PTX-MB spectrum from 680 – 760 nm. (e) Photoacoustic imaging of PTX-MB and PTX-LMB solutions ( $7.3 \times 10^{-5}$  M in PBS with 20% mice serum) shows a 6.88-fold increase of PTX-MB at 680 nm. The inset in (e) is the photoacoustic image of a phantom. (f) The illustration shows the redox switching between PTX-MB and PTX-LMB leading to photoacoustic signal. Scale bars = 2 mm.

We synthesized PTX-MB through the ester formation between compounds (II) and (III).<sup>265</sup> The yield of crude product before HPLC purification was found to be 53.8% (**Figure S5 & S6**). After reverse phase HPLC purification, a purity of 93.6% was achieved and PTX-MB was isolated as trichloroacetate salt with isolated yield of 13.6% (see **Figure S7 & S8**).

The structure of the PTX-MB was confirmed by <sup>1</sup>H NMR and ESI-MS. The ESI-MS spectrum showed a distinct peak at 1249.79 corresponding to the cationic part of PTX-MB (corresponding to C<sub>88</sub>H<sub>73</sub>N<sub>4</sub>O<sub>17</sub>S<sup>+</sup>) (**Figure 5.1(a)**). The maximum solubility of PTX-MB in 20% v/v mice serum (in PBS) is 4.18 x 10<sup>-5</sup> mol L<sup>-1</sup>. A calibration of absorbance of PTX-MB (at 640 nm) versus the concentration in chloroform and PBS with 20% v/v mouse serum was used for this purpose (**Figure S9**). Then we confirmed that the photoacoustic intensity was directly proportional to the concentration of PTX-MB in 20 % v/v mouse serum (in PBS) (**Figure 5.1(b)**).

### 5.3.2 Optical and acoustic characterization of PTX-MB

Methylene blue is known to undergo a redox reaction to transform between the oxidized methylene blue (MB,  $\lambda_{\text{max}} = 640$  nm, photoacoustically active) form and reduced leuco methylene blue form (LMB,  $\lambda_{\text{max}} = 256$  nm, photoacoustically silent) under ambient conditions.<sup>262-263</sup> MB dissolved in 1x PBS at room temperature can be reduced by a wide range of reducing agents.<sup>274-275</sup> This is attributed to the reduction of the sulfur atom in the phenothiazonium ring. A similar property is expected in MB moiety of PTX-MB. We found that 7.3x10<sup>-5</sup> M PTX-MB is reduced completely by 3.2x10<sup>-2</sup> M DTT in presence of 0.05 % v/v trimethylamine according to absorbance spectra (**Figure 5.2(c)**). At 7.3x10<sup>-5</sup> M concentration, the photoacoustic contrast ( $\lambda_{\text{exc}} = 690$  nm) between PTX-MB and PTX-LMB (formed using 3.2x10<sup>-2</sup> M DTT) was 6.88 (**Figure 5.2 (d) & (e)**). The redox switching of PTX-MB to PTX-LMB is illustrated in **Figure 5.1(f)**.

### 5.3.3 Nanoparticle Synthesis and Characterization

Next, we prepared and characterized PTX-MB @ PLGA NPs. Previous studies showed the leuco form of methylene blue was stable inside a polymer matrix due to absence of oxygen within the matrix.<sup>276</sup> We reacted PTX-MB with DTT in chloroform containing PLGA and encapsulated the PTX-LMB in PLGA NPs by emulsification. DTT reduces the PTX-MB to PTX-LMB in the chloroform medium and then is solubilized in aqueous medium. DTT can also be removed completely after reduction and encapsulation of PTX-MB in PLGA NPs due to its higher solubility of DTT in water (50 mg mL<sup>-1</sup>) than chloroform (10 mg mL<sup>-1</sup>).<sup>274</sup> Thus, DTT can be easily removed during particle synthesis and washing. During the particle synthesis, a 60 mM aqueous solution of ascorbic acid (in PBS) purged with argon was used as aqueous medium to prevent spontaneous oxidation of PTX-LMB. The particles were characterized for size distribution using SEM and TEM. The size range of the PTX-LMB loaded particles was determined to be ~50 nm according to TEM (**Figure 5.2 (a)**) and 100-200 nm according to SEM (**Figure 5.2(b)**). The difference of observed particle size between TEM and SEM is attributed to the different method of sample preparation and shrinking of pores in PLGA NPs under high vacuum in TEM.<sup>277-278</sup>

The PLGA nanoparticles with encapsulated PTX-LMB were lyophilized and found to contain 0.018 mg (13.3 nanomol) of PTX-MB in 1.0 mg of PLGA NPs. The PTX-LMB-loaded NPs were blue in color due to surface oxidation of PTX-LMB. However, dissolution of PTX-LMB loaded PLGA NPs in chloroform resulted in a colorless solution (no absorbance at 640 nm). When the solution was mixed with 100 mM potassium hexacyanoferrate (III), the solution turned dark blue with strong absorbance at 640 nm due to oxidation (**Figure 5.2(c)**). Using absorbance, the percentage of conjugate existing as PTX-LMB form inside PLGA NPs was calculated to be 94.82%. The color change was also observed even when the solution of PTX-LMB loaded PLGA

NPs (in chloroform) was exposed to air for at least 30 min. Thus, the release of PTX-LMB from particles can lead to spontaneous oxidation and turn-on photoacoustic signal.

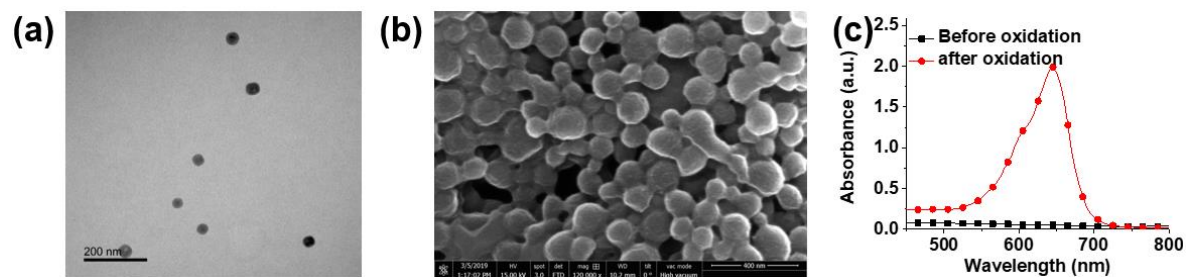


**Figure 5.2 Preparation and characterization of PLGA nanoparticles encapsulating PTX-LMB.** (a) TEM micrograph of PTX-LMB-loaded PLGA nanoparticles shows average diameter of 50 nm. (b) SEM micrograph of PTX-MB @ PLGA nanoparticles indicates a diameter of 100-200 nm (scale bar is 400 nm). The difference in size observed between TEM and SEM is due to shrinking of pores in PLGA NPs during TEM (c) Absorbance spectra of the freshly prepared solution of PTX-MB @ PLGA NPs ( $15 \text{ mg mL}^{-1}$ ) in chloroform (black squares) shows no absorption at 640 nm and the same solution absorbs strongly at 640 nm after oxidation with potassium hexacyanoferrate (III) (red circles). Using the absorbance data from (c), 94.82% of the loaded PTX-MB existed was remained as PTX-LMB.



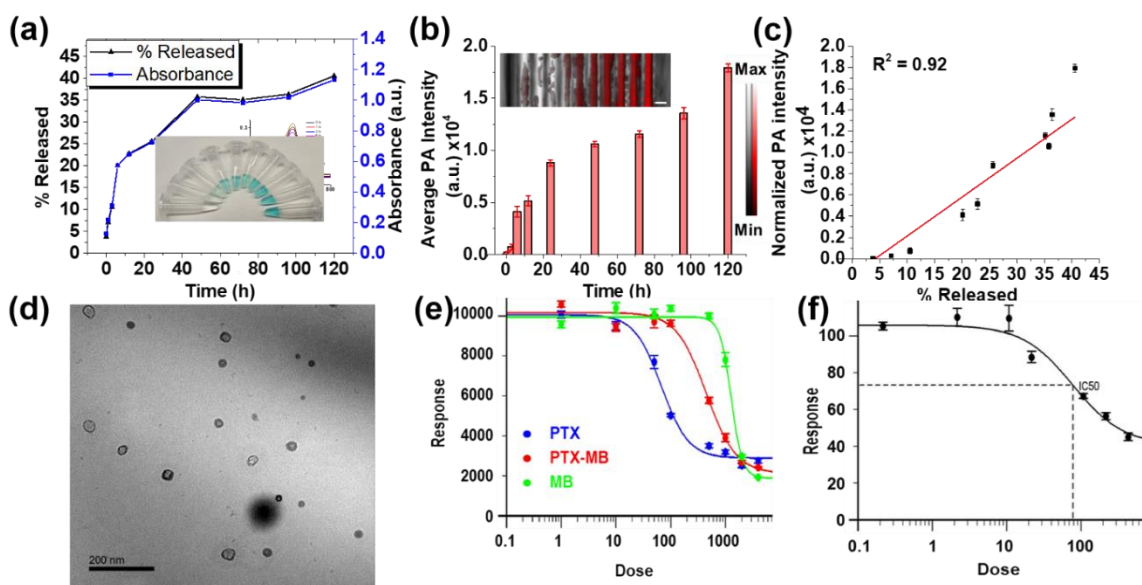


**Figure 5.3. In vitro drug release and cancer inhibitory activity of PTX-MB and PTX-MB @ PLGA NPs.** (a) The in vitro drug release profile of PTX-MB @ PLGA NPs ( $5.0 \text{ mg mL}^{-1}$  in 20% v/v mice serum in PBS) shows that 40.59% of PTX-LMB is released at the end of 120 h. The inset in panel (a) shows the photograph of aliquots under visible light. (b) The photoacoustic intensity of drug release aliquots show a 669.9-fold increase in signal after 120 h. Particles isolated from these aliquots did not show significant increase in photoacoustic signal (see Figure S3). Scale bar = 2 mm. (c) The photoacoustic signal is linearly related to the percentage of PTX-MB ( $R^2 = 0.92$ ). (d) The TEM image of particles collected after 120 h of drug release shows no change in size compared to as-prepared NPs shown in (a). (e) The in vitro activity of PTX-MB on CT26 colon cancer cells shows that the IC<sub>50</sub> of PTX, PTX-MB, and MB are 68, 447, and 1281 nM respectively. (f) Cancer inhibitory activity of PLGA NPs loaded with PTX-LMB shows an IC<sub>50</sub> of  $78 \text{ } \mu\text{g mL}^{-1}$  corresponding to 362 nM PTX-MB released after 1 hour of release. Error bars are the standard deviations of four replicates.

### 5.3.4 In vitro drug release and anticancer inhibitory activity

Next, we studied the release of PTX-MB from the carrier and the *in vitro* anticancer activity against CT26 cells. The PTX-LMB loaded PLGA NPs were studied for drug release in 20% v/v mice serum in PBS. The release profile showed an initial burst release followed by a more gradual release of PTX-LMB. We collected aliquots from 0-120 h of drug release; the absorbance showed an 8-fold increase at 640 nm while the corresponding photoacoustic signal showed an increase of 669.9-fold after 120 h corresponding to 40.59 % release (**Figure 5.3(a) & (b)**). The photoacoustic signal showed a linear increase with respect to the percentage drug released (**Figure 5.3(c)**). The

increased absorbance and photoacoustic signal are attributed to the release of PTX-LMB and its oxidation to PTX-MB.<sup>279-280</sup>

The PLGA NPs isolated from the aliquots of drug release did not show any significant change in photoacoustic signal. Thus, the signal increase is attributed to the released conjugate (see **Figure S10**). The total of 40.59% of the loaded drug was found to be released after 120 h.<sup>281</sup> The aliquot collected at 120 h did not show detectable amounts of DTT according to mass spectrometry (**Figure S12**). No significant change in particle size was observed in TEM after the release time of 120 h (**Figure 5.3(d)**).

PTX-MB displayed significant anticancer activity against CT26 colon cancer cells. The IC<sub>50</sub> values of paclitaxel (PTX) and PTX-MB were found to be 68 nM and 447 nM against CT26 cells. The reduced cancer inhibitory activity of PTX-MB is also observed in other paclitaxel conjugates. Next, PTX-LMB-loaded PLGA NPs were studied for cancer inhibition against CT26 cells. The IC<sub>50</sub> of PTX-LMB loaded PLGA NPs was 78  $\mu\text{g mL}^{-1}$ . The IC<sub>50</sub> of PTX-LMB loaded PLGA NPs corresponds to 362 nM PTX-MB released after 1 hour. The difference in IC<sub>50</sub> of released drug is attributed to the difference in media used during the *in vitro* drug release study.

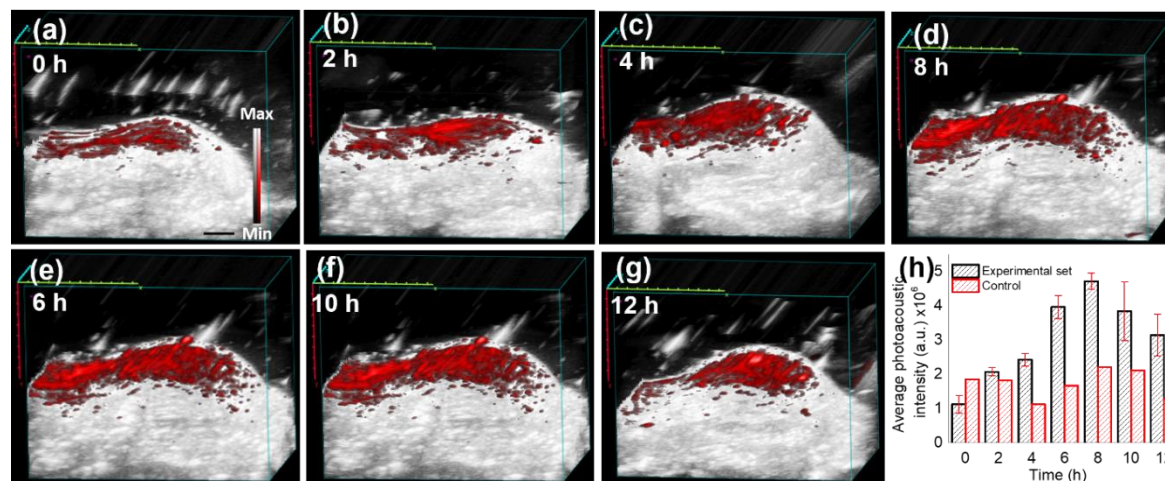


**Figure 5.4. Photoacoustic in vivo drug release monitoring in mice.** Images a-f show photoacoustic images of the subcutaneous injections of mice injected with the 25 mg mL<sup>-1</sup> dispersion of PLGA nanoparticles loaded with PTX-LMB. The experiment was performed in triplicate. (h) The photoacoustic signal intensity increased 168-649% from 0-8 h. Error bars represent the standard error. Scale bar = 2 mm.

### 5.3.5 *In vivo* drug release and anticancer activity

Finally we studied the release of PTX-MB from carrier and antitumor activity in murine models. We studied the PTX-MB @ PLGA NPs for *in vivo* release and anticancer activity. One set of the experimental group was subcutaneously injected with PTX-MB @ PLGA NPs (25 mg mL<sup>-1</sup>) and one control set of mice was subcutaneously injected was injected with blank PLGA NPs (25 mg mL<sup>-1</sup>) in a similar mixture of matrigel, PBS, and mice serum. The *in vivo* drug release was monitored using 3D photoacoustic images ( $\lambda_{exc}= 680$  nm). The images acquired in experimental and control groups (at 2, 4, 6, 8, 10 and 12 hours) showed obvious signal increase in the range of 168-649% between 0-8 h. After 8 hours the photoacoustic signal showed irregular change due the possible clearance of the released PTX-MB (**Figure 5.4 (a-h) and supporting information Figure S13**).

Finally, we used a murine cancer model to determine the efficacy of PTX-MB @ PLGA-DTT NPs. Mice with metastatic colon cancer were divided into five groups: PTX-MB @ PLGA-DTT (PTX-MB), PTX (10 mg/kg), PBS only, PTX (high, 20 mg/kg), and PLGA particle only. Mice treated with PTX-MB @ PLGA NPs (10 mg/kg equivalent paclitaxel) exhibited a 44.7% decrease in tumor radiance on Day 14 compared to mice treated with the PLGA nanoparticle alone (**Figure 5.5(a) & (b)**). Additionally, mice treated with PTX-MB encapsulated in PLGA-DTT NPs exhibited no significant weight loss or observable behavioral changes from treatment. One of the mice receiving PTX (high) exhibited high weight loss >10%, possibly due to toxic effects from a high dose of PTX (20 mg/kg). Fonseca *et al.* suggested that paclitaxel encapsulated nanoparticles caused a reduction in side effects and toxicity due to improved tissue distribution and pharmacokinetics<sup>282</sup>. Additionally, a previous study showed that a dose of 32.5 mg/kg of paclitaxel administered in 3 consecutive days caused 100% mortality in a murine model<sup>283</sup> consistent with our findings that a high dosage of paclitaxel can cause adverse side effects such as weight loss.

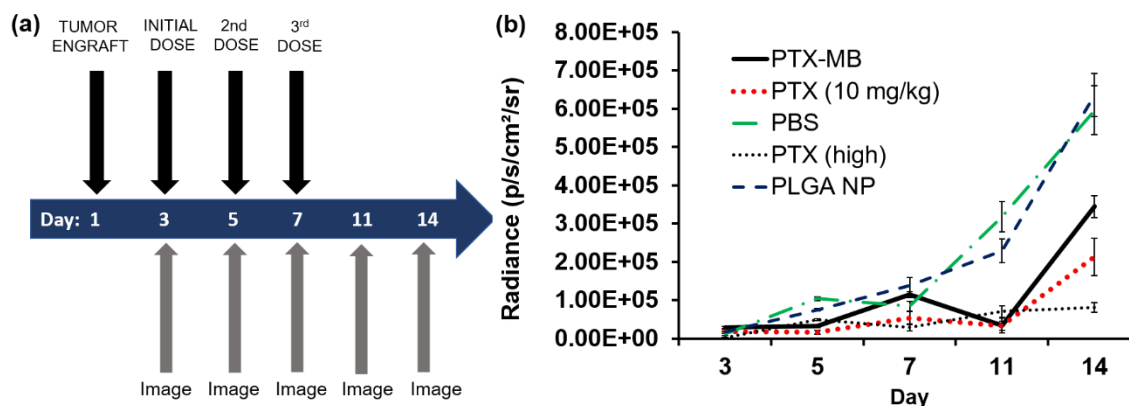


**Figure 5.5. *In vivo* efficacy of PTX-MB @ PLGA NPs.** (a) Nu/nu mice were divided into 5 groups (n=5). 250,000 luminescent CT-26 cells were injected IP on Day 1 in all mice. (a) The experimental illustration shows the schematic. Each mouse received the following doses IP on days 3, 5, and 7: PTX-MB @ PLGA NPs (PTX-MB) injection, PTX (10 mg/kg), PBS only, PTX (10 mg/kg), PTX (high, 20 mg/kg), and PLGA particle only. (b) The tumor radiance plotted against time (days) shows that mice treated with PTX-MB @ PLGA NPs (10 mg/kg equivalent Paclitaxel) exhibited a 44.7% decrease in tumor radiance on Day 14 compared to mice treated with the blank PLGA NPs. Error bars represent the standard error within treatment groups.

## 5.4 Conclusion

We developed a photoacoustically-activatable probe for drug release monitoring based on the blue-bottle reaction of methylene blue. Furthermore, we demonstrated the utility of the nanodrug formulation in live mouse models. In contrast to the previous reports, this strategy uses a direct photoacoustic increase from the drug tagged with an acoustically activatable chromophore.<sup>256, 260, 269</sup> The conjugated paclitaxel as well as the nanoparticle formulation with paclitaxel exhibits *in vitro* and *in vivo* cancer inhibitory effects. This approach is novel for two reasons. First, this approach of covalently conjugating an activatable photoacoustic probe can be used in different drug molecules with different chemistry. Second, the absorbance of the tagged chromophore can be changed to increase the depth of imaging using photoacoustic technique by covalent modification of the chromophore.<sup>284-285</sup> The phenothiazine-based chromophores have good photostability and can be dependable contrast agents in imaging against photobleaching and

loss of signal.<sup>285</sup> This is a powerful tool to monitor the location and concentration of drugs as well as insight on their status relative to nanocarriers.

## 5.5 Acknowledgements

J.E.L. acknowledges funding from the National Institutes of Health (NIH) Institutional National Research Service Award T32 CA153915, Cancer Researchers in Nanotechnology (Zhang). J.V.J. acknowledges funding from the NIH (Grants R00 HL117048 and DP2 HL137187) and infrastructure from Grants S10 OD021821 and S10 OD023555. The transmission electron micrographs were taken in the Cellular and Molecular Medicine Electron microscopy core facility which is supported in part by National Institutes of Health Award number S10 OD023527. This work was performed, in part, at the San Diego Nanotechnology Infrastructure of UCSD, a member of the National Nanotechnology Coordinated Infrastructure, which is supported by the National Science Foundation (Grant ECCS-1542148). The *in vivo* imaging studies using the IVIS system were conducted at the UCSD Screening Core. The authors would like to thank Nicole Steinmetz, PhD and Chao Wang, PhD for their gracious supply of CT26-Luc cells.

Chapter 5, in full, is currently being prepared for submission for publication of the material, AnanthaKrishnan Soundaram Jeevarathinam, Lemaster, Jeanne E., Fang Chen, Eric Zhao, and Jesse V. Jokerst. The dissertation author was the co-first author of this paper.

## 5.6 Appendix

### Synthesis of key intermediates.

PTX-COOH was synthesized according to the previously reported procedures.<sup>264</sup> In a typical synthesis of (PTX-COOH), Paclitaxel ( M.W. 853.90 g mol<sup>-1</sup>; 100.0 mg; 1.17x10<sup>-4</sup> mol), 4-dimethylaminopyridine (M.W., 122.16 g mol<sup>-1</sup>; 23.6 mg; 1.93x10<sup>-4</sup> mol) and of succinic anhydride (M.W., 100.07 g mol<sup>-1</sup>; 40.9 mg; 4.09x10<sup>-4</sup> mol) were placed under nitrogen in a round bottomed flask. Then, dry pyridine (3 mL) was added to dissolve the above reactants and the solution was stirred for 3 hours at room temperature. After 3 hours, anhydrous dichloromethane

(12 ml) was added. The combined solution was washed with 1 M HCl (3 x 12 ml) and with deionized water (3 x 12 ml). The aqueous phase was again washed with dichloromethane (10 ml). The combined organic phase was evaporated under vacuum in a rotary evaporator. The resulting crude 2'-succinimidyl paclitaxel (II) (PTX-COOH) was used without further purification. The product was isolated as colorless powder in 65 % isolated yield and purity of the sample was found to be 99.6%. MS (LC-ESI)  $m/z$   $[M+H]^+$  calcd for  $C_{51}H_{56}NO_{17}$  954.08; found 954.08 (LC-MS data is shown in Figure S1 & S2).

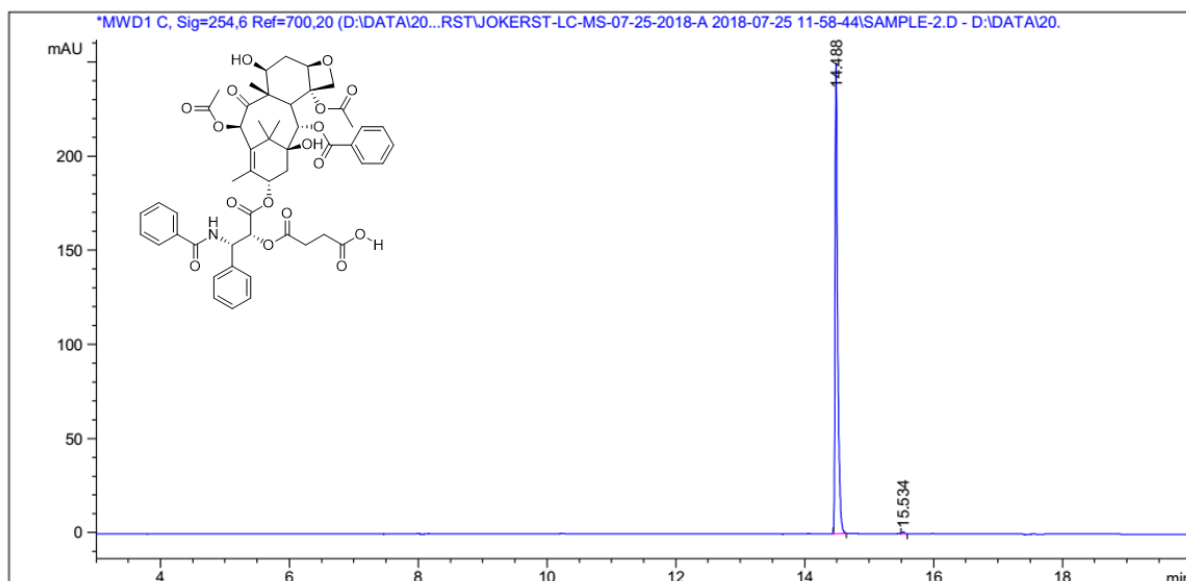


**Figure S1.** Liquid chromatography trace from the LC-MS analysis of (II). Retention time, 14.48 min with 99.6 % purity.



Sample-2 #598-603 RT: 14.45-14.56 AV: 6 SB: 6 14.29-14.41 NL: 1.41E7  
T: + c ESI Full ms [200.00-1800.00]

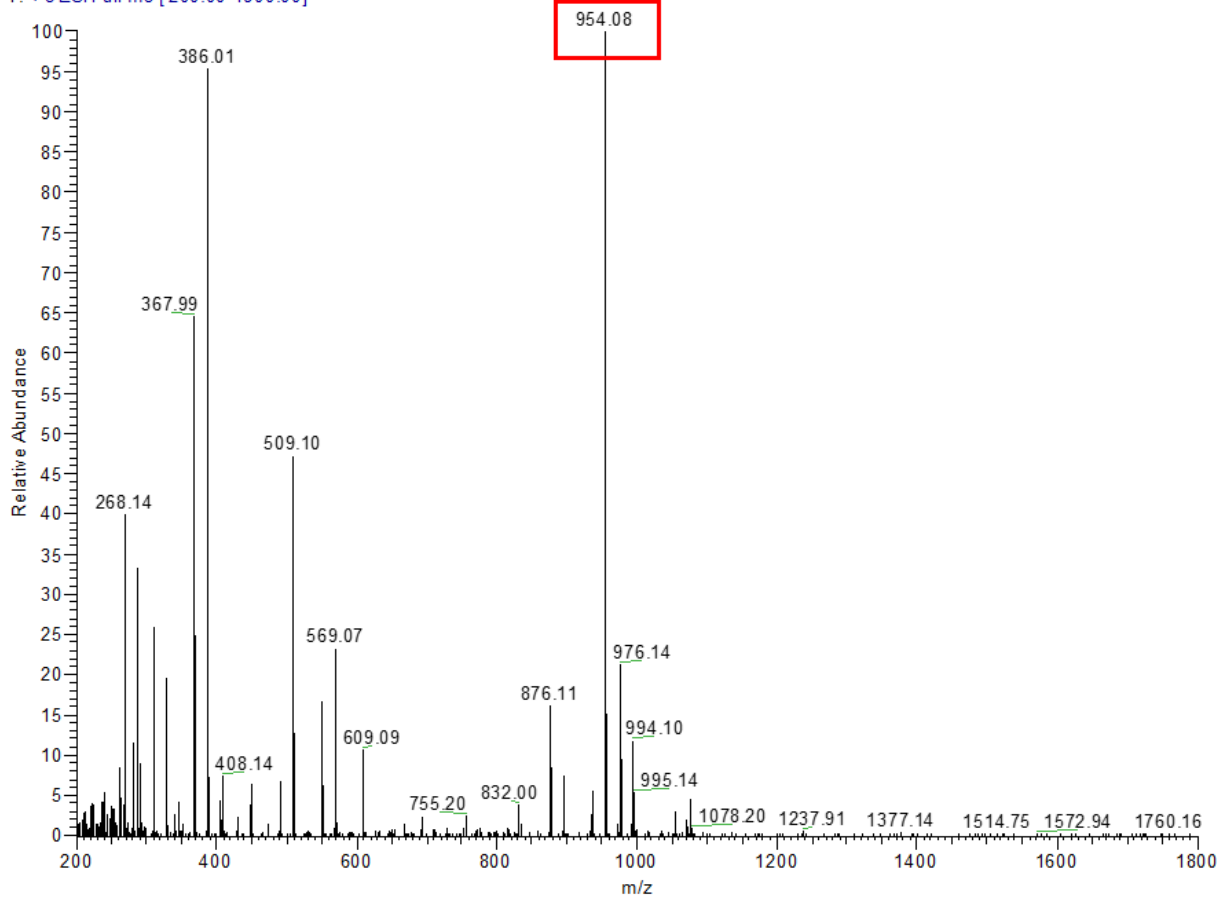


**Figure S2.** Mass spectrum of the sample of (II) from the LC-MS analysis corresponding to **Figure S1**.

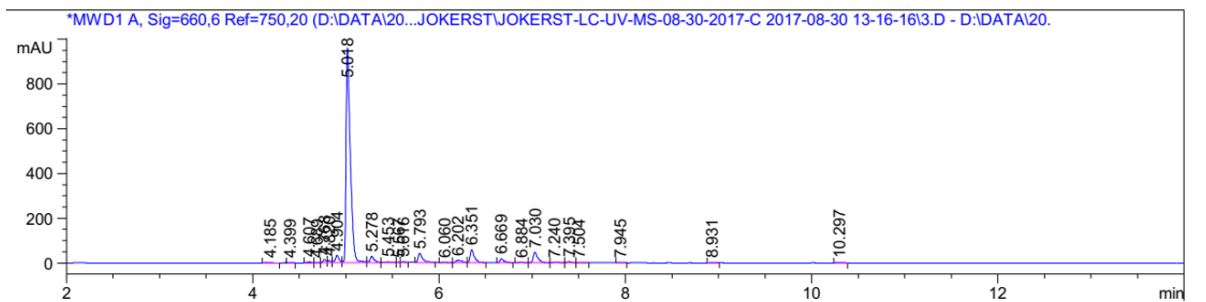


**Figure S3.** Liquid chromatography trace from the LC-MS analysis of dye (III). Retention time, 5.018 min with 74.6 % purity.

1-b #310-314 RT: 5.01-5.07 AV: 5 SB: 3 4.94-4.97 NL: 3.63E7  
T: + c ESI Full ms [ 100.00-900.00]

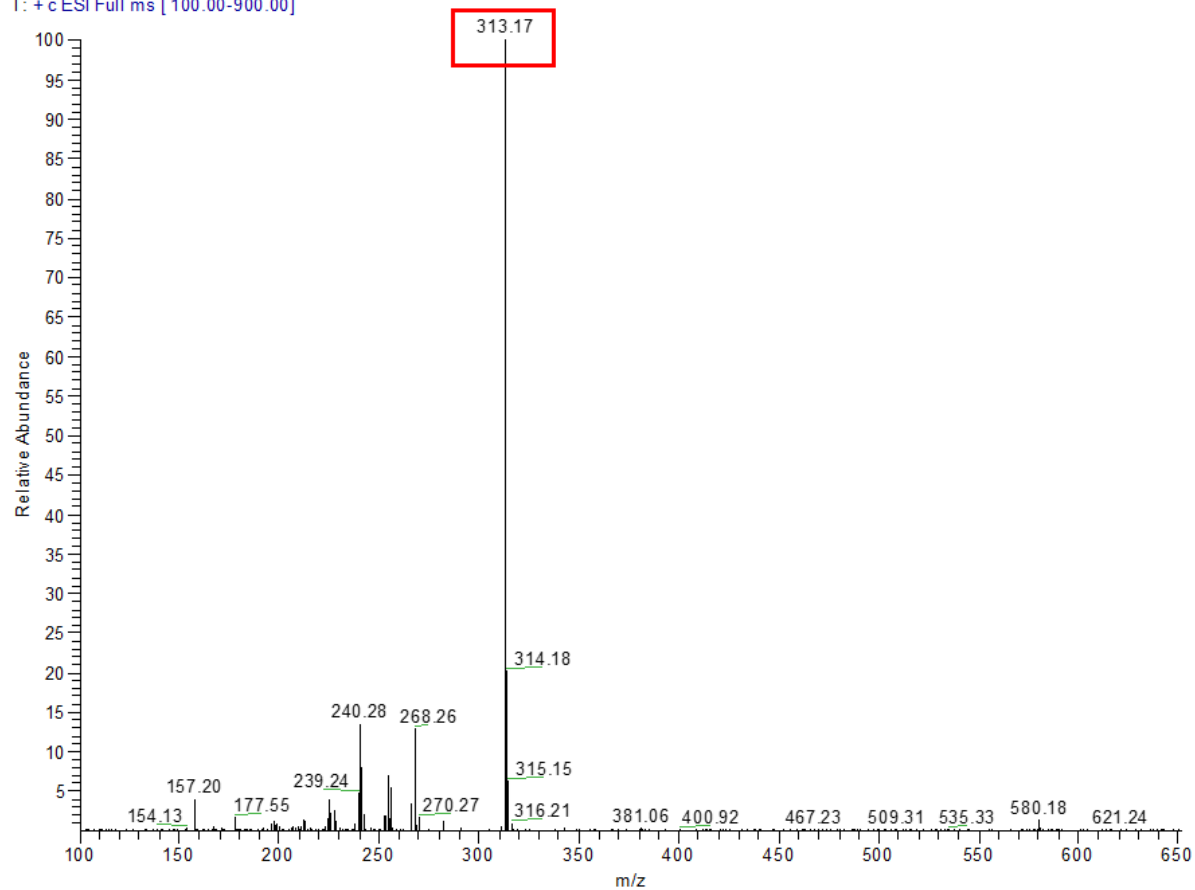


**Figure S4.** Mass spectrum from LC-MS analysis of dye (III) corresponding to **Figure S3**.

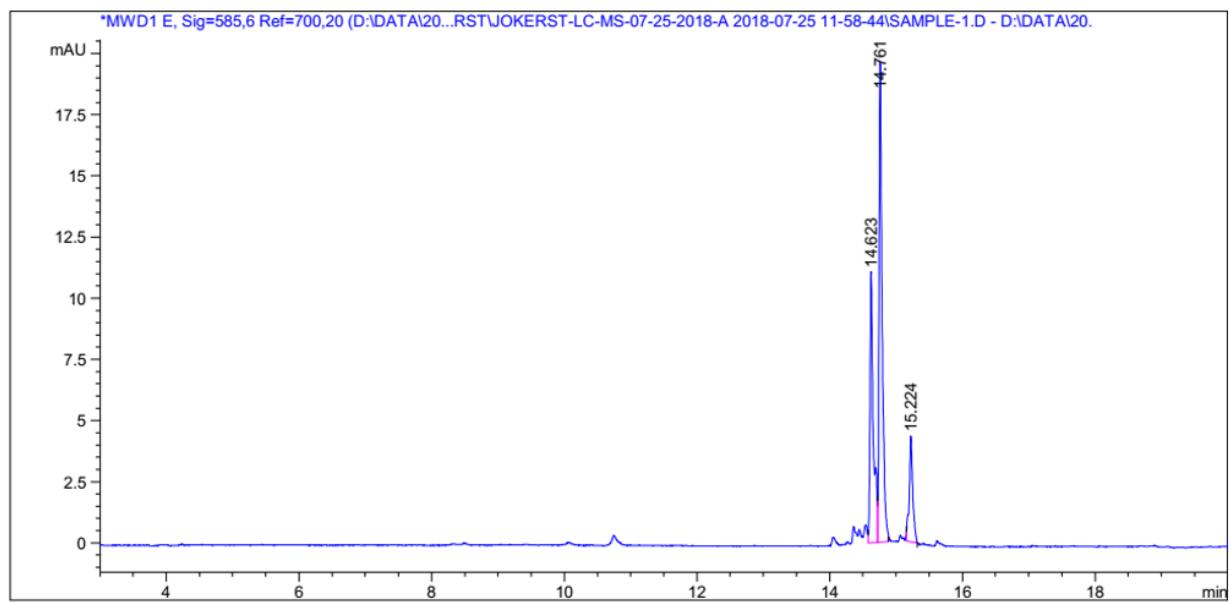


**Figure S5.** Liquid chromatogram of PTX-MB from LC-MS analysis of crude sample of PTX-MB obtained from reaction mixture corresponding to Figure 3S. Retention time is 14.78 min with an overall yield of 53.8 %.

Sample-1 #612-614 RT: 14.78-14.82 AV: 3 SB: 3 14.41-14.46 NL: 2.62E8  
T: + c ESI Full ms [200.00-1800.00]

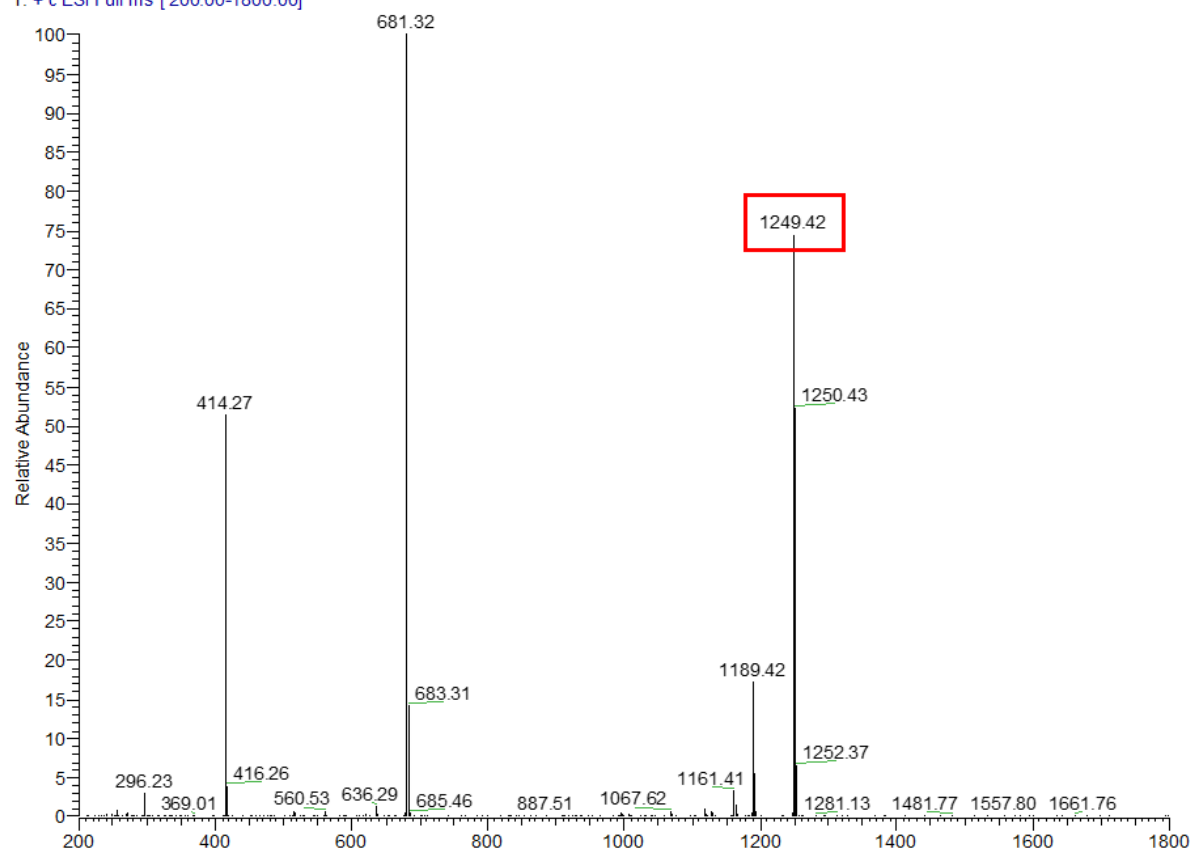


**Figure S6.** Mass spectrum from the LC-MS analysis of crude sample of PTX-MB. The mass spectrum corresponds to the peak with retention time of 14.78 min in **Figure 5S**.

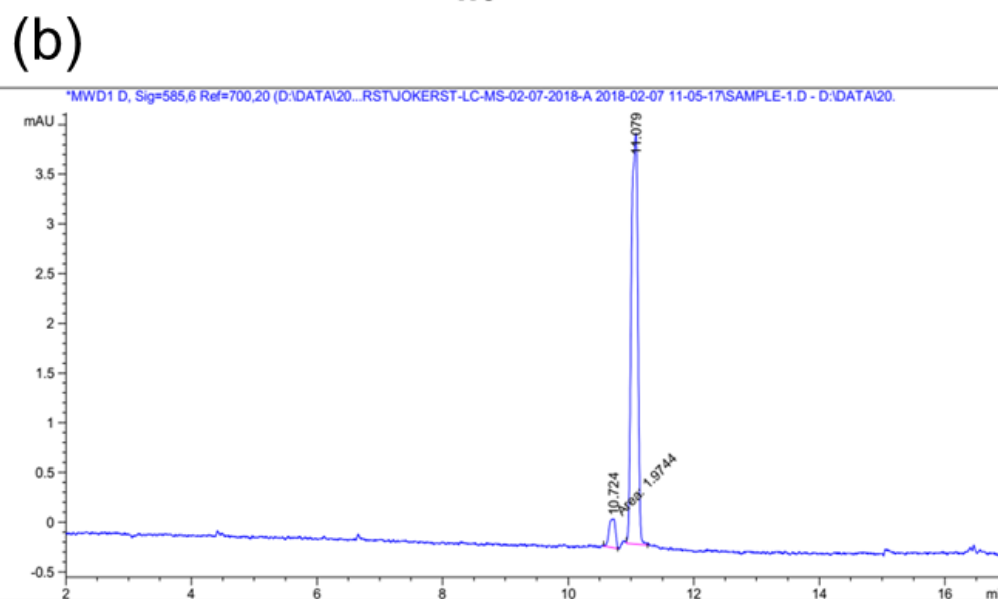
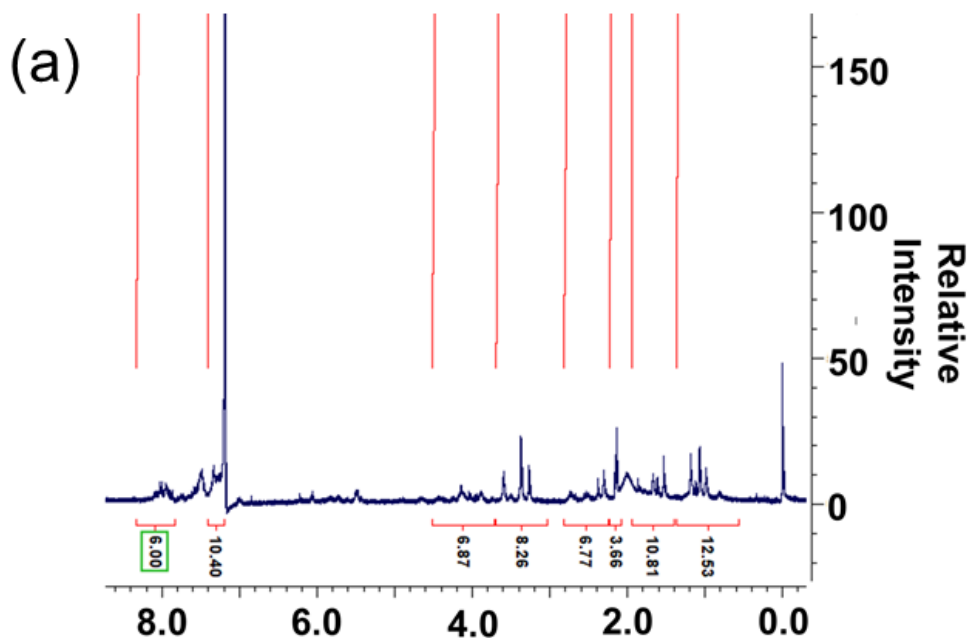


**Figure S7. (a) NMR spectrum of PTX-MB purified by HPLC . (b) Liquid chromatogram of PTX-MB after purification by reverse phase HPLC with a mobile phase gradient of 30 -60 % water in acetonitrile with 0.01 %v/v of trifluoroacetic acid. Retention time is 11.0 min with purity of 93.6%. Compound was isolated as trifluoroacetate salt.**

Sample-1#484-492 RT: 10.98-11.14 AV: 9 SB: 7 10.41-10.55 NL: 4.00E8  
T: + c ESI Full ms [ 300.00-1800.00]

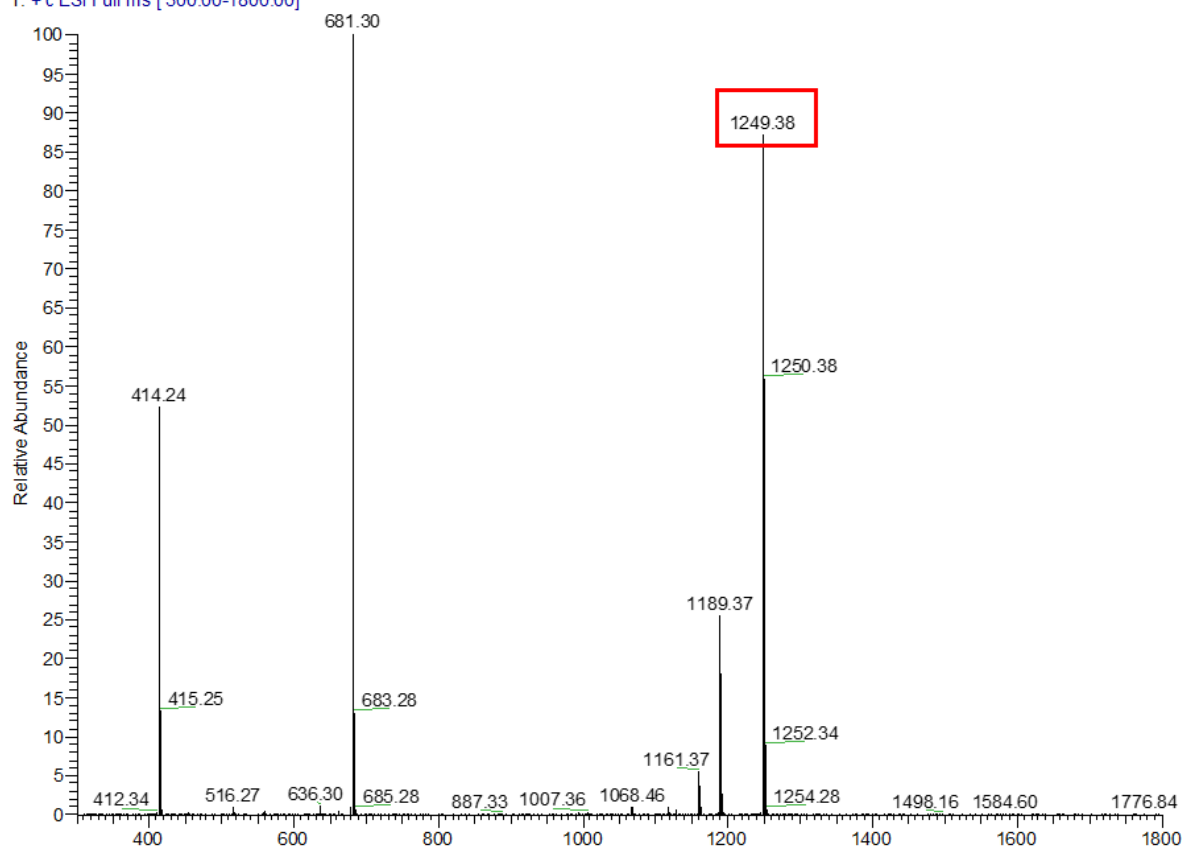


**Figure S8.** Mass spectrum of PTX-MB after purification by reverse phase HPLC. The spectrum corresponds to the peak with retention time of 11.0 min in **Figure 7S**.

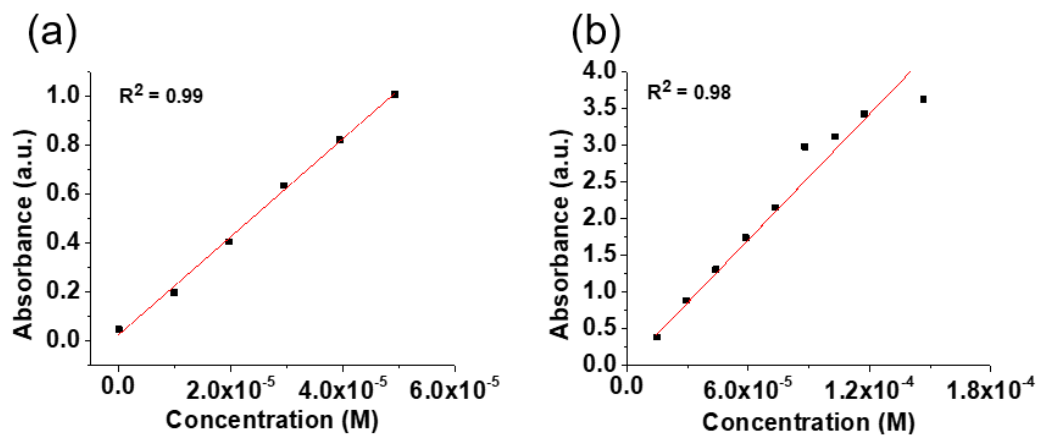
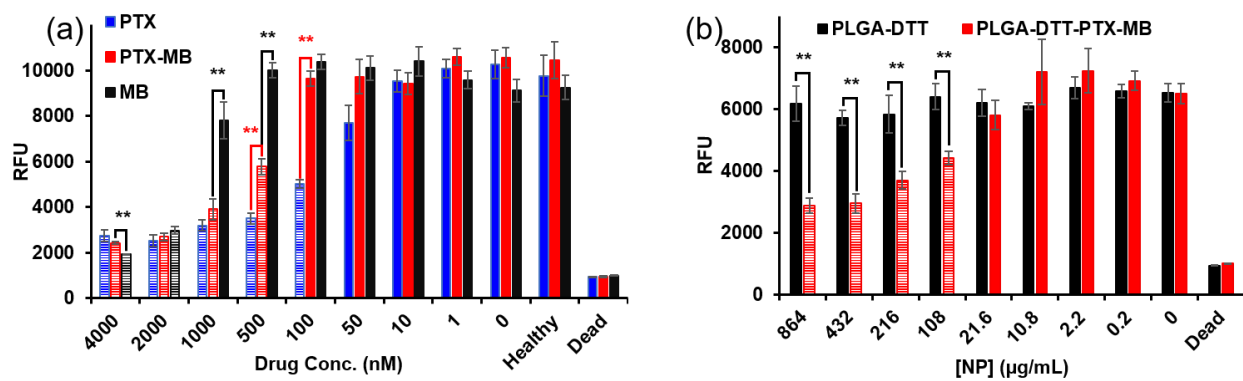


**Figure S9.** (a) Calibration of absorbance of PTX-MB with its concentration in PBS medium containing 20 % v/v normal mouse serum.

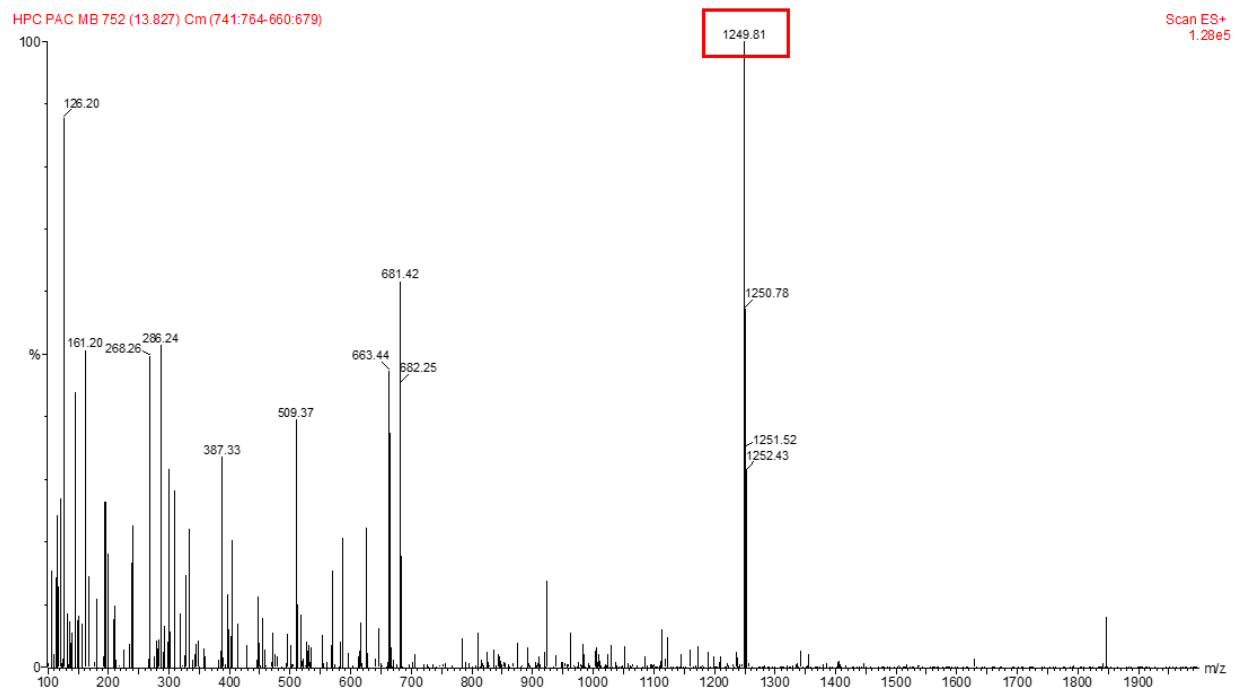




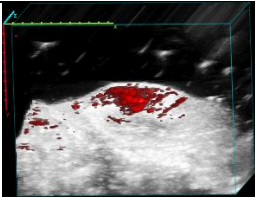
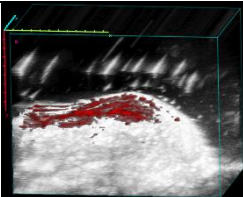
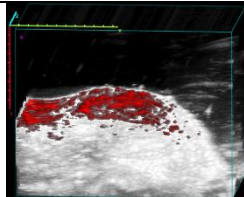
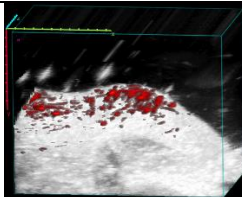
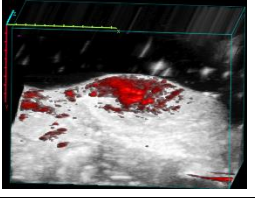
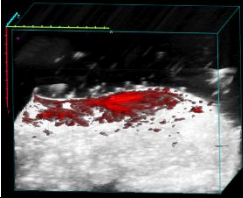
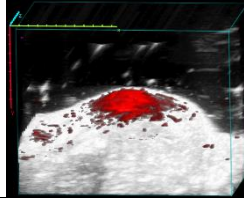
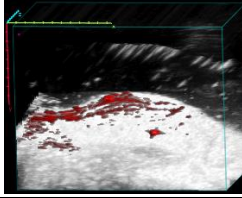
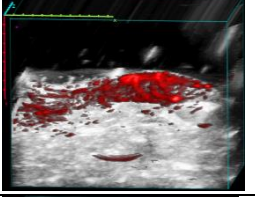
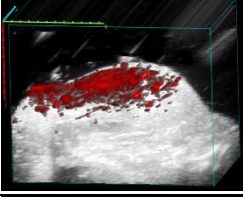
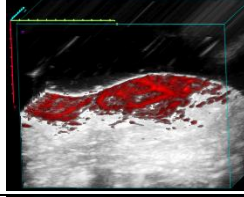
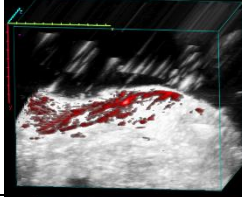
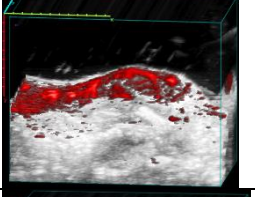
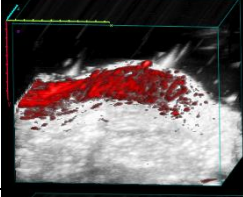
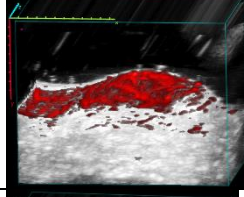
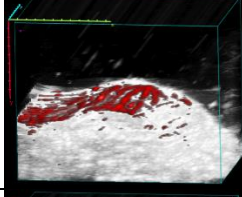
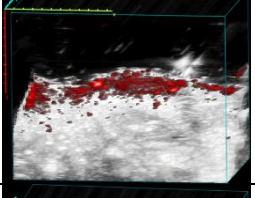
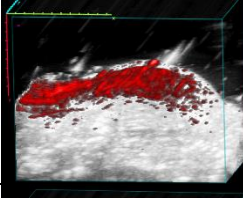
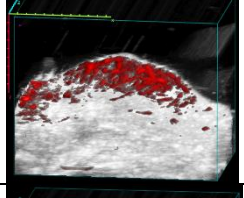
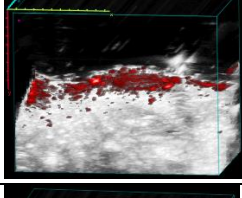
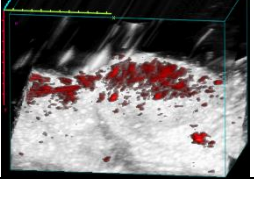
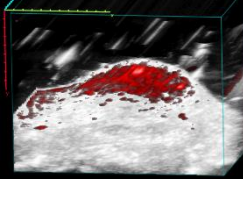
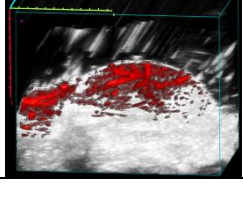
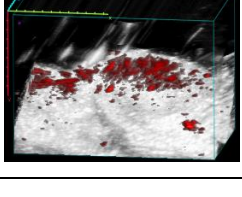
**Figure S10.** (a) Absorbance of supernatants collected during the drug release study of PLGA NPs loaded with PTX-LMB in PBS with 20 % mouse serum at 0, 1, 3, 6, 12, 24,48, 72, 96, and 120 hours. (b) photograph of the aliquots collected corresponding to the absorbance in (a). (c) the particles isolated from each aliquots were dispersed in 1% agarose to avoid precipitation (leading to small variations in photoacoustic signal) and 3D image of the dispersions were acquired after the allowing the dispersion to solidify. (c) shows that the photoacoustic intensity of the isolated particles did not follow a specific trend. This is in contrast to the photoacoustic signal of the supernatants of the aliquots.



**Figure S11.** (a) Dose-response curve of the drugs. The half maximal inhibitory concentration (IC<sub>50</sub>) of PTX, PTX-MB, and MB are 68, 447, and 1281 nM respectively. Striped columns have a  $p < 0.001$  compared to the group without drug (0 nM). S:  $p < 0.001$  (two tail, homoscedastic student t-test). (b) Dose-response curve of the PLGA-DTT-PTX-MB. The half maximal inhibitory concentration (IC<sub>50</sub>) of PLGA-DTT-PTX-MB is 78  $\mu\text{g/mL}$  or 362 nM PTX-MB after one-hour release. Striped columns have a  $p < 0.001$  compared to the group without nanoparticles (0  $\mu\text{g/mL}$ ). S:  $p < 0.001$  (two tail, homoscedastic student t-test).



**Figure S12.** ESI-mass spectrum of PTX-MB extracted from the supernatant of the aliquot collected from drug release study at 120 h. No detectable amounts of DTT was found in the aliquot.

Time points (h)	Experimental set 1	Experimental set 2	Experimental set 3	Control set
0				
2				
4				
6				
8				
10				

**Figure S13.** Photoacoustic 3D images of experimental and control sets of mice at different time points obtained from the in-vivo drug release studies.

## CHAPTER 6: CONCLUSION AND FUTURE DIRECTION

### 6.1 Translation of Nanoparticle-based Contrast Agents to Clinical Settings

The translation of nanoparticle-based photoacoustic imaging from laboratories to clinical settings is currently limited by toxicity concerns, poor signal, synthesis of NPs, and targeting of nanoparticles. There are active research programs using radio frequency, microwave, x-rays to produce acoustic signal<sup>286-288</sup>, i.e., thermoacoustic imaging. Magnetomotive ultrasound is another promising alternative that uses an external high-strength pulsed magnetic field to induce motion within magnetically labeled tissue; ultrasound is used to detect the induced internal tissue motion. In one example, this was used to discriminate between endocytosed iron oxide nanoparticles and extracellular nanoparticles via photoacoustic data as well as the concentration of each.<sup>289</sup> This approach also offers significant depth advantages. The challenge in each of these approaches is achieving sufficient signal and acoustic pressure differences to be detected with clinical transducers.

### 6.2 Hardware Advancements

Another approach to overcoming depth limitation is via the development of novel transducers. That is, rather than trying to make the signal stronger, these approaches take the detector closer to the signal. There are active research programs developing small, implantable, and even wearable photoacoustic transducers suitable for endoscopic, transrectal,<sup>290-291</sup> transvaginal,<sup>292</sup> or vascular imaging. These devices will complement novel contrast agents and could be used for applications other than imaging such as wearable sensors sensitive to drug levels. A third approach to increasing signal moves into the second NIR window (NIR II). This region is generally from 1000-1500 nm and offers even lower absorption and scatter (except from water).

Although this has thus far been primarily demonstrated for fluorescence imaging,<sup>293</sup> we suspect that photoacoustic imaging could take advantage of this region. It is likely that nanoparticles will play a key role in all three of these developments: sensitizers to the x-rays/RF, near infrared II contrast agents, or for use with novel transducers.

We will also likely continue to see theranostic applications that include imaging due to the effects on vasculature response, hemodynamics, local temperature<sup>69</sup>, and pH sensitivity.<sup>294</sup> In theranostics, the nanoparticle has both a therapeutic role (drug delivery, tumor ablation) and a diagnostic role (tumor margins, sub-typing). In one example, gold nanocages (AuNCs) encapsulated drugs and a phase-change material to load and release the drug in the presence of high intensity focused ultrasound—this allowed for site-specific delivery.<sup>295</sup> In another example, CuS nanoparticles were used for both photoacoustic imaging, enzyme-responsive drug therapy, and phototherapy—this combination therapy may be used as a multifunctional platform for cancer treatment.<sup>296</sup> Future examples may combine photoacoustic imaging with photothermal therapy. This has already been shown with Fe<sub>5</sub>C<sub>2</sub>-based nanoparticles<sup>297</sup> and is possible because of the different optical pulse sequences and wavelengths used in photoacoustic imaging versus photothermal therapy. Thus, this same nanoparticle could both image and ablate tumors. Although exciting, these combination approaches can be more challenging to clinically translate. Simpler materials are usually more easily approved by the FDA.

### **6.3 Future Direction in Nanoparticle Contrast Agent Development**

Nanoparticle contrast agents are useful for imaging applications because they have high signal, stable signal, or activatable signal. New persons in this field would be wise to work on the NIR II window for improved clinical translation or find collaborators developing novel

photoacoustic imaging equipment. Additionally, thermoacoustic and x-ray-based ultrasound are tools which can increase the depth of photoacoustic penetration and we suspect that nanoparticle contrast agents will continue to play an important role in these hybrid acoustic modalities.

The field of medicine is rapidly changing with advancements in cell therapy, contrast agents for imaging, and medical equipment. These developments will improve diagnostics and therapy as well as overall human health.

## REFERENCES

1. Marks, P.; Gottlieb, S., Balancing safety and innovation for cell-based regenerative medicine. *New England Journal of Medicine* **2018**, *378* (10), 954-959.
2. Piuze, N. S.; Ng, M.; Chughtai, M.; Khlopa, A.; Ng, K.; Mont, M. A.; Muschler, G. F., The stem-cell market for the treatment of knee osteoarthritis: a patient perspective. *The journal of knee surgery* **2018**, *31* (06), 551-556.
3. Lunn, J. S.; Sakowski, S. A.; Hur, J.; Feldman, E. L., Stem cell technology for neurodegenerative diseases. *Annals of neurology* **2011**, *70* (3), 353-361.
4. Wu, R.; Hu, X.; Wang, J. a., Concise review: Optimized strategies for stem cell-based therapy in myocardial repair: Clinical translatability and potential limitation. *Stem Cells* **2018**, *36* (4), 482-500.
5. Golchin, A.; Farahany, T. Z., Biological products: cellular therapy and FDA approved products. *Stem Cell Reviews and Reports* **2019**, *15* (2), 166-175.
6. Ankrum, J.; Karp, J. M., Mesenchymal stem cell therapy: Two steps forward, one step back. *Trends in molecular medicine* **2010**, *16* (5), 203-209.
7. Gu, E.; Chen, W.-Y.; Gu, J.; Burrige, P.; Wu, J. C., Molecular imaging of stem cells: tracking survival, biodistribution, tumorigenicity, and immunogenicity. *Theranostics* **2012**, *2* (4), 335.
8. James, M. L.; Gambhir, S. S., A molecular imaging primer: modalities, imaging agents, and applications. *Physiological Rev.* **2012**, *92* (2), 897-965.
9. Gogtay, N.; Sporn, A.; Clasen, L. S.; Nugent, T. F.; Greenstein, D.; Nicolson, R.; Giedd, J. N.; Lenane, M.; Gochman, P.; Evans, A., Comparison of progressive cortical gray matter loss in childhood-onset schizophrenia with that in childhood-onset atypical psychoses. *Archives of general psychiatry* **2004**, *61* (1), 17-22.
10. Wang, L. V.; Hu, S., Photoacoustic Tomography: In Vivo Imaging from Organelles to Organs. *Science* **2012**, *335* (6075), 1458-1462.
11. Castaneda, R. T.; Khurana, A.; Khan, R.; Daldrup-Link, H. E., Labeling stem cells with ferumoxytol, an FDA-approved iron oxide nanoparticle. *JoVE (Journal of Visualized Experiments)* **2011**, (57), e3482.
12. Homan, K.; Kim, S.; Chen, Y.-S.; Wang, B.; Mallidi, S.; Emelianov, S., Prospects of molecular photoacoustic imaging at 1064 nm wavelength. *Optics letters* **2010**, *35* (15), 2663-2665.
13. Cho, E. C.; Glaus, C.; Chen, J.; Welch, M. J.; Xia, Y., Inorganic nanoparticle-based contrast agents for molecular imaging. *Trends in molecular medicine* **2010**, *16* (12), 561-573.



14. Smith, A. M.; Mancini, M. C.; Nie, S., Bioimaging: Second window for in vivo imaging. *Nat Nanotechnol* **2009**, *4*, 710-711.
15. Jokerst, J. V.; Lobovkina, T.; Zare, R. N.; Gambhir, S. S., Nanoparticle PEGylation for imaging and therapy. *Nanomedicine* **2011**, *6* (4), 715-728.
16. Zackrisson, S.; van de Ven, S.; Gambhir, S., Light in and sound out: emerging translational strategies for photoacoustic imaging. *Cancer research* **2014**, *74* (4), 979-1004.
17. Kohl, Y.; Kaiser, C.; Bost, W.; Stracke, F.; Fournelle, M.; Wischke, C.; Thielecke, H.; Lendlein, A.; Kratz, K.; Lemor, R., Preparation and biological evaluation of multifunctional PLGA-nanoparticles designed for photoacoustic imaging. *Nanomedicine: Nanotechnology, Biology and Medicine* **2011**, *7* (2), 228-237.
18. Viator, J. A.; Gupta, S.; Goldschmidt, B. S.; Bhattacharyya, K.; Kannan, R.; Shukla, R.; Dale, P. S.; Boote, E.; Katti, K., Gold nanoparticle mediated detection of prostate cancer cells using photoacoustic flowmetry with optical reflectance. *Journal of biomedical nanotechnology* **2010**, *6* (2), 187-191.
19. Zhang, Y.; Hong, H.; Cai, W., Photoacoustic imaging. *Cold Spring Harbor Protocols* **2011**, *2011* (9), pdb. top065508.
20. Qin, C.; Cheng, K.; Chen, K.; Hu, X.; Liu, Y.; Lan, X.; Zhang, Y.; Liu, H.; Xu, Y.; Bu, L., Tyrosinase as a multifunctional reporter gene for Photoacoustic/MRI/PET triple modality molecular imaging. *Scientific reports* **2013**, *3*.
21. Liang, X.; Deng, Z.; Jing, L.; Li, X.; Dai, Z.; Li, C.; Huang, M., Prussian blue nanoparticles operate as a contrast agent for enhanced photoacoustic imaging. *Chemical Communications* **2013**, *49* (94), 11029-11031.
22. Zha, Z.; Deng, Z.; Li, Y.; Li, C.; Wang, J.; Wang, S.; Qu, E.; Dai, Z., Biocompatible polypyrrole nanoparticles as a novel organic photoacoustic contrast agent for deep tissue imaging. *Nanoscale* **2013**, *5* (10), 4462-4467.
23. Kim, S.; Chen, Y.-S.; Luke, G. P.; Emelianov, S. Y., In vivo three-dimensional spectroscopic photoacoustic imaging for monitoring nanoparticle delivery. *Biomedical optics express* **2011**, *2* (9), 2540-2550.
24. Thakor, A. S.; Jokerst, J. V.; Zavaleta, C. L.; Massoud, T. F.; Gambhir, S. S., Gold Nanoparticles: A Revival in Precious Metal Administration to Patients. *Nano Lett.* **2011**, *11* (10), 4029-4036.
25. Li, K.; Liu, B., Polymer-encapsulated organic nanoparticles for fluorescence and photoacoustic imaging. *Chemical Society Reviews* **2014**, *43* (18), 6570-6597.
26. Rengan, A. K.; Bukhari, A. B.; Pradhan, A.; Malhotra, R.; Banerjee, R.; Srivastava, R.; De, A., In Vivo Analysis of Biodegradable Liposome Gold Nanoparticles as Efficient Agents for Photothermal Therapy of Cancer. *Nano Lett.* **2015**, *15* (2), 842-848.

27. Link, S.; Burda, C.; Nikoobakht, B.; El-Sayed, M., Laser-induced shape changes of colloidal gold nanorods using femtosecond and nanosecond laser pulses. *The Journal of Physical Chemistry B* **2000**, *104* (26), 6152-6163.
28. Nam, S. Y.; Ricles, L. M.; Suggs, L. J.; Emelianov, S. Y., Nonlinear photoacoustic signal increase from endocytosis of gold nanoparticles. *Optics letters* **2012**, *37* (22), 4708-4710.
29. Galanzha, E. I.; Nedosekin, D. A.; Sarimollaoglu, M.; Orza, A. I.; Biris, A. S.; Verkhusha, V. V.; Zharov, V. P., Photoacoustic and photothermal cytometry using photoswitchable proteins and nanoparticles with ultrasharp resonances. *Journal of Biophotonics* **2015**, *8* (1-2), 81-93.
30. Tam, J. M.; Tam, J. O.; Murthy, A.; Ingram, D. R.; Ma, L. L.; Travis, K.; Johnston, K. P.; Sokolov, K. V., Controlled Assembly of Biodegradable Plasmonic Nanoclusters for Near-Infrared Imaging and Therapeutic Applications. *ACS Nano* **2010**, *4* (4), 2178-2184.
31. Yoon, S. J.; Mallidi, S.; Tam, J. M.; Tam, J. O.; Murthy, A.; Johnston, K. P.; Sokolov, K. V.; Emelianov, S. Y., Utility of biodegradable plasmonic nanoclusters in photoacoustic imaging. *Optics letters* **2010**, *35* (22), 3751-3753.
32. Pan, D.; Pramanik, M.; Senpan, A.; Allen, J. S.; Zhang, H.; Wickline, S. A.; Wang, L. V.; Lanza, G. M., Molecular photoacoustic imaging of angiogenesis with integrin-targeted gold nanobeacons. *The FASEB Journal* **2011**, *25* (3), 875-882.
33. Maji, S. K.; Sreejith, S.; Joseph, J.; Lin, M.; He, T.; Tong, Y.; Sun, H.; Yu, S. W. K.; Zhao, Y., Upconversion nanoparticles as a contrast agent for photoacoustic imaging in live mice. *Advanced Materials* **2014**, *26* (32), 5633-5638.
34. Pan, D.; Cai, X.; Yalaz, C.; Senpan, A.; Omanakuttan, K.; Wickline, S. A.; Wang, L. V.; Lanza, G. M., Photoacoustic sentinel lymph node imaging with self-assembled copper neodecanoate nanoparticles. *ACS nano* **2012**, *6* (2), 1260-1267.
35. Hsu, S.-W.; Ngo, C.; Tao, A. R., Tunable and Directional Plasmonic Coupling within Semiconductor Nanodisk Assemblies. *Nano Lett.* **2014**, *14* (5), 2372-2380.
36. Ku, G.; Zhou, M.; Song, S.; Huang, Q.; Hazle, J.; Li, C., Copper sulfide nanoparticles as a new class of photoacoustic contrast agent for deep tissue imaging at 1064 nm. *Acs Nano* **2012**, *6* (8), 7489-7496.
37. Zhang, Y.; Jeon, M.; Rich, L. J.; Hong, H.; Geng, J.; Zhang, Y.; Shi, S.; Barnhart, T. E.; Alexandridis, P.; Huizinga, J. D., Non-invasive multimodal functional imaging of the intestine with frozen micellar naphthalocyanines. *Nat Nanotechnol* **2014**, *9* (8), 631-638.
38. Cheng, Z.; Al Zaki, A.; Hui, J. Z.; Muzykantov, V. R.; Tsourkas, A., Multifunctional nanoparticles: cost versus benefit of adding targeting and imaging capabilities. *Science* **2012**, *338* (6109), 903-910.

39. Wu, L.; Cai, X.; Nelson, K.; Xing, W.; Xia, J.; Zhang, R.; Stacy, A. J.; Luderer, M.; Lanza, G. M.; Wang, L. V., A green synthesis of carbon nanoparticles from honey and their use in real-time photoacoustic imaging. *Nano research* **2013**, *6* (5), 312-325.
40. Jokerst, J. V.; Van de Sompel, D.; Bohndiek, S. E.; Gambhir, S. S., Cellulose nanoparticles are a biodegradable photoacoustic contrast agent for use in living mice. *Photoacoustics* **2014**, *2* (3), 119-127.
41. Fan, Q.; Cheng, K.; Hu, X.; Ma, X.; Zhang, R.; Yang, M.; Lu, X.; Xing, L.; Huang, W.; Gambhir, S. S., Transferring biomarker into molecular probe: melanin nanoparticle as a naturally active platform for multimodality imaging. *Journal of the American Chemical Society* **2014**, *136* (43), 15185-15194.
42. Pu, K.; Shuhendler, A. J.; Jokerst, J. V.; Mei, J.; Gambhir, S. S.; Bao, Z.; Rao, J., Semiconducting polymer nanoparticles as photoacoustic molecular imaging probes in living mice. *Nat Nano* **2014**, *9* (3), 233-239.
43. Ng, K. K.; Shakiba, M.; Huynh, E.; Weersink, R. A.; Roxin, Á.; Wilson, B. C.; Zheng, G., Stimuli-responsive photoacoustic nanoswitch for in vivo sensing applications. *ACS nano* **2014**, *8* (8), 8363-8373.
44. Lee, C.; Kim, J.; Zhang, Y.; Jeon, M.; Liu, C.; Song, L.; Lovell, J. F.; Kim, C., Dual-color photoacoustic lymph node imaging using nanoformulated naphthalocyanines. *Biomaterials* **2015**, *73*, 142-148.
45. Fan, Q.; Cheng, K.; Yang, Z.; Zhang, R.; Yang, M.; Hu, X.; Ma, X.; Bu, L.; Lu, X.; Xiong, X., Perylene-Diimide-Based Nanoparticles as Highly Efficient Photoacoustic Agents for Deep Brain Tumor Imaging in Living Mice. *Advanced Materials* **2015**, *27* (5), 843-847.
46. Ho, I.-T.; Sessler, J. L.; Gambhir, S. S.; Jokerst, J. V., Parts per billion detection of uranium with a porphyrinoid-containing nanoparticle and in vivo photoacoustic imaging. *Analyst* **2015**, *140* (11), 3731-3737.
47. Huynh, E.; Lovell, J. F.; Helfield, B. L.; Jeon, M.; Kim, C.; Goertz, D. E.; Wilson, B. C.; Zheng, G., Porphyrin shell microbubbles with intrinsic ultrasound and photoacoustic properties. *J Am Chem Soc* **2012**, *134* (40), 16464-16467.
48. Pu, K.; Shuhendler, A. J.; Jokerst, J. V.; Mei, J.; Gambhir, S. S.; Bao, Z.; Rao, J., Semiconducting polymer nanoparticles as photoacoustic molecular imaging probes in living mice. *Nat Nanotechnol* **2014**.
49. Rieffel, J.; Chitgupi, U.; Lovell, J. F., Recent Advances in Higher-Order, Multimodal, Biomedical Imaging Agents. *Small* **2015**, *11* (35), 4445-4461.
50. Jin, Y.; Li, Y.; Ma, X.; Zha, Z.; Shi, L.; Tian, J.; Dai, Z., Encapsulating tantalum oxide into polypyrrole nanoparticles for X-ray CT/photoacoustic bimodal imaging-guided photothermal ablation of cancer. *Biomaterials* **2014**, *35* (22), 5795-5804.

51. Kircher, M. F.; de la Zerda, A.; Jokerst, J. V.; Zavaleta, C. L.; Kempen, P. J.; Mittra, E.; Pitter, K.; Huang, R.; Campos, C.; Habte, F., A brain tumor molecular imaging strategy using a new triple-modality MRI-photoacoustic-Raman nanoparticle. *Nature medicine* **2012**, *18* (5), 829-834.
52. Mou, J.; Liu, C.; Li, P.; Chen, Y.; Xu, H.; Wei, C.; Song, L.; Shi, J.; Chen, H., A facile synthesis of versatile Cu<sub>2-x</sub>S nanoprobe for enhanced MRI and infrared thermal/photoacoustic multimodal imaging. *Biomaterials* **2015**, *57*, 12-21.
53. Jokerst, J. V.; Cole, A. J.; Van de Sompel, D.; Gambhir, S. S., Gold nanorods for ovarian cancer detection with photoacoustic imaging and resection guidance via Raman imaging in living mice. *ACS nano* **2012**, *6* (11), 10366-10377.
54. Wilson, K.; Homan, K.; Emelianov, S., Biomedical photoacoustics beyond thermal expansion using triggered nanodroplet vaporization for contrast-enhanced imaging. *Nature Comm.* **2012**, *3*, 618.
55. Huynh, E.; Leung, B. Y.; Helfield, B. L.; Shakiba, M.; Gandier, J.-A.; Jin, C. S.; Master, E. R.; Wilson, B. C.; Goertz, D. E.; Zheng, G., In situ conversion of porphyrin microbubbles to nanoparticles for multimodality imaging. *Nature nanotechnology* **2015**, *10* (4), 325-332.
56. Chen, Y.-S.; Frey, W.; Kim, S.; Homan, K.; Kruizinga, P.; Sokolov, K.; Emelianov, S., Enhanced thermal stability of silica-coated gold nanorods for photoacoustic imaging and image-guided therapy. *Optics express* **2010**, *18* (9), 8867-8878.
57. Chen, Y.-S.; Frey, W.; Kim, S.; Kruizinga, P.; Homan, K.; Emelianov, S., Silica-coated gold nanorods as photoacoustic signal nanoamplifiers. *Nano letters* **2011**, *11* (2), 348-354.
58. Jokerst, J. V.; Thangaraj, M.; Kempen, P. J.; Sinclair, R.; Gambhir, S. S., Photoacoustic imaging of mesenchymal stem cells in living mice via silica-coated gold nanorods. *ACS nano* **2012**, *6* (7), 5920-5930.
59. Yang, H.-W.; Liu, H.-L.; Li, M.-L.; Hsi, I.-W.; Fan, C.-T.; Huang, C.-Y.; Lu, Y.-J.; Hua, M.-Y.; Chou, H.-Y.; Liaw, J.-W., Magnetic gold-nanorod/PNIPAAmMA nanoparticles for dual magnetic resonance and photoacoustic imaging and targeted photothermal therapy. *Biomaterials* **2013**, *34* (22), 5651-5660.
60. Chanda, N.; Shukla, R.; Zambre, A.; Mekapothula, S.; Kulkarni, R. R.; Katti, K.; Bhattacharyya, K.; Fent, G. M.; Casteel, S. W.; Boote, E. J., An effective strategy for the synthesis of biocompatible gold nanoparticles using cinnamon phytochemicals for phantom CT imaging and photoacoustic detection of cancerous cells. *Pharmaceutical research* **2011**, *28* (2), 279-291.
61. Luke, G. P.; Myers, J. N.; Emelianov, S. Y.; Sokolov, K. V., Sentinel lymph node biopsy revisited: ultrasound-guided photoacoustic detection of micrometastases using molecularly targeted plasmonic nanosensors. *Cancer research* **2014**, *74* (19), 5397-5408.

62. Yang, K.; Zhu, L.; Nie, L.; Sun, X.; Cheng, L.; Wu, C.; Niu, G.; Chen, X.; Liu, Z., Visualization of protease activity in vivo using an activatable photo-acoustic imaging probe based on CuS nanoparticles. *Theranostics* **2014**, *4* (2), 134-141.
63. Hu, C. M.; Fang, R. H.; Wang, K. C.; Luk, B. T.; Thamphiwatana, S.; Dehaini, D.; Nguyen, P.; Angsantikul, P.; Wen, C. H.; Kroll, A. V.; Carpenter, C.; Ramesh, M.; Qu, V.; Patel, S. H.; Zhu, J.; Shi, W.; Hofman, F. M.; Chen, T. C.; Gao, W.; Zhang, K.; Chien, S.; Zhang, L., Nanoparticle biointerfacing by platelet membrane cloaking. *Nature* **2015**, *526* (7571), 118-21.
64. Fang, R. H.; Hu, C. M.; Luk, B. T.; Gao, W.; Copp, J. A.; Tai, Y.; O'Connor, D. E.; Zhang, L., Cancer cell membrane-coated nanoparticles for anticancer vaccination and drug delivery. *Nano Lett* **2014**, *14* (4), 2181-8.
65. Simon, J. D.; Peles, D. N., The Red and the Black. *Accounts of Chemical Research* **2010**, *43* (11), 1452-1460.
66. Meredith, P.; Sarna, T., The physical and chemical properties of eumelanin. *Pigment cell research* **2006**, *19* (6), 572-594.
67. Simon, J. D., Spectroscopic and Dynamic Studies of the Epidermal Chromophores trans-Urocanic Acid and Eumelanin. *Accounts of Chemical Research* **2000**, *33* (5), 307-313.
68. Xiao, M.; Li, Y.; Zhao, J.; Wang, Z.; Gao, M.; Gianneschi, N. C.; Dhinojwala, A.; Shawkey, M. D., Stimuli-Responsive Structurally Colored Films from Bioinspired Synthetic Melanin Nanoparticles. *Chemistry of Materials* **2016**, *28* (15), 5516-5521.
69. Xiao, M.; Li, Y.; Allen, M. C.; Deheyn, D. D.; Yue, X.; Zhao, J.; Gianneschi, N. C.; Shawkey, M. D.; Dhinojwala, A., Bio-inspired structural colors produced via self-assembly of synthetic melanin nanoparticles. *ACS nano* **2015**, *9* (5), 5454-5460.
70. Zhang, R.; Fan, Q.; Yang, M.; Cheng, K.; Lu, X.; Zhang, L.; Huang, W.; Cheng, Z., Engineering melanin nanoparticles as an efficient drug-delivery system for imaging-guided chemotherapy. *Advanced Materials* **2015**, *27* (34), 5063-5069.
71. Horikoshi, T.; Ito, S.; Wakamatsu, K.; Onodera, H.; Eguchi, H., Evaluation of melanin-related metabolites as markers of melanoma progression. *Cancer* **1994**, *73* (3), 629-636.
72. Schwarz, S. T.; Rittman, T.; Gontu, V.; Morgan, P. S.; Bajaj, N.; Auer, D. P., T1-Weighted MRI shows stage-dependent substantia nigra signal loss in Parkinson's disease. *Mov. Disord.* **2011**, *26* (9), 1633-1638.
73. Kim, D. J.; Ju, K.-Y.; Lee, J.-K., The synthetic melanin nanoparticles having an excellent binding capacity of heavy metal ions. *Bulletin of the Korean Chemical Society* **2012**, *33* (11), 3788-3792.
74. Ju, K.-Y.; Lee, J. W.; Im, G. H.; Lee, S.; Pyo, J.; Park, S. B.; Lee, J. H.; Lee, J.-K., Bio-Inspired, Melanin-Like Nanoparticles as a Highly Efficient Contrast Agent for T1-Weighted Magnetic Resonance Imaging. *Biomacromolecules* **2013**, *14* (10), 3491-3497.

75. Liu, Y.; Ai, K.; Liu, J.; Deng, M.; He, Y.; Lu, L., Dopamine-Melanin Colloidal Nanospheres: An Efficient Near-Infrared Photothermal Therapeutic Agent for In Vivo Cancer Therapy. *Advanced Materials* **2013**, *25* (9), 1353-1359.
76. Li, Y.; Jiang, C.; Zhang, D.; Wang, Y.; Ren, X.; Ai, K.; Chen, X.; Lu, L., Targeted polydopamine nanoparticles enable photoacoustic imaging guided chemo-photothermal synergistic therapy of tumor. *Acta Biomaterialia* **2017**, *47*, 124-134.
77. Li, Y.; Xie, Y.; Wang, Z.; Zang, N.; Carniato, F.; Huang, Y.; Andolina, C. M.; Parent, L. R.; Ditri, T. B.; Walter, E. D., Structure and function of iron-loaded synthetic melanin. *ACS nano* **2016**, *10* (11), 10186-10194.
78. Wang, Z.; Carniato, F.; Xie, Y.; Huang, Y.; Li, Y.; He, S.; Zang, N.; Rinehart, J. D.; Botta, M.; Gianneschi, N. C., High Relaxivity Gadolinium-Polydopamine Nanoparticles. *Small* **2017**, *13* (43), 1701830.
79. Repenko, T.; Fokong, S.; De Laporte, L.; Go, D.; Kiessling, F.; Lammers, T.; Kuehne, A. J., Water-soluble dopamine-based polymers for photoacoustic imaging. *Chem. Commun.* **2015**, *51* (28), 6084-6087.
80. Liu, X.; Cao, J.; Li, H.; Li, J.; Jin, Q.; Ren, K.; Ji, J., Mussel-inspired polydopamine: a biocompatible and ultrastable coating for nanoparticles in vivo. *ACS nano* **2013**, *7* (10), 9384-9395.
81. Zhong, X.; Yang, K.; Dong, Z.; Yi, X.; Wang, Y.; Ge, C.; Zhao, Y.; Liu, Z., Polydopamine as a biocompatible multifunctional nanocarrier for combined radioisotope therapy and chemotherapy of cancer. *Advanced Functional Materials* **2015**, *25* (47), 7327-7336.
82. Lin, L.-S.; Cong, Z.-X.; Cao, J.-B.; Ke, K.-M.; Peng, Q.-L.; Gao, J.; Yang, H.-H.; Liu, G.; Chen, X., Multifunctional Fe<sub>3</sub>O<sub>4</sub>@ polydopamine core-shell nanocomposites for intracellular mRNA detection and imaging-guided photothermal therapy. *ACS nano* **2014**, *8* (4), 3876-3883.
83. Liopo, A.; Su, R.; Oraevsky, A. A., Melanin nanoparticles as a novel contrast agent for photoacoustic tomography. *Photoacoustics* **2015**, *3* (1), 35-43.
84. Yan, J.; Ji, Y.; Zhang, P.; Lu, X.; Fan, Q.; Pan, D.; Yang, R.; Xu, Y.; Wang, L.; Zhang, L., Melanin nanoparticles as an endogenous agent for efficient iron overload therapy. *Journal of Materials Chemistry B* **2016**, *4* (45), 7233-7240.
85. Kircher, M. F.; Gambhir, S. S.; Grimm, J., Noninvasive cell-tracking methods. *Nat Rev Clin Oncol* **2011**, *8* (11), 677-688.
86. Wang, J.; Jokerst, J. V., Stem Cell Imaging: Tools to Improve Cell Delivery and Viability. *Stem Cells International* **2016**, *2016*, 16.
87. Na, H. B.; Song, I. C.; Hyeon, T., Inorganic nanoparticles for MRI contrast agents. *Advanced Materials* **2009**, *21* (21), 2133-2148.

88. Laurent, S.; Forge, D.; Port, M.; Roch, A.; Robic, C.; Vander Elst, L.; Muller, R. N., Magnetic iron oxide nanoparticles: Synthesis, stabilization, vectorization, physicochemical characterizations and biological applications. *Chemical Reviews* **2008**, *108* (6), 2064-2110.
89. Kraitchman, D. L.; Heldman, A. W.; Atalar, E.; Amado, L. C.; Martin, B. J.; Pittenger, M. F.; Hare, J. M.; Bulte, J. W., In vivo magnetic resonance imaging of mesenchymal stem cells in myocardial infarction. *Circulation* **2003**, *107* (18), 2290-2293.
90. Li, K.; Ding, D.; Huo, D.; Pu, K. Y.; Thao, N. N. P.; Hu, Y.; Li, Z.; Liu, B., Conjugated Polymer Based Nanoparticles as Dual-Modal Probes for Targeted In Vivo Fluorescence and Magnetic Resonance Imaging. *Advanced Functional Materials* **2012**, *22* (15), 3107-3115.
91. Daldrup-Link, H. E.; Rudelius, M.; Oostendorp, R. A.; Settles, M.; Piontek, G.; Metz, S.; Rosenbrock, H.; Keller, U.; Heinzmann, U.; Rummeny, E. J., Targeting of hematopoietic progenitor cells with MR contrast agents. *Radiology* **2003**, *228* (3), 760-767.
92. Bulte, J. W.; Douglas, T.; Witwer, B.; Zhang, S.-C.; Strable, E.; Lewis, B. K.; Zywicke, H.; Miller, B.; Van Gelderen, P.; Moskowitz, B. M., Magnetodendrimers allow endosomal magnetic labeling and in vivo tracking of stem cells. *Nature biotechnology* **2001**, *19* (12), 1141.
93. Huang, Y.; Wei, T.; Yu, J.; Hou, Y.; Cai, K.; Liang, X.-J., Multifunctional metal rattle-type nanocarriers for MRI-guided photothermal cancer therapy. *Mol. Pharm.* **2014**, *11* (10), 3386-3394.
94. Huang, J.; Bu, L.; Xie, J.; Chen, K.; Cheng, Z.; Li, X.; Chen, X., Effects of nanoparticle size on cellular uptake and liver MRI with polyvinylpyrrolidone-coated iron oxide nanoparticles. *ACS Nano* **2010**, *4* (12), 7151-7160.
95. Lauffer, R. B., Paramagnetic metal complexes as water proton relaxation agents for NMR imaging: Theory and design. *Chemical Reviews* **1987**, *87* (5), 901-927.
96. Caravan, P.; Ellison, J. J.; McMurry, T. J.; Lauffer, R. B., Gadolinium(III) chelates as MRI contrast agents: Structure, dynamics, and applications. *Chemical Reviews* **1999**, *99* (9), 2293-2352.
97. Caravan, P., Strategies for increasing the sensitivity of gadolinium based MRI contrast agents. *Chemical Society Reviews* **2006**, *35* (6), 512-523.
98. Aime, S.; Botta, M.; Terreno, E., Gd(III)-BASED CONTRAST AGENTS FOR MRI. *Advances in Inorganic Chemistry* **2006**, *57*, 173-237.
99. Aime, S.; Botta, M.; Terreno, E., Gd (III)-based contrast agents for MRI. *Adv. Inorg. Chem* **2005**, *57*, 173-237.
100. Kim, T.; Lemaster, J. E.; Chen, F.; Li, J.; Jokerst, J. V., Photoacoustic Imaging of Human Mesenchymal Stem Cells Labeled with Prussian Blue–Poly (l-lysine) Nanocomplexes. *ACS Nano* **2017**, *11* (9), 9022-9032.

101. Weber, J.; Beard, P. C.; Bohndiek, S. E., Contrast agents for molecular photoacoustic imaging. *Nature Methods* **2016**, *13* (8), 639-650.
102. Lemaster, J. E.; Chen, F.; Kim, T.; Hariri, A.; Jokerst, J. V., Development of a Trimodal Contrast Agent for Acoustic and Magnetic Particle Imaging of Stem Cells. *ACS Applied Nano Materials* **2018**, *1* (3), 1321-1331.
103. Chen, F.; Ma, M.; Wang, J.; Wang, F.; Chern, S.-X.; Zhao, E. R.; Jhunjhunwala, A.; Darmadi, S.; Chen, H.; Jokerst, J. V., Exosome-like silica nanoparticles: a novel ultrasound contrast agent for stem cell imaging. *Nanoscale* **2017**, *9* (1), 402-411.
104. Foroutan, F.; Jokerst, J. V.; Gambhir, S. S.; Vermesh, O.; Kim, H.-W.; Knowles, J. C., Sol-gel synthesis and electrospraying of biodegradable (P2O5) 55-(CaO) 30-(Na2O) 15 glass nanospheres as a transient contrast agent for ultrasound stem cell imaging. *ACS nano* **2015**, *9* (2), 1868-1877.
105. Pu, K.; Shuhendler, A. J.; Valta, M. P.; Cui, L.; Saar, M.; Peehl, D. M.; Rao, J., Phosphorylcholine-Coated Semiconducting Polymer Nanoparticles as Rapid and Efficient Labeling Agents for In Vivo Cell Tracking. *Advanced healthcare materials* **2014**, *3* (8), 1292-1298.
106. Larsson, B.; Tjälve, H., Studies on the melanin-affinity of metal ions. *Acta Physiologica Scandinavica* **1978**, *104* (4), 479-484.
107. Xiao, M.; Hu, Z.; Wang, Z.; Li, Y.; Tormo, A. D.; Le Thomas, N.; Wang, B.; Gianneschi, N. C.; Shawkey, M. D.; Dhinojwala, A., Bioinspired bright noniridescent photonic melanin supraballs. *Science Advances* **2017**, *3* (9).
108. Abràmoff, M. D.; Magalhães, P. J.; Ram, S. J., Image processing with ImageJ. *Biophotonics international* **2004**, *11* (7), 36-42.
109. Wang, Z.; Xie, Y.; Li, Y.; Huang, Y.; Parent, L. R.; Ditri, T.; Zang, N.; Rinehart, J. D.; Gianneschi, N. C., Tunable, Metal-Loaded Polydopamine Nanoparticles Analyzed by Magnetometry. *Chemistry of Materials* **2017**, *29* (19), 8195-8201.
110. Miao, Z.-H.; Wang, H.; Yang, H.; Li, Z.-L.; Zhen, L.; Xu, C.-Y., Intrinsically Mn<sup>2+</sup>-chelated polydopamine nanoparticles for simultaneous magnetic resonance imaging and photothermal ablation of cancer cells. *ACS applied materials & interfaces* **2015**, *7* (31), 16946-16952.
111. Lee, S. Y.; Lin, M.; Lee, A.; Park, Y. I., Lanthanide-Doped Nanoparticles for Diagnostic Sensing. *Nanomaterials* **2017**, *7* (12), 411.
112. Kim, C.; Erpelding, T. N.; Jankovic, L.; Pashley, M. D.; Wang, L. V., Deeply penetrating in vivo photoacoustic imaging using a clinical ultrasound array system. *Biomedical optics express* **2010**, *1* (1), 278-284.



113. Song, K. H.; Stein, E. W.; Margenthaler, J. A.; Wang, L. V., Noninvasive photoacoustic identification of sentinel lymph nodes containing methylene blue in vivo in a rat model. *Journal of biomedical optics* **2008**, *13* (5), 054033-054033-6.
114. Ge, R.; Lin, M.; Li, X.; Liu, S.; Wang, W.; Li, S.; Zhang, X.; Liu, Y.; Liu, L.; Shi, F.; Sun, H.; Zhang, H.; Yang, B., Cu<sup>2+</sup>-Loaded Polydopamine Nanoparticles for Magnetic Resonance Imaging-Guided pH- and Near-Infrared-Light-Stimulated Thermochemotherapy. *ACS Applied Materials & Interfaces* **2017**, *9* (23), 19706-19716.
115. Lyu, Y.; Zeng, J.; Jiang, Y.; Zhen, X.; Wang, T.; Qiu, S.; Lou, X.; Gao, M.; Pu, K., Enhancing both biodegradability and efficacy of semiconducting polymer nanoparticles for photoacoustic imaging and photothermal therapy. *ACS nano* **2018**, *12* (2), 1801-1810.
116. Zhen, X.; Feng, X.; Xie, C.; Zheng, Y.; Pu, K., Surface engineering of semiconducting polymer nanoparticles for amplified photoacoustic imaging. *Biomaterials* **2017**, *127*, 97-106.
117. Repenko, T.; Rix, A.; Nedilko, A.; Rose, J.; Hermann, A.; Vinokur, R.; Moli, S.; Cao-Milà, R.; Mayer, M.; von Plessen, G., Strong photoacoustic signal enhancement by coating gold nanoparticles with melanin for biomedical imaging. *Advanced Functional Materials* **2018**, *28* (7), 1705607.
118. Sasaki, M.; Shibata, E.; Kanbara, Y.; Ehara, S., Enhancement effects and relaxivities of gadolinium-DTPA at 1.5 versus 3 Tesla: a phantom study. *Magn. Reson. Med. Sci.* **2005**, *4* (3), 145-149.
119. Tallury, P.; Santra, S.; Sharma, P.; De Castro, M.; Maria, B.; Bengtsson, N.; Biswas, S.; Saha, A. K.; Walter, G. A.; Scott, E. A., Fluorescent and paramagnetic chitosan nanoparticles that exhibit high magnetic resonance relaxivity: Synthesis, characterization and in vitro studies. *Journal of biomedical nanotechnology* **2011**, *7* (5), 724-729.
120. Tseng, C.-L.; Shih, I.-L.; Stobinski, L.; Lin, F.-H., Gadolinium hexanedione nanoparticles for stem cell labeling and tracking via magnetic resonance imaging. *Biomaterials* **2010**, *31* (20), 5427-5435.
121. Henning, T. D.; Saborowski, O.; Golovko, D.; Boddington, S.; Bauer, J. S.; Fu, Y.; Meier, R.; Pietsch, H.; Sennino, B.; McDonald, D. M., Cell labeling with the positive MR contrast agent Gadofluorine M. *Eur. Radiol.* **2007**, *17* (5), 1226-1234.
122. Huang, D.-M.; Hung, Y.; Ko, B.-S.; Hsu, S.-C.; Chen, W.-H.; Chien, C.-L.; Tsai, C.-P.; Kuo, C.-T.; Kang, J.-C.; Yang, C.-S., Highly efficient cellular labeling of mesoporous nanoparticles in human mesenchymal stem cells: implication for stem cell tracking. *The FASEB journal* **2005**, *19* (14), 2014-2016.
123. Zhao, F.; Zhao, Y.; Liu, Y.; Chang, X.; Chen, C.; Zhao, Y., Cellular uptake, intracellular trafficking, and cytotoxicity of nanomaterials. *Small* **2011**, *7* (10), 1322-1337.
124. Stroh, A.; Faber, C.; Neuberger, T.; Lorenz, P.; Sieland, K.; Jakob, P. M.; Webb, A.; Pilgrim, H.; Schober, R.; Pohl, E. E., In vivo detection limits of magnetically labeled embryonic

stem cells in the rat brain using high-field (17.6 T) magnetic resonance imaging. *NeuroImage* **2005**, *24* (3), 635-645.

125. Shapiro, E. M.; Sharer, K.; Skrtic, S.; Koretsky, A. P., In vivo detection of single cells by MRI. *Magn. Reson. Med.* **2006**, *55* (2), 242-249.

126. Traverse, J. H.; Henry, T. D.; Vaughan, D. E.; Ellis, S. G.; Pepine, C. J.; Willerson, J. T.; Zhao, D. X.; Simpson, L. M.; Penn, M. S.; Byrne, B. J., LateTIME: a phase-II, randomized, double-blinded, placebo-controlled, pilot trial evaluating the safety and effect of administration of bone marrow mononuclear cells 2 to 3 weeks after acute myocardial infarction. *Texas Heart Institute Journal* **2010**, *37* (4), 412.

127. Traverse, J. H.; Henry, T. D.; Vaughn, D. E.; Ellis, S. G.; Pepine, C. J.; Willerson, J. T.; Zhao, D. X.; Piller, L. B.; Penn, M. S.; Byrne, B. J., Rationale and design for TIME: a phase II, randomized, double-blind, placebo-controlled pilot trial evaluating the safety and effect of timing of administration of bone marrow mononuclear cells after acute myocardial infarction. *Am. Heart J.* **2009**, *158* (3), 356-363.

128. Bolli, R.; Chugh, A. R.; D'Amario, D.; Loughran, J. H.; Stoddard, M. F.; Ikram, S.; Beache, G. M.; Wagner, S. G.; Leri, A.; Hosoda, T., Cardiac stem cells in patients with ischaemic cardiomyopathy (SCIPIO): initial results of a randomised phase 1 trial. *The Lancet* **2011**, *378* (9806), 1847-1857.

129. Zhou, Z.; Lu, Z. R., Gadolinium-based contrast agents for magnetic resonance cancer imaging. *Wiley Interdisciplinary Reviews: Nanomedicine and Nanobiotechnology* **2013**, *5* (1), 1-18.

130. Rogosnitzky, M.; Branch, S., Gadolinium-based contrast agent toxicity: a review of known and proposed mechanisms. *BioMetals* **2016**, *29* (3), 365-376.

131. Tse, H.-F.; Kwong, Y.-L.; Chan, J. K.; Lo, G.; Ho, C.-L.; Lau, C.-P., Angiogenesis in ischaemic myocardium by intramyocardial autologous bone marrow mononuclear cell implantation. *The Lancet* **2003**, *361* (9351), 47-49.

132. Aime, S.; Caravan, P., Biodistribution of gadolinium-based contrast agents, including gadolinium deposition. *Journal of Magnetic Resonance Imaging: An Official Journal of the International Society for Magnetic Resonance in Medicine* **2009**, *30* (6), 1259-1267.

133. Niendorf, H.; Haustein, J.; Cornelius, I.; Alhassan, A.; Clauss, W., Safety of gadolinium-DTPA: extended clinical experience. *Magn. Reson. Med.* **1991**, *22* (2), 222-228.

134. Lemaster, J. E.; Wang, Z.; Hariri, A.; Chen, F.; Hu, Z.; Huang, Y.; Barback, C. V.; Cochran, R.; Gianneschi, N. C.; Jokerst, J. V., Gadolinium Doping Enhances the Photoacoustic Signal of Synthetic Melanin Nanoparticles: A Dual Modality Contrast Agent for Stem Cell Imaging. *Chemistry of Materials* **2018**, *31* (1), 251-259.

135. Jiang, Q.; Luo, Z.; Men, Y.; Yang, P.; Peng, H.; Guo, R.; Tian, Y.; Pang, Z.; Yang, W., Red blood cell membrane-camouflaged melanin nanoparticles for enhanced photothermal therapy. *Biomaterials* **2017**, *143*, 29-45.
136. Tian, Y.; Zhao, Y.; Liu, W.; Liu, Y.; Tang, Y.; Teng, Z.; Zhang, C.; Wang, S.; Lu, G., Photosensitizer-loaded biomimetic platform for multimodal imaging-guided synergistic phototherapy. *RSC Advances* **2018**, *8* (56), 32200-32210.
137. Riley, P., Melanin. *The international journal of biochemistry & cell biology* **1997**, *29* (11), 1235-1239.
138. Ortonne, J. P., Photoprotective properties of skin melanin. *British Journal of Dermatology* **2002**, *146*, 7-10.
139. Watt, W., Thermoregulation and photoperiodically controlled melanin variation in *Colias eurytheme*. *Proc Natl Acad Sci USA* **1969**, *63*, 767-774.
140. Seagle, B.-L. L.; Rezai, K. A.; Gasyna, E. M.; Kobori, Y.; Rezaei, K. A.; Norris, J. R., Time-resolved detection of melanin free radicals quenching reactive oxygen species. *Journal of the American Chemical Society* **2005**, *127* (32), 11220-11221.
141. Agin, P. P.; Sayre, R. M.; Chedekel, M. R., Photodegradation of phaeomelanin: an in vitro model. *Photochemistry and photobiology* **1980**, *31* (4), 359-362.
142. Thody, A. J.; Higgins, E. M.; Wakamatsu, K.; Ito, S.; Burchill, S. A.; Marks, J. M., Pheomelanin as well as eumelanin is present in human epidermis. *Journal of Investigative Dermatology* **1991**, *97* (2), 340-344.
143. Ball, V.; Gracio, J.; Vila, M.; Singh, M. K.; Metz-Boutigue, M.-H. I. n.; Michel, M.; Bour, J. r. m.; Toniazzo, V. r.; Ruch, D.; Buehler, M. J., Comparison of Synthetic Dopamine–Eumelanin Formed in the Presence of Oxygen and Cu<sup>2+</sup> Cations as Oxidants. *Langmuir* **2013**, *29* (41), 12754-12761.
144. Liu, Y.; Ai, K.; Lu, L., Polydopamine and its derivative materials: synthesis and promising applications in energy, environmental, and biomedical fields. *Chemical reviews* **2014**, *114* (9), 5057-5115.
145. d'Ischia, M.; Napolitano, A.; Ball, V.; Chen, C.-T.; Buehler, M. J., Polydopamine and eumelanin: From structure–property relationships to a unified tailoring strategy. *Accounts of chemical research* **2014**, *47* (12), 3541-3550.
146. Liu, M.; Zeng, G.; Wang, K.; Wan, Q.; Tao, L.; Zhang, X.; Wei, Y., Recent developments in polydopamine: an emerging soft matter for surface modification and biomedical applications. *Nanoscale* **2016**, *8* (38), 16819-16840.
147. Qu, K.; Wang, Y.; Vasileff, A.; Jiao, Y.; Chen, H.; Zheng, Y., Polydopamine-inspired nanomaterials for energy conversion and storage. *Journal of Materials Chemistry A* **2018**, *6* (44), 21827-21846.

148. Zou, Y.; Wang, Z.; Chen, Z.; Zhang, Q.-P.; Zhang, Q.; Tian, Y.; Ren, S.; Li, Y., Synthetic Melanin Hybrid Patchy Nanoparticle Photocatalysts. *The Journal of Physical Chemistry C* **2019**, *123* (9), 5345-5352.
149. Wang, C.; Wang, D.; Dai, T.; Xu, P.; Wu, P.; Zou, Y.; Yang, P.; Hu, J.; Li, Y.; Cheng, Y., Skin Pigmentation-Inspired Polydopamine Sunscreens. *Advanced Functional Materials* **2018**, *28* (33), 1802127.
150. Zhou, Z.; Yan, Y.; Wang, L.; Zhang, Q.; Cheng, Y., Melanin-like nanoparticles decorated with an autophagy-inducing peptide for efficient targeted photothermal therapy. *Biomaterials* **2019**, *203*, 63-72.
151. Ju, K.-Y.; Lee, Y.; Lee, S.; Park, S. B.; Lee, J.-K., Bioinspired polymerization of dopamine to generate melanin-like nanoparticles having an excellent free-radical-scavenging property. *Biomacromolecules* **2011**, *12* (3), 625-632.
152. Amin, D.; Sugnaux, C.; Lau, K.; Messersmith, P., Size control and fluorescence labeling of polydopamine melanin-mimetic nanoparticles for intracellular imaging. *Biomimetics* **2017**, *2* (3), 17.
153. Chen, T.-P.; Liu, T.; Su, T.-L.; Liang, J., Self-polymerization of dopamine in acidic environments without oxygen. *Langmuir* **2017**, *33* (23), 5863-5871.
154. De Jong, W. H.; Hagens, W. I.; Krystek, P.; Burger, M. C.; Sips, A. J.; Geertsma, R. E., Particle size-dependent organ distribution of gold nanoparticles after intravenous administration. *Biomaterials* **2008**, *29* (12), 1912-1919.
155. Wang, Z.; Xu, C.; Lu, Y.; Wei, G.; Ye, G.; Sun, T.; Chen, J., Microplasma electrochemistry controlled rapid preparation of fluorescent polydopamine nanoparticles and their application in uranium detection. *Chemical Engineering Journal* **2018**, *344*, 480-486.
156. Wang, X.; Chen, Z.; Yang, P.; Hu, J.; Wang, Z.; Li, Y., Size Control Synthesis of Melanin-Like Polydopamine Nanoparticles by Tuning Radicals. *Polymer Chemistry* **2019**.
157. Chen, L.; Lin, Z.; Liu, L.; Zhang, X.; Shi, W.; Ge, D.; Sun, Y., Fe<sup>2+</sup>/Fe<sup>3+</sup> ions chelated with ultrasmall polydopamine nanoparticles inducing Ferroptosis for cancer therapy. *ACS Biomaterials Science & Engineering* **2019**.
158. Ni, Y.; Chen, F.; Shi, L.; Tong, G.; Wang, J.; Li, H.; Yu, C.; Zhou, Y., Facile Preparation of Water-Soluble and Cytocompatible Small-Sized Chitosan-Polydopamine Nanoparticles. *Chinese Journal of Chemistry* **2017**, *35* (6), 931-937.
159. Lin, J.-H.; Yu, C.-J.; Yang, Y.-C.; Tseng, W.-L., Formation of fluorescent polydopamine dots from hydroxyl radical-induced degradation of polydopamine nanoparticles. *Physical Chemistry Chemical Physics* **2015**, *17* (23), 15124-15130.

160. Xiao, M.; Hu, Z.; Wang, Z.; Li, Y.; Tormo, A. D.; Le Thomas, N.; Wang, B.; Gianneschi, N. C.; Shawkey, M. D.; Dhinojwala, A., Bioinspired bright noniridescent photonic melanin supraballs. *Science advances* **2017**, *3* (9), e1701151.
161. Lee, H.; Dellatore, S. M.; Miller, W. M.; Messersmith, P. B., Mussel-inspired surface chemistry for multifunctional coatings. *science* **2007**, *318* (5849), 426-430.
162. Du, X.; Li, L.; Li, J.; Yang, C.; Frenkel, N.; Welle, A.; Heissler, S.; Nefedov, A.; Grunze, M.; Levkin, P. A., UV-Triggered Dopamine Polymerization: Control of Polymerization, Surface Coating, and Photopatterning. *Advanced Materials* **2014**, *26* (47), 8029-8033.
163. Hong, S.; Na, Y. S.; Choi, S.; Song, I. T.; Kim, W. Y.; Lee, H., Non-covalent self-assembly and covalent polymerization co-contribute to polydopamine formation. *Advanced Functional Materials* **2012**, *22* (22), 4711-4717.
164. Afkhami, A.; Nematollahi, D.; Khalafi, L.; Rafiee, M., Kinetic study of the oxidation of some catecholamines by digital simulation of cyclic voltammograms. *International journal of chemical kinetics* **2005**, *37* (1), 17-24.
165. McElfresh, C.; Harrington, T.; Vecchio, K. S., Application of a novel new multispectral nanoparticle tracking technique. *Measurement Science and Technology* **2018**, *29* (6), 065002.
166. Ball, V., Polydopamine nanomaterials: recent advances in synthesis methods and applications. *Frontiers in bioengineering and biotechnology* **2018**, *6*.
167. Bridelli, M. G., Self-assembly of melanin studied by laser light scattering. *Biophysical chemistry* **1998**, *73* (3), 227-239.
168. Decuzzi, P.; Godin, B.; Tanaka, T.; Lee, S.-Y.; Chiappini, C.; Liu, X.; Ferrari, M., Size and shape effects in the biodistribution of intravascularly injected particles. *Journal of Controlled Release* **2010**, *141* (3), 320-327.
169. Wang, H. Y.; Sun, Y.; Tang, B., Study on fluorescence property of dopamine and determination of dopamine by fluorimetry. *Talanta* **2002**, *57* (5), 899-907.
170. Meredith, P.; Powell, B. J.; Riesz, J.; Nighswander-Rempel, S. P.; Pederson, M. R.; Moore, E. G., Towards structure–property–function relationships for eumelanin. *Soft Matter* **2006**, *2* (1), 37-44.
171. Liu, Y.; Ai, K.; Liu, J.; Deng, M.; He, Y.; Lu, L., Dopamine-melanin colloidal nanospheres: an efficient near-infrared photothermal therapeutic agent for in vivo cancer therapy. *Advanced materials* **2013**, *25* (9), 1353-1359.
172. Cho, S.; Kim, S.-H., Hydroxide ion-mediated synthesis of monodisperse dopamine–melanin nanospheres. *Journal of colloid and interface science* **2015**, *458*, 87-93.
173. Herlinger, E.; Jameson, R. F.; Linert, W., Spontaneous autoxidation of dopamine. *Journal of the Chemical Society, Perkin Transactions 2* **1995**, (2), 259-263.

174. Raffa, R. B.; Valdez, J. M.; Holland, L. J.; Schulingkamp, R. J., Energy-dependent UV light-induced disruption of (-) sulpiride antagonism of dopamine. *European journal of pharmacology* **2000**, *406* (3), R11-R12.
175. Chen, C.-T.; Martin-Martinez, F. J.; Jung, G. S.; Buehler, M. J., Polydopamine and eumelanin molecular structures investigated with ab initio calculations. *Chemical science* **2017**, *8* (2), 1631-1641.
176. Zhang, C.; Ou, Y.; Lei, W. X.; Wan, L. S.; Ji, J.; Xu, Z. K., CuSO<sub>4</sub>/H<sub>2</sub>O<sub>2</sub>-induced rapid deposition of polydopamine coatings with high uniformity and enhanced stability. *Angewandte Chemie International Edition* **2016**, *55* (9), 3054-3057.
177. Salomäki, M.; Marttila, L.; Kivelä, H.; Ouvinen, T.; Lukkari, J., Effects of pH and oxidants on the first steps of polydopamine formation: A thermodynamic approach. *The Journal of Physical Chemistry B* **2018**, *122* (24), 6314-6327.
178. Kang, H.; Kim, M.; Feng, Q.; Lin, S.; Wei, K.; Li, R.; Choi, C. J.; Kim, T.-H.; Li, G.; Oh, J.-M., Nanolayered hybrid mediates synergistic co-delivery of ligand and ligation activator for inducing stem cell differentiation and tissue healing. *Biomaterials* **2017**, *149*, 12-28.
179. Feng, Q.; Wei, K.; Lin, S.; Xu, Z.; Sun, Y.; Shi, P.; Li, G.; Bian, L., Mechanically resilient, injectable, and bioadhesive supramolecular gelatin hydrogels crosslinked by weak host-guest interactions assist cell infiltration and in situ tissue regeneration. *Biomaterials* **2016**, *101*, 217-228.
180. Li, R.; Xu, J.; Wong, D. S. H.; Li, J.; Zhao, P.; Bian, L., Self-assembled N-cadherin mimetic peptide hydrogels promote the chondrogenesis of mesenchymal stem cells through inhibition of canonical Wnt/ $\beta$ -catenin signaling. *Biomaterials* **2017**, *145*, 33-43.
181. Kang, H.; Wong, D. S. H.; Yan, X.; Jung, H. J.; Kim, S.; Lin, S.; Wei, K.; Li, G.; Dravid, V. P.; Bian, L., Remote Control of Multimodal Nanoscale Ligand Oscillations Regulates Stem Cell Adhesion and Differentiation. *ACS Nano* **2017**, *11* (10), 9636-9649.
182. Segers, V. F.; Lee, R. T., Stem-cell therapy for cardiac disease. *Nature* **2008**, *451* (7181), 937-942.
183. Masumoto, H.; Yamashita, J., Exploiting human iPS cell-derived cardiovascular cell populations toward cardiac regenerative therapy. *Stem Cell Transl. Invest.* **2016**, *3*.
184. Gouadon, E.; Moore-Morris, T.; Smit, N. W.; Chatenoud, L.; Coronel, R.; Harding, S. E.; Jourdon, P.; Lambert, V.; Rucker-Martin, C.; Pucéat, M., Concise Review: Pluripotent Stem Cell-Derived Cardiac Cells, A Promising Cell Source for Therapy of Heart Failure: Where Do We Stand? *Stem Cells* **2016**, *34* (1), 34-43.
185. Terzic, A.; Behfar, A., Stem cell therapy for heart failure: ensuring regenerative proficiency. *Trends Cardiovasc. Med.* **2016**, *26* (5), 395-404.
186. Broughton, K. M.; Sussman, M. A., Empowering adult stem cells for myocardial regeneration V2. 0. *Circ. Res.* **2016**, *118* (5), 867-880.

187. Noiseux, N.; Mansour, S.; Weisel, R.; Stevens, L.-M.; Der Sarkissian, S.; Tsang, K.; Crean, A. M.; Larose, E.; Li, S.-H.; Wintersperger, B., The IMPACT-CABG trial: A multicenter, randomized clinical trial of CD133+ stem cell therapy during coronary artery bypass grafting for ischemic cardiomyopathy. *J. Thorac. Cardiovasc. Surg.* **2016**, *152* (6), 1582-1588. e2.
188. Bhatnagar, A.; Bolli, R.; Johnstone, B. H.; Traverse, J. H.; Henry, T. D.; Pepine, C. J.; Willerson, J. T.; Perin, E. C.; Ellis, S. G.; Zhao, D. X., Bone marrow cell characteristics associated with patient profile and cardiac performance outcomes in the LateTIME-Cardiovascular Cell Therapy Research Network (CCTRN) trial. *Am. Heart J.* **2016**, *179*, 142-150.
189. Gnecci, M.; He, H.; Noiseux, N.; Liang, O. D.; Zhang, L.; Morello, F.; Mu, H.; Melo, L. G.; Pratt, R. E.; Ingwall, J. S., Evidence supporting paracrine hypothesis for Akt-modified mesenchymal stem cell-mediated cardiac protection and functional improvement. *The FASEB Journal* **2006**, *20* (6), 661-669.
190. Ryan, A.; Murphy, M.; Barry, F., Mesenchymal stem/stromal cell therapy. *The Biology and Therapeutic Application of Mesenchymal Cells* **2017**, 426-440.
191. LaBarge, M. A.; Blau, H. M., Biological progression from adult bone marrow to mononucleate muscle stem cell to multinucleate muscle fiber in response to injury. *Cell* **2002**, *111* (4), 589-601.
192. Corbel, S. Y.; Lee, A.; Yi, L.; Duenas, J.; Brazelton, T. R.; Blau, H. M.; Rossi, F. M., Contribution of hematopoietic stem cells to skeletal muscle. *Nat. Med.* **2003**, *9* (12), 1528-1532.
193. Torrente, Y.; Belicchi, M.; Sampaolesi, M.; Pisati, F.; Meregalli, M.; D'Antona, G.; Tonlorenzi, R.; Porretti, L.; Gavina, M.; Mamchaoui, K., Human circulating AC133+ stem cells restore dystrophin expression and ameliorate function in dystrophic skeletal muscle. *J. Clin. Invest.* **2004**, *114* (2), 182-195.
194. Shabbir, A.; Zisa, D.; Leiker, M.; Johnston, C.; Lin, H.; Lee, T., Muscular dystrophy therapy by non-autologous mesenchymal stem cells: muscle regeneration without immunosuppression and inflammation. *Transplantation* **2009**, *87* (9), 1275.
195. Abdelwahid, E.; Kalvelyte, A.; Stulpinas, A.; de Carvalho, K. A. T.; Guarita-Souza, L. C.; Foldes, G., Stem cell death and survival in heart regeneration and repair. *Apoptosis* **2016**, *21* (3), 252-268.
196. Srivastava, A. K.; Kadayakkara, D. K.; Bar-Shir, A.; Gilad, A. A.; McMahon, M. T.; Bulte, J. W., Advances in using MRI probes and sensors for in vivo cell tracking as applied to regenerative medicine. *Dis. Models & Mech.* **2015**, *8* (4), 323-336.
197. Kircher, M. F.; Gambhir, S. S.; Grimm, J., Noninvasive cell-tracking methods. *Nature reviews Clinical oncology* **2011**, *8* (11), 677-688.
198. Beeres, S. L.; Bengel, F. M.; Bartunek, J.; Atsma, D. E.; Hill, J. M.; Vanderheyden, M.; Penicka, M.; Schalij, M. J.; Wijns, W.; Bax, J. J., Role of imaging in cardiac stem cell therapy. *Journal of the American College of Cardiology* **2007**, *49* (11), 1137-1148.

199. Meregalli, M.; Farini, A.; Parolini, D.; Maciotta, S.; Torrente, Y., Stem Cell Therapies to Treat Muscular Dystrophy. *BioDrugs* **2010**, *24* (4), 237-247.
200. Verwilt, P.; Park, S.; Yoon, B.; Kim, J. S., Recent advances in Gd-chelate based bimodal optical/MRI contrast agents. *Chemical Society Reviews* **2015**, *44* (7), 1791-1806.
201. Kim, T.; Lee, N.; Park, Y. I.; Kim, J.; Kim, J.; Lee, E. Y.; Yi, M.; Kim, B.-G.; Hyeon, T.; Yu, T., Mesoporous silica-coated luminescent Eu<sup>3+</sup> doped GdVO<sub>4</sub> nanoparticles for multimodal imaging and drug delivery. *RSC Advances* **2014**, *4* (86), 45687-45695.
202. de Schellenberger, A. A.; Kratz, H.; Farr, T. D.; Loewa, N.; Hauptmann, R.; Wagner, S.; Taupitz, M.; Schnorr, J.; Schellenberger, E. A., Labeling of mesenchymal stem cells for MRI with single-cell sensitivity. *International journal of nanomedicine* **2016**, *11*, 1517.
203. Zhang, M.; Liu, X.; Huang, J.; Wang, L.; Shen, H.; Luo, Y.; Li, Z.; Zhang, H.; Deng, Z.; Zhang, Z., Ultrasmall graphene oxide based T1 MRI contrast agent for in vitro and in vivo labeling of human mesenchymal stem cells. *Nanomedicine: Nanotechnology, Biology and Medicine* **2017**.
204. Gerig, G.; Kubler, O.; Kikinis, R.; Jolesz, F. A., Nonlinear anisotropic filtering of MRI data. *IEEE Transactions on medical imaging* **1992**, *11* (2), 221-232.
205. Cao, F.; Lin, S.; Xie, X.; Ray, P.; Patel, M.; Zhang, X.; Drukker, M.; Dylla, S. J.; Connolly, A. J.; Chen, X., In vivo visualization of embryonic stem cell survival, proliferation, and migration after cardiac delivery. *Circulation* **2006**, *113* (7), 1005-1014.
206. Love, Z.; Wang, F.; Dennis, J.; Awadallah, A.; Salem, N.; Lin, Y.; Weisenberger, A.; Majewski, S.; Gerson, S.; Lee, Z., Imaging of mesenchymal stem cell transplant by bioluminescence and PET. *Journal of Nuclear Medicine* **2007**, *48* (12), 2011-2020.
207. Sun, X.; Cai, W.; Chen, X., Positron emission tomography imaging using radiolabeled inorganic nanomaterials. *Accounts of chemical research* **2015**, *48* (2), 286.
208. Tolmachev, V.; Stone-Elander, S., Radiolabelled proteins for positron emission tomography: pros and cons of labelling methods. *Biochimica et Biophysica Acta (BBA)-General Subjects* **2010**, *1800* (5), 487-510.
209. Wallace, M. B.; Nietert, P. J.; Earle, C.; Krasna, M. J.; Hawes, R. H.; Hoffman, B. J.; Reed, C. E., An analysis of multiple staging management strategies for carcinoma of the esophagus: computed tomography, endoscopic ultrasound, positron emission tomography, and thoracoscopy/laparoscopy. *The Annals of thoracic surgery* **2002**, *74* (4), 1026-1032.
210. Dave, M.; Menghini, P.; Sugi, K.; Somoza, R.; Lee, Z.; Jain, M.; Caplan, A.; Cominelli, F., Ultrasound-guided Intracardiac Injection of Human Mesenchymal Stem Cells to Increase Homing to the Intestine for Use in Murine Models of Experimental Inflammatory Bowel Diseases. *Journal of visualized experiments: JoVE* **2017**, (127).
211. Kempen, P. J.; Greasley, S.; Parker, K. A.; Campbell, J. L.; Chang, H.-Y.; Jones, J. R.; Sinclair, R.; Gambhir, S. S.; Jokerst, J. V., Theranostic mesoporous silica nanoparticles biodegrade



after pro-survival drug delivery and ultrasound/magnetic resonance imaging of stem cells. *Theranostics* **2015**, *5* (6), 631.

212. Aguirre, A.; Ardeshirpour, Y.; Sanders, M. M.; Brewer, M.; Zhu, Q., Potential role of coregistered photoacoustic and ultrasound imaging in ovarian cancer detection and characterization. *Translational oncology* **2011**, *4* (1), 29-37.

213. Razansky, D.; Distel, M.; Vinegoni, C.; Ma, R.; Perrimon, N.; Köster, R. W.; Ntziachristos, V., Multispectral opto-acoustic tomography of deep-seated fluorescent proteins in vivo. *Nature Photonics* **2009**, *3* (7), 412-417.

214. Bayer, C. L.; Chen, Y.-S.; Kim, S.; Mallidi, S.; Sokolov, K.; Emelianov, S., Multiplex photoacoustic molecular imaging using targeted silica-coated gold nanorods. *Biomedical optics express* **2011**, *2* (7), 1828-1835.

215. Yin, M.; Bar-Zion, A.; Adam, D.; Foster, S., Combined contrast enhanced ultrasound and photoacoustic imaging reveals both functional flow patterns and dysfunctional vascular pooling in tumor models. AACR: 2016.

216. Bar-Zion, A.; Yin, M.; Adam, D.; Foster, F. S., Functional Flow Patterns and Static Blood Pooling in Tumors Revealed by Combined Contrast-Enhanced Ultrasound and Photoacoustic Imaging. *Cancer Research* **2016**, *76* (15), 4320-4331.

217. Raes, F.; Sobilo, J.; Natkunarajah, S.; Trochet, P.; Fuchs, D.; Lerondel, S.; Le Pape, A., Novel imaging strategy to assess the antitumor efficacy of treatments in an orthotopic mouse lung cancer model using ultrasound and photoacoustic imaging. AACR: 2016.

218. Hariri, A.; Fatima, A.; Mohammadian, N.; Mahmoodkalayeh, S.; Ansari, M. A.; Bely, N.; Avanaki, M. R., Development of low-cost photoacoustic imaging systems using very low-energy pulsed laser diodes. *Journal of Biomedical Optics* **2017**, *22* (7), 075001.

219. Lyu, Y.; Zhen, X.; Miao, Y.; Pu, K., Reaction-based semiconducting polymer nanoprobe for photoacoustic imaging of protein sulfenic acids. *ACS Nano* **2016**, *11* (1), 358-367.

220. Jiang, Y.; Pu, K., Advanced Photoacoustic Imaging Applications of Near-Infrared Absorbing Organic Nanoparticles. *Small* **2017**.

221. Jiang, Y.; Upputuri, P. K.; Xie, C.; Lyu, Y.; Zhang, L.; Xiong, Q.; Pramanik, M.; Pu, K., Broadband absorbing semiconducting polymer nanoparticles for photoacoustic imaging in second near-infrared window. *Nano letters* **2017**, *17* (8), 4964-4969.

222. Berninger, M. T.; Mohajerani, P.; Wildgruber, M.; Beziere, N.; Kimm, M. A.; Ma, X.; Haller, B.; Fleming, M. J.; Vogt, S.; Anton, M., Detection of intramyocardially injected DiR-labeled mesenchymal stem cells by optical and photoacoustic tomography. *Photoacoustics* **2017**, *6*, 37-47.

223. Zheng, B.; Lu, K.; Konkle, J. J.; Hensley, D. W.; Keselman, P.; Orendorff, R. D.; Tay, Z. W.; Yu, E.; Zhou, X. Y.; Bishop, M., Magnetic Particle Imaging. In *Design and Applications of Nanoparticles in Biomedical Imaging*, Springer: 2017; pp 69-93.
224. Zheng, B.; Marc, P.; Yu, E.; Gunel, B.; Lu, K.; Vazin, T.; Schaffer, D. V.; Goodwill, P. W.; Conolly, S. M., Quantitative magnetic particle imaging monitors the transplantation, biodistribution, and clearance of stem cells in vivo. *Theranostics* **2016**, *6* (3), 291.
225. Haegele, J.; Duschka, R.; Graeser, M.; Luedtke-Buzug, K.; Schaecke, C.; Panagiotopoulos, N.; Buzug, T.; Barkhausen, J.; Vogt, F. In *Magnetic particle imaging: kinetics of the intravascular signal in vivo*, Magnetic Particle Imaging (IWMPI), 2013 International Workshop on, IEEE: 2013; pp 1-1.
226. Saritas, E. U.; Goodwill, P. W.; Croft, L. R.; Konkle, J. J.; Lu, K.; Zheng, B.; Conolly, S. M., Magnetic particle imaging (MPI) for NMR and MRI researchers. *Journal of Magnetic Resonance* **2013**, *229*, 116-126.
227. Shin, T.-H.; Choi, Y.; Kim, S.; Cheon, J., Recent advances in magnetic nanoparticle-based multi-modal imaging. *Chemical Society Reviews* **2015**, *44* (14), 4501-4516.
228. Hensley, D.; Tay, Z. W.; Dhavalikar, R.; Zheng, B.; Goodwill, P.; Rinaldi, C.; Conolly, S., Combining magnetic particle imaging and magnetic fluid hyperthermia in a theranostic platform. *Physics in medicine and biology* **2017**, *62* (9), 3483.
229. Bulte, J. W.; Walczak, P.; Janowski, M.; Krishnan, K. M.; Arami, H.; Halkola, A.; Gleich, B.; Rahmer, J., Quantitative “hot spot” imaging of transplanted stem cells using superparamagnetic tracers and magnetic particle imaging (MPI). *Tomography: a journal for imaging research* **2015**, *1* (2), 91.
230. Poß, M.; Tower, R. J.; Napp, J.; Appold, L. C.; Lammers, T.; Alves, F.; Glüer, C.-C.; Boretius, S.; Feldmann, C., Multimodal [GdO]<sup>+</sup>[ICG]<sup>-</sup> Nanoparticles for Optical, Photoacoustic, and Magnetic Resonance Imaging. *Chemistry of Materials* **2017**, *29* (8), 3547-3554.
231. Lee, D.-E.; Koo, H.; Sun, I.-C.; Ryu, J. H.; Kim, K.; Kwon, I. C., Multifunctional nanoparticles for multimodal imaging and theragnosis. *Chemical Society Reviews* **2012**, *41* (7), 2656-2672.
232. Bulte, J. W.; Walczak, P.; Gleich, B.; Weizenecker, J.; Markov, D. E.; Aerts, H. C.; Boeve, H.; Borgert, J.; Kuhn, M. In *MPI cell tracking: what can we learn from MRI?*, Medical Imaging 2011: Biomedical Applications in Molecular, Structural, and Functional Imaging, International Society for Optics and Photonics: 2011; p 79650Z.
233. Mérian, J.; Gravier, J.; Navarro, F.; Texier, I., Fluorescent nanoprobe dedicated to in vivo imaging: from preclinical validations to clinical translation. *Molecules* **2012**, *17* (5), 5564-5591.
234. Wang, J.; Guo, F.; Yu, M.; Liu, L.; Tan, F.; Yan, R.; Li, N., Rapamycin/DiR loaded lipid-polyaniline nanoparticles for dual-modal imaging guided enhanced photothermal and antiangiogenic combination therapy. *Journal of Controlled Release* **2016**, *237*, 23-34.

235. Huynh, E.; Rajora, M. A.; Zheng, G., Multimodal micro, nano, and size conversion ultrasound agents for imaging and therapy. *Wiley Interdisciplinary Reviews: Nanomedicine and Nanobiotechnology* **2016**, 8 (6), 796-813.
236. Magnetic Insight, I., Momentum Imager.
237. Wassel, R. A.; Grady, B.; Kopke, R. D.; Dormer, K. J., Dispersion of super paramagnetic iron oxide nanoparticles in poly (d, l-lactide-co-glycolide) microparticles. *Colloids and Surfaces A: Physicochemical and Engineering Aspects* **2007**, 292 (2), 125-130.
238. Kim, T.; Lee, N.; Arifin, D. R.; Shats, I.; Janowski, M.; Walczak, P.; Hyeon, T.; Bulte, J. W., In Vivo Micro-CT Imaging of Human Mesenchymal Stem Cells Labeled with Gold-Poly-l-Lysine Nanocomplexes. *Advanced Functional Materials* **2016**.
239. Arconada-Alvarez, S. J.; Lemaster, J. E.; Wang, J.; Jokerst, J. V., The development and characterization of a novel yet simple 3D printed tool to facilitate phantom imaging of photoacoustic contrast agents. *Photoacoustics* **2017**, 5, 17-24.
240. Yang, H.; Cai, W.; Xu, L.; Lv, X.; Qiao, Y.; Li, P.; Wu, H.; Yang, Y.; Zhang, L.; Duan, Y., Nanobubble–Affibody: Novel ultrasound contrast agents for targeted molecular ultrasound imaging of tumor. *Biomaterials* **2015**, 37, 279-288.
241. Zheng, B.; Vazin, T.; Goodwill, P. W.; Conway, A.; Verma, A.; Saritas, E. U.; Schaffer, D.; Conolly, S. M., Magnetic particle imaging tracks the long-term fate of in vivo neural cell implants with high image contrast. *Sci. Rep.* **2015**, 5, 14055.
242. Lu, C.-W.; Hung, Y.; Hsiao, J.-K.; Yao, M.; Chung, T.-H.; Lin, Y.-S.; Wu, S.-H.; Hsu, S.-C.; Liu, H.-M.; Mou, C.-Y., Bifunctional magnetic silica nanoparticles for highly efficient human stem cell labeling. *Nano letters* **2007**, 7 (1), 149-154.
243. Frank, J. A.; Miller, B. R.; Arbab, A. S.; Zywicke, H. A.; Jordan, E. K.; Lewis, B. K.; Bryant Jr, L. H.; Bulte, J. W., Clinically applicable labeling of mammalian and stem cells by combining superparamagnetic iron oxides and transfection agents. *Radiology* **2003**, 228 (2), 480-487.
244. Yu, M.; Huang, S.; Yu, K. J.; Clyne, A. M., Dextran and polymer polyethylene glycol (PEG) coating reduce both 5 and 30 nm iron oxide nanoparticle cytotoxicity in 2D and 3D cell culture. *International journal of molecular sciences* **2012**, 13 (5), 5554-5570.
245. Venugopal, B.; Fernandez, F. B.; Harikrishnan, V.; John, A., Post implantation fate of adipogenic induced mesenchymal stem cells on Type I collagen scaffold in a rat model. *Journal of Materials Science: Materials in Medicine* **2017**, 28 (2), 28.
246. Volatron, J.; Carn, F.; Kolosnjaj-Tabi, J.; Javed, Y.; Vuong, Q. L.; Gossuin, Y.; Ménager, C.; Luciani, N.; Charron, G.; Hémadi, M., Ferritin Protein Regulates the Degradation of Iron Oxide Nanoparticles. *Small* **2017**, 13 (2).

247. Dabbagh, K.; Laurent, G. J.; Shock, A.; Leoni, P.; Papakrivopoulou, J.; Chambers, R. C., Alpha-1-antitrypsin stimulates fibroblast proliferation and procollagen production and activates classical MAP kinase signalling pathways. *Journal of cellular physiology* **2001**, *186* (1), 73-81.
248. Bobo, D.; Robinson, K. J.; Islam, J.; Thurecht, K. J.; Corrie, S. R., Nanoparticle-Based Medicines: A Review of FDA-Approved Materials and Clinical Trials to Date. *Pharmaceutical Research* **2016**, *33* (10), 2373-2387.
249. White, S. C.; Lorigan, P.; Margison, G. P.; Margison, J. M.; Martin, F.; Thatcher, N.; Anderson, H.; Ranson, M., Phase II study of SPI-77 (sterically stabilised liposomal cisplatin) in advanced non-small-cell lung cancer. *British Journal of Cancer* **2006**, *95* (7), 822-828.
250. Sanhai, W. R.; Sakamoto, J. H.; Canady, R.; Ferrari, M., Seven challenges for nanomedicine. *Nature Nanotechnology* **2008**, *3*, 242.
251. Chen, W.; Palazzo, A.; Hennink, W. E.; Kok, R. J., Effect of Particle Size on Drug Loading and Release Kinetics of Gefitinib-Loaded PLGA Microspheres. *Molecular Pharmaceutics* **2017**, *14* (2), 459-467.
252. Chen, W.; Cheng, C.-A.; Zink, J. I., Spatial, Temporal, and Dose Control of Drug Delivery using Noninvasive Magnetic Stimulation. *ACS Nano* **2019**, *13* (2), 1292-1308.
253. Dunn, A. E.; Dunn, D. J.; Macmillan, A.; Whan, R.; Stait-Gardner, T.; Price, W. S.; Lim, M.; Boyer, C., Spatial and temporal control of drug release through pH and alternating magnetic field induced breakage of Schiff base bonds. *Polymer Chemistry* **2014**, *5* (10), 3311-3315.
254. Man, F.; Lammers, T.; T M de Rosales, R., Imaging Nanomedicine-Based Drug Delivery: a Review of Clinical Studies. *Mol Imaging Biol* **2018**, *20* (5), 683-695.
255. Luo, D.; Goel, S.; Liu, H.-J.; Carter, K. A.; Jiang, D.; Geng, J.; Kuttyreff, C. J.; Engle, J. W.; Huang, W.-C.; Shao, S.; Fang, C.; Cai, W.; Lovell, J. F., Intrabilayer <sup>64</sup>Cu Labeling of Photoactivatable, Doxorubicin-Loaded Stealth Liposomes. *ACS Nano* **2017**, *11* (12), 12482-12491.
256. Liow, S. S.; Dou, Q.; Kai, D.; Li, Z.; Sugiarto, S.; Yu, C. Y. Y.; Kwok, R. T. K.; Chen, X.; Wu, Y.-L.; Ong, S. T.; Kizhakeyil, A.; Verma, N. K.; Tang, B. Z.; Loh, X. J., Long-Term Real-Time In Vivo Drug Release Monitoring with AIE Thermogelling Polymer. *Small* **2017**, *13* (7), 1603404.
257. Liu, J.; Bu, J.; Bu, W.; Zhang, S.; Pan, L.; Fan, W.; Chen, F.; Zhou, L.; Peng, W.; Zhao, K.; Du, J.; Shi, J., Real-Time In Vivo Quantitative Monitoring of Drug Release by Dual-Mode Magnetic Resonance and Upconverted Luminescence Imaging. *Angewandte Chemie International Edition* **2014**, *53* (18), 4551-4555.
258. Bayer, C. L.; Luke, G. P.; Emelianov, S. Y., PHOTOACOUSTIC IMAGING FOR MEDICAL DIAGNOSTICS. *Acoustics today* **2012**, *8* (4), 15-23.

259. Zhang, Y.; Jeon, M.; Rich, L. J.; Hong, H.; Geng, J.; Zhang, Y.; Shi, S.; Barnhart, T. E.; Alexandridis, P.; Huizinga, J. D.; Seshadri, M.; Cai, W.; Kim, C.; Lovell, J. F., Non-invasive multimodal functional imaging of the intestine with frozen micellar naphthalocyanines. *Nature Nanotechnology* **2014**, *9*, 631.
260. Li, X.; Bottini, M.; Zhang, L.; Zhang, S.; Chen, J.; Zhang, T.; Liu, L.; Rosato, N.; Ma, X.; Shi, X.; Wu, Y.; Guo, W.; Liang, X.-J., Core-Satellite Nanomedicines for in Vivo Real-Time Monitoring of Enzyme-Activatable Drug Release by Fluorescence and Photoacoustic Dual-Modal Imaging. *ACS Nano* **2019**, *13* (1), 176-186.
261. Bhutiani, N.; Samykutty, A.; McMasters, K. M.; Egilmez, N. K.; McNally, L. R., In vivo tracking of orally-administered particles within the gastrointestinal tract of murine models using multispectral optoacoustic tomography. *Photoacoustics* **2019**, *13*, 46-52.
262. Limpanuparb, T.; Roongruangsree, P.; Areekul, C., A DFT investigation of the blue bottle experiment: E<sup>o</sup>half-cell analysis of autoxidation catalysed by redox indicators. *R. Soc. Open Sci.* **2017**, *4* (11), 170708/1-170708/23.
263. Murakami, N.; Maruno, H., In situ photoacoustic spectroscopic analysis on photocatalytic decolorization of methylene blue over titanium(iv) oxide particles. *RSC Advances* **2016**, *6* (70), 65518-65523.
264. Gao, Y.; Kuang, Y.; Guo, Z.-F.; Guo, Z.; Krauss, I. J.; Xu, B., Enzyme-Instructed Molecular Self-assembly Confers Nanofibers and a Supramolecular Hydrogel of Taxol Derivative. *Journal of the American Chemical Society* **2009**, *131* (38), 13576-13577.
265. Felgentraeger, A.; Maisch, T.; Dobler, D.; Spaeth, A., Hydrogen bond acceptors and additional cationic charges in methylene blue derivatives: photophysics and antimicrobial efficiency. *BioMed Res. Int.* **2013**, 482167, 12 pp.
266. Fonte, P.; Soares, S.; Costa, A.; Andrade, J. C.; Seabra, V.; Reis, S.; Sarmiento, B., Effect of cryoprotectants on the porosity and stability of insulin-loaded PLGA nanoparticles after freeze-drying. *Biomatter* **2012**, *2* (4), 329-339.
267. Holzer, M.; Vogel, V.; Mäntele, W.; Schwartz, D.; Haase, W.; Langer, K., Physico-chemical characterisation of PLGA nanoparticles after freeze-drying and storage. *European Journal of Pharmaceutics and Biopharmaceutics* **2009**, *72* (2), 428-437.
268. Zaias, J.; Mineau, M.; Cray, C.; Yoon, D.; Altman, N. H., Reference values for serum proteins of common laboratory rodent strains. *J Am Assoc Lab Anim Sci* **2009**, *48* (4), 387-390.
269. Wang, R.; Zhou, L.; Wang, W.; Li, X.; Zhang, F., In vivo gastrointestinal drug-release monitoring through second near-infrared window fluorescent bioimaging with orally delivered microcarriers. *Nature Communications* **2017**, *8*, 14702.
270. Cohen, M. H.; Gootenberg, J.; Keegan, P.; Pazdur, R., FDA drug approval summary: bevacizumab (Avastin®) plus carboplatin and paclitaxel as first-line treatment of

advanced/metastatic recurrent nonsquamous non-small cell lung cancer. *The oncologist* **2007**, *12* (6), 713-718.

271. Baran, T. M.; Giesselman, B. R.; Hu, R.; Biel, M. A.; Foster, T. H., Factors influencing tumor response to photodynamic therapy sensitized by intratumor administration of methylene blue. *Lasers in Surgery and Medicine* **2010**, *42* (8), 728-735.

272. Deutsch, H. M.; Glinski, J. A.; Hernandez, M.; Haugwitz, R. D.; Narayanan, V. L.; Suffness, M.; Zalkow, L. H., Synthesis of congeners and prodrugs. 3. Water-soluble prodrugs of taxol with potent antitumor activity. *Journal of Medicinal Chemistry* **1989**, *32* (4), 788-792.

273. Kingston, D. G. I.; Hawkins, D. R.; Ovington, L., New Taxanes From *Taxus brevifolia*. *Journal of Natural Products* **1982**, *45* (4), 466-470.

274. Dollendorf, C.; Hetzer, M.; Ritter, H., Polymeric redox-responsive delivery systems bearing ammonium salts cross-linked via disulfides. *Beilstein journal of organic chemistry* **2013**, *9* (1), 1652-1662.

275. Snehalatha, T.; Rajanna, K. C.; Saiprakash, P. K., Methylene Blue - Ascorbic Acid: An Undergraduate Experiment in Kinetics. *Journal of Chemical Education* **1997**, *74* (2), 228.

276. Galagan, Y.; Su, W.-F., Reversible photoreduction of methylene blue in acrylate media containing benzyl dimethyl ketal. *Journal of Photochemistry and Photobiology A: Chemistry* **2008**, *195* (2), 378-383.

277. Dhapare, S. S.; Dash, A. K., Effect of differential drying techniques on PLGA nanoparticles containing hydrophobic and hydrophilic anticancer agents. *Therapeutic Delivery* **2015**, *6* (1), 27-39.

278. Michen, B.; Geers, C.; Vanhecke, D.; Endes, C.; Rothen-Rutishauser, B.; Balog, S.; Petri-Fink, A., Avoiding drying-artifacts in transmission electron microscopy: Characterizing the size and colloidal state of nanoparticles. *Scientific Reports* **2015**, *5*, 9793.

279. Hariri, A.; Zhao, E.; Jeevarathinam, A. S.; Lemaster, J.; Zhang, J.; Jokerst, J. V., Molecular imaging of oxidative stress using an LED-based photoacoustic imaging system. *Scientific Reports* **2019**, *9* (1), 11378.

280. Wang, J.; Jeevarathinam, A. S.; Humphries, K.; Jhunjhunwala, A.; Chen, F.; Hariri, A.; Miller, B. R.; Jokerst, J. V., A Mechanistic Investigation of Methylene Blue and Heparin Interactions and Their Photoacoustic Enhancement. *Bioconjugate Chemistry* **2018**, *29* (11), 3768-3775.

281. Vicari, L.; Musumeci, T.; Giannone, I.; Adamo, L.; Conticello, C.; De Maria, R.; Pignatello, R.; Puglisi, G.; Gulisano, M., Paclitaxel loading in PLGA nanospheres affected the in vitro drug cell accumulation and antiproliferative activity. *BMC Cancer* **2008**, *8* (1), 212.

282. Fonseca, C.; Simoes, S.; Gaspar, R., Paclitaxel-loaded PLGA nanoparticles: preparation, physicochemical characterization and in vitro anti-tumoral activity. *Journal of controlled release* **2002**, *83* (2), 273-286.
283. Cabanes, A.; Briggs, K. E.; Gokhale, P. C.; Treat, J.; Rahman, A., Comparative in vivo studies with paclitaxel and liposome-encapsulated paclitaxel. *International journal of oncology* **1998**, *12* (5), 1035-1075.
284. Hsieh, T.-S.; Wu, J.-Y.; Chang, C.-C., Multiple fluorescent behaviors of phenothiazine-based organic molecules. *Dyes and Pigments* **2015**, *112*, 34-41.
285. Hsieh, T.-S.; Wu, J.-Y.; Chang, C.-C., Synthesis of a Photostable Near-Infrared-Absorbing Photosensitizer for Selective Photodamage to Cancer Cells. *Chemistry – A European Journal* **2014**, *20* (31), 9709-9715.
286. Drummond, J. E., Magneto-acoustic resonance imaging. Google Patents: 1995.
287. Hickling, S.; Hobson, M.; El Naqa, I., Feasibility of X-Ray Acoustic Computed Tomography as a Tool for Noninvasive Volumetric In Vivo Dosimetry. *International Journal of Radiation Oncology• Biology• Physics* **2014**, *90* (1), S843.
288. Ogunlade, O.; Beard, P., Exogenous contrast agents for thermoacoustic imaging: An investigation into the underlying sources of contrast. *Med. Phys.* **2015**, *42* (1), 170-181.
289. Qu, M.; Mehrmohammadi, M.; Emelianov, S., Detection of Nanoparticle Endocytosis Using Magneto-Photoacoustic Imaging. *Small* **2011**, *7* (20), 2858-2862.
290. Wang, X.; Roberts, W. W.; Carson, P. L.; Wood, D. P.; Fowlkes, J. B., Photoacoustic tomography: a potential new tool for prostate cancer. *Biomedical optics express* **2010**, *1* (4), 1117-1126.
291. Valluru, K. S.; Chinni, B. K.; Rao, N. A.; Bhatt, S.; Dogra, V. S. In *Development of a c-scan photoacoustic imaging probe for prostate cancer detection*, SPIE Medical Imaging, International Society for Optics and Photonics: 2011; pp 79680C-79680C-7.
292. Kumavor, P. D.; Alqasemi, U.; Tavakoli, B.; Li, H.; Yang, Y.; Sun, X.; Warych, E.; Zhu, Q., Co-registered pulse-echo/photoacoustic transvaginal probe for real time imaging of ovarian tissue. *Journal of biophotonics* **2013**, *6* (6-7), 475-484.
293. Zhang, Y.; Hong, G.; Zhang, Y.; Chen, G.; Li, F.; Dai, H.; Wang, Q., Ag<sub>2</sub>S quantum dot: a bright and biocompatible fluorescent nanoprobe in the second near-infrared window. *ACS nano* **2012**, *6* (5), 3695-3702.
294. Chen, Q.; Liu, X.; Chen, J.; Zeng, J.; Cheng, Z.; Liu, Z., A Self-Assembled Albumin-Based Nanoprobe for In Vivo Ratiometric Photoacoustic pH Imaging. *Advanced Materials* **2015**, *27* (43), 6820-6827.

295. Moon, G. D.; Choi, S.-W.; Cai, X.; Li, W.; Cho, E. C.; Jeong, U.; Wang, L. V.; Xia, Y., A new theranostic system based on gold nanocages and phase-change materials with unique features for photoacoustic imaging and controlled release. *Journal of the American Chemical Society* **2011**, *133* (13), 4762-4765.
296. Zha, Z.; Zhang, S.; Deng, Z.; Li, Y.; Li, C.; Dai, Z., Enzyme-responsive copper sulphide nanoparticles for combined photoacoustic imaging, tumor-selective chemotherapy and photothermal therapy. *Chemical Communications* **2013**, *49* (33), 3455-3457.
297. Yu, J.; Yang, C.; Li, J.; Ding, Y.; Zhang, L.; Yousaf, M. Z.; Lin, J.; Pang, R.; Wei, L.; Xu, L., Multifunctional Fe<sub>5</sub>C<sub>2</sub> Nanoparticles: A Targeted Theranostic Platform for Magnetic Resonance Imaging and Photoacoustic Tomography-Guided Photothermal Therapy. *Advanced Materials* **2014**, *26* (24), 4114-4120.